HELLENIC REPUBLIC
National and Kapodistrian
University of Athens
EST. 1837

National and Kapodistrian University of Athens

School of Science

Department of Geology and Geoenvironment

Postgraduate program: Seismology

Non-Extensive statistical physics properties of seismic coda waves recorded during the Santorini unrest period 2011-2012

MSc. Thesis

Theodoros Aspiotis

Examination Committee

Professor Filippos Vallianatos (Supervisor)

Professor Gerasimos A. Tselentis

Assistant Professor George Kaviris

Science makes people reach selflessly for truth and objectivity;

Lise Meitner

Preface

I would like to express my thankfulness to Professor Filippos Vallianatos, for introducing me to the world of statistical mechanics and its implementations. It was a tough and at the same time an exciting trip, especially when diving into the theoretical perspective of StatMech. and non-extensive statistical mechanics.
The inspiration of this dissertation was an internal curiosity on how to connect the dots between any complex active seismotectonic regime, such as a volcanic regime under stress, with the physical subsurface processes, in terms of statistical mechanics.
In the framework of the present postgraduate dissertation in Seismology, we developed a new software for data acquisition, processing and result presentation with the potential of a multidiscipline utility. The novel procedures in signal analysis and the relatively simple process of entropic indices via a simplified and detailed graphical user interface, make SeisCompLex a useful software, especially in an area where computer tools are limited, making the implementation of non-extensive statistical physics, a difficult task. SeisCompLex, contains a unified library of functions and is compatible in both Windows and Linux platforms.
I would also like to thank Professor G. A. Tselentis for his overall contribution to a variety of problems (academic and research) and Assistant Professor G. Kaviris for his continuous support throughout my studying years at the National and Kapodistrian University of Athens.
Lastly but not least I would like to thank Dr. Vasilis Kapetanidis and Mr. Ioannis Koutalonis for helping me in understanding the difficulties and peculiarities, such as those resulting from the implementation of statistical mechanics in complex physical systems.

Contents

Abstract

The unrest period in Santorini's caldera during 2011-2012, led several studies to raise the important question of whether seismicity is associated with an impending and potential volcanic eruption or if it solely relieves the accumulated tectonic energy. In the present work, we study seismic coda waves, generated by local earthquake events prior, during and after the Santorini's unrest period (volcanic and seismic crisis) that occurred within the caldera area. Coda waves are interpreted as scattered seismic waves generated by heterogeneities within the Earth, i.e. by faults, fractures, fissure structures, microcracks, velocity and/or density boundaries/anomalies, etc. In particular, we utilize all three components of the seismograms recorded by three seismological stations on the Santorini island and estimate the duration of the coda waves by implementing a five-step procedure that includes the signal-to-noise ratio, the STA/LTA like method, in time domain and upon analytic signal obtained after implementing Hilbert transformation, and the short time Fourier transform, using gaussian windowing as a window function. The final estimation was verified or re-estimated manually due to the existent ambient seismic noise. Because of the nature and the path complexity of the coda waves and towards achieving a unified framework for the study of the immerse geo-structural seismotectonic complexity of the Santorini volcanic complex, we use Non-Extensive Statistical Physics (NESP) to study the probability density functions (pdfs) of the increments of seismic coda waves. NESP, forms a generalization of the Boltzmann-Gibbs statistical mechanics that has been extensively used for the analysis of semi-chaotic systems that exhibit long-range interactions, memory effects and multi-fractality. The analysis and results demonstrate that the seismic coda waves increments, deviate from the Gaussian shape and their respective pdfs could adequately be described and processed by the q-Gaussian distribution. Furthermore and in order to investigate the dynamical evolution of the volcanic-tectonic activity, we estimate the q_s-indices derived from the pdfs of the coda wave time series increments, and present their variations as a function of time, of space (spaciotemporal variation), of local magnitude (M_L) and epicentral distance (measured in km) prior, during and after the caldera unrest period from 2009 to 2014 [1].

Περίληψη

Η περίοδος της ηφαιστειακής κρίσης στο νησί της Σαντορίνης κατά τη περίοδο 2011-2012, οδήγησε αρκετές επιστημονικές μελέτες να εγείρουν το κρίσιμο ερώτημα, εάν η σεισμικότητα της ευρύτερης περιοχής της καλντέρας, σχετίζεται με μια επικείμενη και πιθανή ηφαιστειακή έκρηξη ή αν εκφορτίζει τη συσσωρευμένη τεκτονική ενέργεια. Στην παρούσα μεταπτυχιακή διατριβή, μελετήσαμε τα σεισμικά κύματα ουράς (Coda waves), από τα τοπικά σεισμικά γεγονότα πριν, κατά τη διάρκεια και μετά την περίοδο της ηφαιστειακή και σεισμικής κρίσης της Σαντορίνης. Τα σεισμικά κύματα ουράς, οφείλουν την παρουσία τους σε φαινόμενα σκέδασης και στην πολυπλοκότητα της κατανομής των σκεδαστών του υπεδάφους, στις ανομοιογένειες του εσωτερικού της Γης, όπως είναι οι ρωγμές και η σχιστότητα των πετρωμάτων, τα ρήγματα, στα όρια μετάβασης υλικών διαφορετικής πυκνότητας, και στις πάσης φύσεως γεωφυσικές ανομοιογένειες ως προς τις ιδιότητες των υλικών στα ανώτερα στρώματα του φλοιού της Γης. Πιο συγκεκριμένα, λάβαμε υπόψη και τις τρεις συνιστώσες των σεισμολογικών σταθμών στο νησί της Σαντορίνης και εκτιμήσαμε τη διάρκεια των σεισμικών κυμάτων ουράς, εφαρμόζοντας μια διαδικασία πέντε επιπέδων, η οποία περιλαμβάνει την αναλογία σεισμικού σήματος προς θόρυβο (SNR), τη μέθοδο τύπου βραχέως μέσου χρόνου προς μακροπρόθεσμο μέσο χρόνο (STA/LTA) στο πεδίο του χρόνου αλλά και στο αναλυτικό σήμα, όπως αυτό προκύπτει από την εφαρμογή του μετασχηματισμού Hilbert, καθώς και τον μετασχηματισμό Fourier βραχέως χρόνου (STFT), εφαρμόζοντας παράθυρο Γκαουσιανής συνάρτησης (window function). Η τελική εκτίμηση της διάρκειας των κυμάτων ουράς, επαληθεύτηκε ή και επανεκτιμήθηκε αναλογικά από τον χρήστη, εξαιτίας της ύπαρξης ισχυρού σεισμικού θορύβου. Λόγω της πολυπλοκότητας των κυμάτων ουράς, για τη μελέτη του ηφαιστειακού συμπλέγματος της Σαντορίνης, εφαρμόσαμε την θεωρία της μη εκτατικής στατιστικής φυσικής (NESP). Η προσέγγιση NESP εκφράζει την γενίκευση της στατιστικής μηχανικής των Boltzmann-Gibbs και έχει χρησιμοποιηθεί εκτενώς για την ανάλυση πολύπλοκων συστημάτων, με εμφανή χαρακτηριστικά και ιδιότητες αλληλεπίδρασης μακράς εμβέλειας, μνήμης και μορφοκλασματικότητας. Η ανάλυση και τα αποτελέσματα της παρούσας διατριβής δείχνουν ότι οι διαφορές πλάτους των διαδοχικών σημείων των σεισμικών κυμάτων ουράς (στο πεδίο του χρόνου), αποκλίνουν από το στατιστικό πρότυπο τύπου Gauss, καθώς οι αντίστοιχες συναρτήσεις πυκνότητας πιθανότητας (PDFs), μπορούν να περιγραφούν επαρκώς από κατανομές πιθανότητας που προκύπτουν από τον μη εκτατικό φορμαλισμό και πιο συγκεκριμένα από την κατανομή q-Gaussian. Επιπλέον, για να διερευνήσουμε τη δυναμική εξέλιξη της ηφαιστειακής-σεισμοτεκτονικής δραστηριότητας, εκτιμήσαμε τους εντροπικούς δείκτες σκέδασης q_s όπως αυτοί προκύπτουν από την μη γραμμική ανάλυση των PDFs, παρουσιάζοντας τις μεταβολές τους ως συνάρτηση του χρόνου, του χώρου (χωροχρονική μεταβολή), του τοπικού μεγέθους (M_L) καθώς και της επικεντρικής απόστασης (km) πριν, κατά τη διάρκεια και μετά την περίοδο ηφαιστειακής κρίσης της καλντέρας, από το 2009 έως το 2014.

1 Area of Interest

1.1 Physical Interest of Santorini's unrest period of 2011 – 2012

The inflation of Santorini's volcano alongside with the immense local seismicity and the GPS spatio-temporal fluctuations, following a not expected deflation behavior, had led to the hypothesis of a potential volcanic eruption.
Numerous scientific studies from different disciplines, have suggested a complex and unstable magma intrusion(s) within Kameni and Columbo tectonovolcanic lineaments, gaining the interest of the global scientific community.
We investigated the Santorini volcanic complex from a geophysical perspective, in order to have an insight of the local sub-surface physical properties prior during and after the unrest period.

1.2 Tectonic regime of Eastern Mediterranean and the Hellenic Volcanic Arc.

The Hellenic Arc is characterized as one of the most multiphase deformed and complex geotectonic environments throughout the world. The geological history of the wider area started approximately 250 million years ago, when the ocean of Tethys was formed from Pangea's super continental fragmentation [2]. This period is extended at the end of the Triassic, through the Mesozoic and Cenozoic era. Tethys ocean was the natural boundary between the archaic continents of Gondwana and Laurasia. The majority of the rock materials found in Greece has been formed from Tethys ocean and deposited as sediments and volcanic rocks. The geological evolution of Greece can be divided into two main periods. The Alpic period, placed in approximately 250 million to 20 million years ago, and the fore-Alpic period extended for the last 20 million years. The neo-tectonic period in which the Hellenic Arc was formed, is stretched during the last 10 million years.
The Hellenic trench, as given in Figure 1.1, is a typical convergent geological boundary between two major tectonic plates (Eurasian and African), forming the east Mediterranean subduction zone.

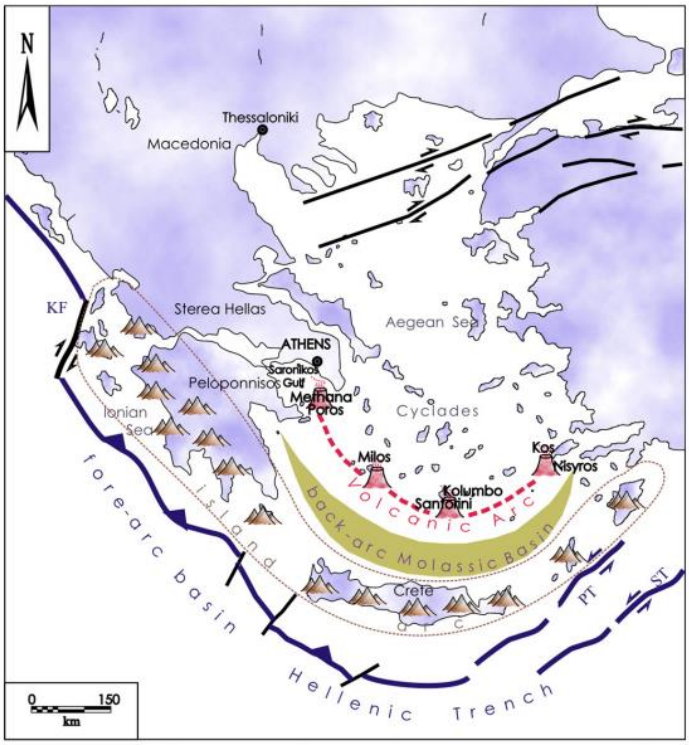

Figure 1.1 The volcanic arc and position of Santorini's island in the Hellenic arc [3].

The main feature of the Hellenic trench is the long (relatively continuous) and steep seaward slope, consisted of a multi-system trenches, troughs, deep seas and sea basins, extended from Rhodes (East) to Kefalonia (West).

The structure of the island arc involves a series of islands and islets, covering the southern part of the Greece (Rhodes, Crete, Kithira etc.).

The back arc is a sea basin north of Crete, characterized by shallow depth. Following, to the north, the volcanic arc consists of the active and inactive volcanoes of Sousaki, Methana, Milos, Santorini and Nisiros.

The Hellenic continental volcanic arc is the aftermath of the Africa-East Mediterranean tectonic plate collision with the Aegean-Anatolian micro plate. As the subducted slab descends, it is subjected to higher amount of pressure and temperature, causing the volatile constituents, as well as the water inside hydrate minerals (lattice structure), to evaporate, contributing to magma production. This procedure is continuously supplying the volcanic arc with new magma material, contributing to its spatial expansion and potentially causing violent and disastrous phenomena, such as landslides, eruptions etc. The differentiations in magmatism, as a consequence to changes in tectonics and minerals/rocks throughout the arc evolution, indicate a uniformly continuous subducted slab beneath the volcanic center, at depths of 130~150 km [4].

Santorini island and the whole volcanic arc is part of the Aegean micro-plate which is part of the major Eurasian tectonic plate. Contrariwise, the lithosphere of the eastern Mediterranean is part of the African plate.

In more details, the Aegean plate involves its surrounding large tectonic plates consisting of the Arabian to the east, the Eurasian to the north, north-west and the African to the south. The northern boundary of the Aegean plate is located at the western appearance of the North Anatolia strike-slip fault and its western margin is located at Ambracian gulf.

The northwest boundary of the Aegean plate is well-defined by the Cephalonia Transform Fault (CTF), whereas the eastern boundary is not clearly defined and it is approximately considered to be south of the Northern Anatolian Fault, in a wide area dominated by extensional regime and normal faulting, close to the 30^{o} E meridian [5].

The southern boundary of the Aegean micro-plate is considered to cover the area along the Hellenic Trench, setting the interface between the African and the Eurasian plates. This geological boundary is dominated and bounded by thrust fault structures. The seismotectonic regime across the boundary is congruent with the uplifting sedimentary fore-arc zone at the northern subduction zone, in the transition between the two plates. Consequently, the subduction along the Hellenic trench, resulted from the displacement of the Aegean plate, is estimated at a mean displacement rate of 4-6 cm/year [6] to the southwest and from the relative northern movement of the African plate [7] [8] [9].

The two lithospheric plates are converging with relative displacement of approximately 3 cm/year, considering the relative horizontal velocities with respect to Eurasia [10], resulting to the subduction of the oceanic plate of the east Mediterranean, due to its higher density, under the continental plate of the Aegean.

The complex nature of the Hellenic subduction zone can be further analyzed via the subducted area of the Adriatic (which is mainly characterized as continental lithosphere) reaching its sliding annual rate between 5-10 mm/year and the subducted area of the Ionian, which is considered an oceanic lithosphere, approaching the kinematic velocity of ~35 mm/year [11].

Therefore, the Hellenic arc structure consists of the Hellenic trench, the island arc, the back-arc and the volcanic arc. A lithospheric scale cross-section extended from Balkan foreland to the passive margin of African plate, is given in Figure 1.2.

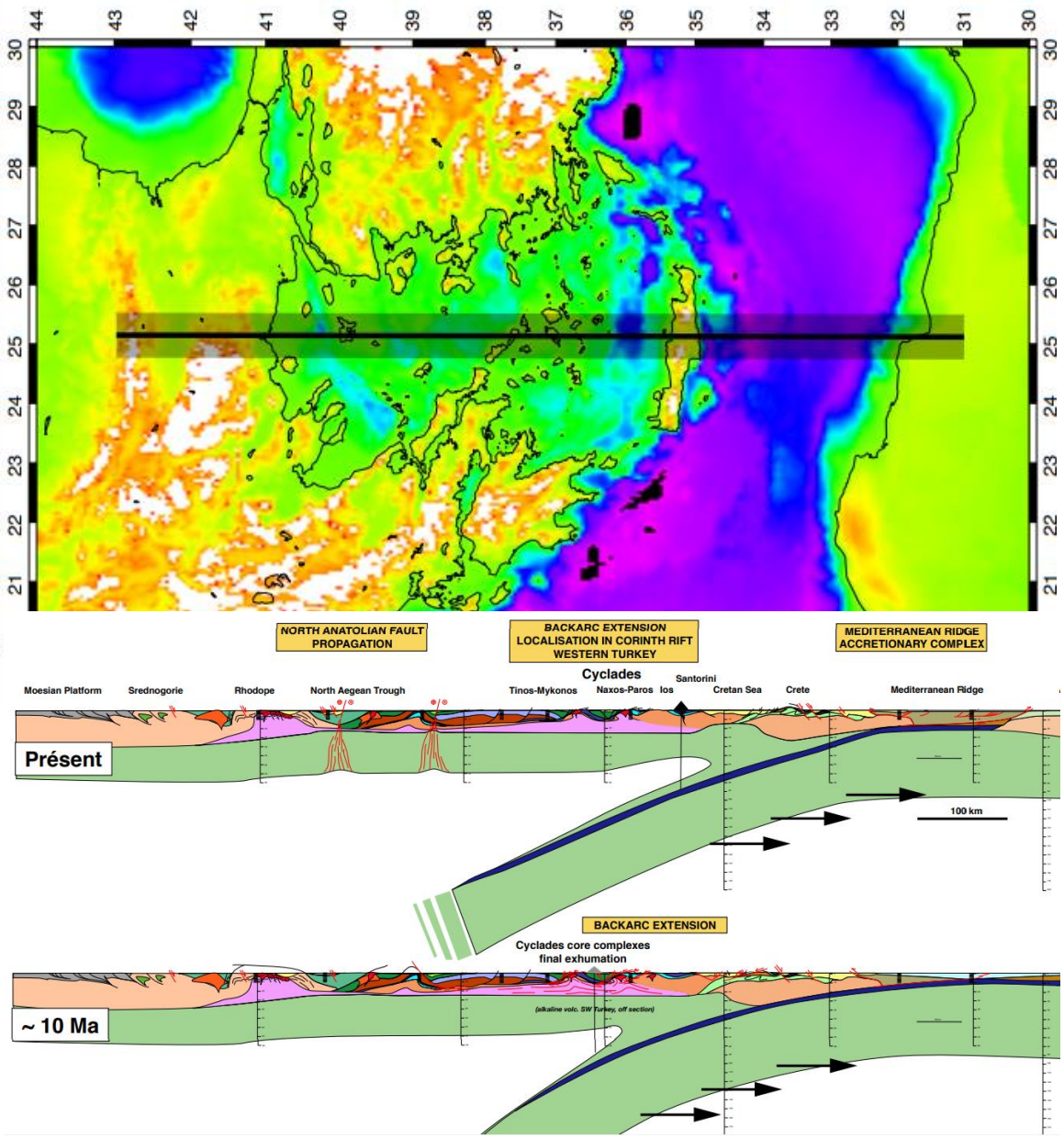

Figure 1.2 Schematic lithospheric scale illustration of the east Mediterranean subduction zone and location of the Santorini island within the Hellenic arc [13].

The relative motion between the Aegean and its neighboring lithospheric plates, can be kinematically explained via complex models, mainly introduced by GPS observations, as shown in Figure 1.3. The North Anatolian fault started to penetrate into the Aegean domain approximately 5Ma years ago, resulting to an external force to the constant sliding of the Aegean to the south and contributing to the neo-tectonic active deformation [12].

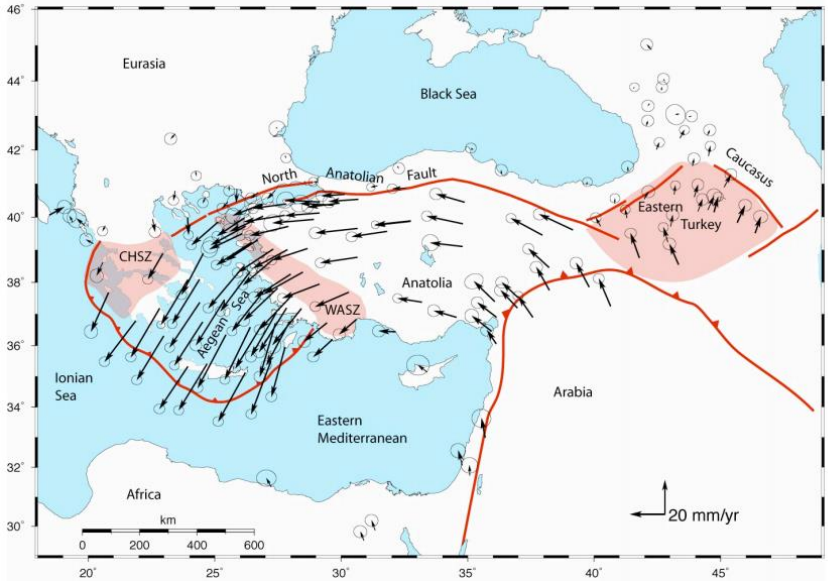

Figure 1.3 Kinematic motion in the wider area of Hellenides. CHSZ represents the central Hellenic shear zone while WASZ stands for the western Anatolian shear zone [10].

Today's slab geometry is defined by shallow dip in high depths (~40°-45°) and of approximately ~30° dip in the upper mantle. Geological and tectonic observations have shown that the slab's dip has decreased since the Cretaceous-Tertiary era [13].
Subduction rates have also decreased since the late Eocene, reaching 5-12mm/year by the late Miocene, due to the continuous changes of geodynamic environments (subduction of Pindos oceanic lithosphere, subduction of Hellenic carbonate platform, subduction of Ionian lithosphere). As a consequence, the evolution of the slab has continuously changed the localization of the arc geometry into several configurations. These configurations, set the volcanic arc in a shifting special displacement with a relatively constant direction from North to South. During Eocene, the volcanic arc occupied the region of northern Greece, especially the region of Thrace. At Oligocene and at the early Miocene the arc was located in the northeastern Aegean region (Lemnos, Agios Efstratios, Lesbos etc.). At late Miocene the volcanic arc extended from the northern Greece to Aegean (Ikaria and Samos islands). The current state of the volcanic arc, began to take shape after the epoch era of Pliocene.
The spatial transition of the Hellenic volcanic arc, throughout Paleogene and Neogene epoch, is given in the Figure 1.4.

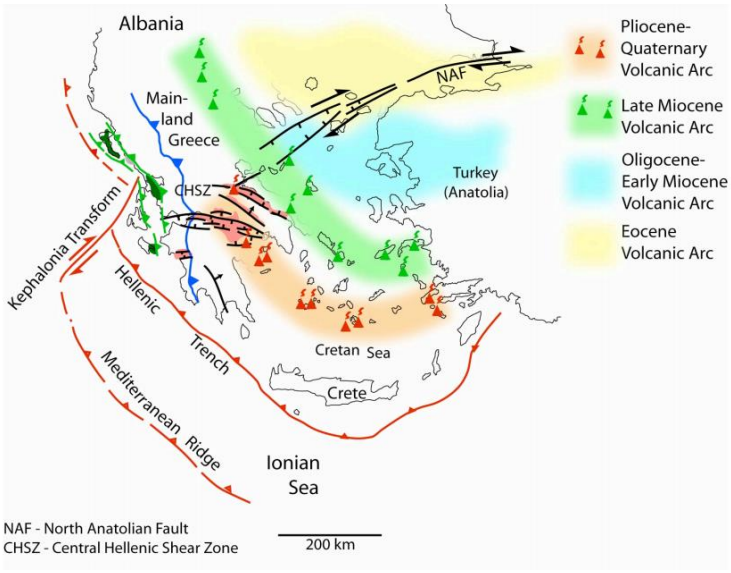

Figure 1.4 Schematic representation of the Hellenic volcanic arc spatial shifting, over the past approximately 40 Million years, from Eocene era until today [14].

1.3 Santorini Volcanic Complex

The Santorini Volcanic Complex is a part of the NE-SW oriented graben of the Anydros basin that extends from the Amorgos Island to the Christiana submarine islets volcanoes. The wider area of the Anydros basin is predominated by normal faults, a conclusion risen by the fault plane solutions of the major earthquake events.

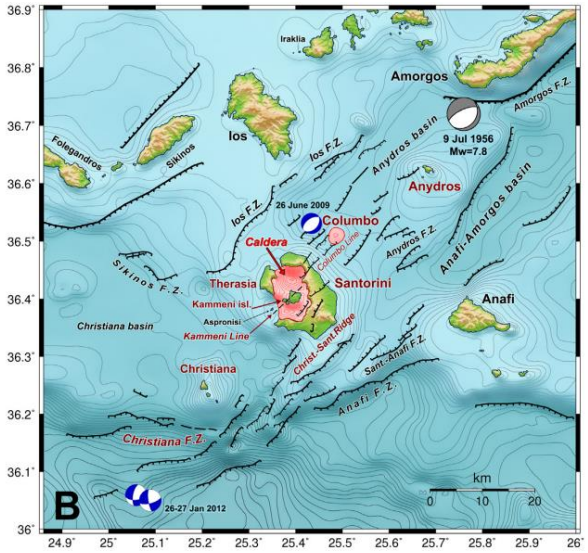

Figure 1.5 Seismotectonic map of the wider area of Santorini and its complex fault structure [15].

Seismicity in that area of the volcanic arc is mainly confined between the two major tectonovolcanic strike slip features of the Santorini's volcanic complex, i.e. the Columbo and Kameni lineaments. The position and orientation of these structures, as seen in Figure 1.5, have been responsible for the most violent eruptive episodes, as they provide a passageway to fluid and magma migration. The Columbo and Kameni lineaments, can be considered as strike slip faults, with normal-sinistral characteristics for Columbo [16], in an area (Anydros basin) dominated by pure normal faulting. The stress field of the wider area is distinct, having a northwest to southeast orientation.

The active volcanic island of Santorini is located at the center of the arc, being the most active volcano in the sea of Aegean. The volcanic activity of Santorini, initiated during Pliocene and continues up to day. The current geomorphological state of the island contains the remnants of the collapsed volcanic shield, forming the steep-walled caldera rim. It is mainly composed upon Mesozoic metamorphic rocks with congruent Pliocene submarine lavas, known as pillow lavas, and sediments that are exposed at the Akrotiri Peninsula, located at the southern part of the island. These terrain materials are part of the Hellenide-Anatolide orogenic belt, deformed during the Cenozoic period of closure the of European and African plates [17] [7] [18].

The most significant violent and recent eruption was the so-called Minoan volcanic eruption, which took place during the Bronze age in approximately 1600 B.C. That period has been characterized by immense seismicity [19] [20]. According to the analysis of the carbon isotope C^{14}, the mega-eruption has been well-defined between 1627 and 1600 B.C. with probability of 95% [21].

The post-Minoan eruptions started approximately 2200 years before. Since then, a number of minor and middle sized volcanic activity, expressed by effusive eruptions and lava flows, have occurred, marked by the recent eruptions of 1925 and 1950 [22] [23] [24], as shown in Figure 1.6.

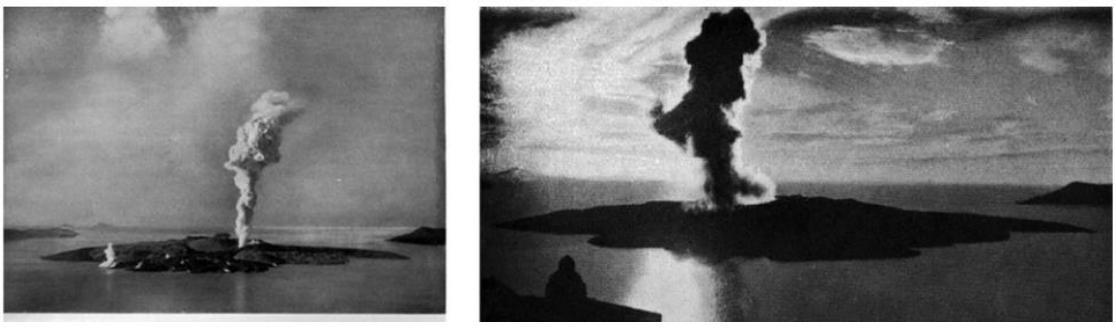

Figure 1.6 (a) The first instrumental observable volcanic eruption of Nea Kameni in 1926 and (b) the 1950 phreatic eruption of Palea Kameni [25].

There have been 12 major volcanic events until today [26], as presented in Table 1.1.

Santorini's Volcanic Event	Aftermath description
~1650 B.C.E.	Mega-Phreatic eruption. Creation of the caldera's rim.
~197 B.C.E.	Formation of the Hiera island.
~46 A.D.	Formation of Theia island.
~726 A.D.	Ash distribution stretched up to Elispodos and Macedonia.
Period from 1457 to 1458	Formation of island between Thirasia and Thera
Period from 1570 to 1573	Formation of Micra Kameni cone alongside to Palea Kameni.
27 / 09 / 1650	Columbo eruption and disappearance. 50 persons and more than 1000 animals died
Period from 1707 to 1711	Formation of Nea kameni.
Period from 1866 to 1870	Lava flow connects Nea Kameni with Micra Kameni. Formation of fimaroles.
Period from 1925 to 1928	Steam. Phreatic eruption. Formation of vast lava field throughout Nea Kameni.
Period from 1939 to 1941	Formation of lava vents and domes.
1950	Phreatic explosion and lava flow.
Unrest period from 2011 to 2012	No eruption has been occurred (yet).

Table 1.1 Post Minoan major volcanic activities of Santorini's volcano.

Evidence from historical data indicates that at least five volcanic eruptions have occurred within the Kameni lineament, while the Columbo tectono-volcanic feature is responsible for two eruptive events, dike swarms, tuff rings and cinder cones [27].
As seen in Table 1.1, the wider area of Santorini's volcanic system, remained relatively inactive during the period from 1950 to 2011. A small-scale volcanic activation, with aseismic and slow inflation in the northern part of Thera's caldera, occurred between 1994 and 2000 [28].
The next indication of volcanic activity, following the calm inflation of 1994 to 2000, was observed during the years 2011-12, showing signs of unrest behavior (volcanic crisis) accompanied with significant seismic activity and crustal deformation [15] [29] [30] [31]. During the unrest period, the earthquake epicenters were distributed along a subvertical surface, correlated to the Kameni line, a tectonic feature responsible for many major eruptions [15] [32] [33] [34]. Concurrently, GPS observations showed spatial deformation with cumulative concentric displacement of about 10 cm [35].
The hypothesis of a potential volcanic eruption was enhanced by the fact that the majority of the post-Minoan eruption events has been strongly associated with seismic activity within the Kameni tectonovolcanic lineament – zone.

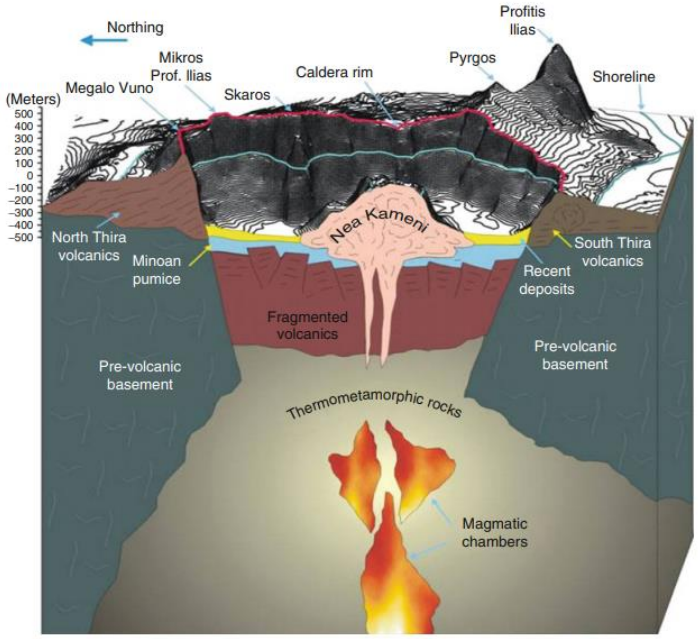

Figure 1.7 A schematic approach, demonstrating the sub-surface tectono-volcanic structure of Santorini's island [25].

2 Coda waves

2.1 A general introduction of Coda waves

When distributed heterogeneities interact with anisotropy and nonlinearity, a great geophysical entanglement procedure is risen, the so-called wave scattering phenomenon.
Due to the subsurface inhomogeneities [36] [37] [38], discontinuities, three dimensional variations of physical and chemical properties such as λ and μ parameters (where μ refers to the shear modulus or rigidity, and λ is defined with respect to μ by using the bulk modulus), site conditions (porosity, permeability, impedance variation etc.) and chaotically distributed fractal-scale scatterers, ground recording signatures with decay behavior are always presented in seismic stream records, following the direct body and surface waves. These waves have been introduced and established as coda waves and the main physical reason of their existence is associated to scattering effects, of primary body and surface waves and to the mode converted phases of one to another [36] [39] [40]. The term "coda" was first used in order to refer to the ground motion, after the last surface wave onset [41]. Another meaning of coda is associated with the tail of surface waves following the S phase arrival. In the first studies of local earthquake events [36] [42], coda waves corresponded to the recorded energy following the primary waves and were used in order to retrieve information of the seismic source and properties of the medium. Later, coda waves were extensively used as a measure of seismic magnitude (coda duration) [43] [44] [45] [46] [47] [48].

2.2 The decay rate of Codas attenuation

From observable characteristics, there was strong evidence that the origin of coda waves is associated with the lateral heterogeneities [36] [38] of the Earth's interior, as the scatterers have high density close to the surface, which decreases with depth, as well as to the repercussions of the overall tectonic dynamics [49].
The physical processes of attenuation refer to the decay rate of seismic amplitude and energy content and are strongly correlated with multiple scattering and intrinsic phenomena (intrinsic attenuation due to the transversion of elastic energy into heat and other forms of energy [50]). Scattering of a seismic wavefront is a physical procedure, occurred due to the fluctuations of the elastic properties of the Earth's materials and the existence of irregularities, discontinuities, fractures, faults, fissures, microcracks and a variety of randomly distributed scatterers, within the rigid layer of the lithosphere. On the contrary, the absorption effect, also contributing to the attenuation mechanism, reflects the anelastic properties of the Earth's interior. Phenomena contributing to the

absorption of seismic energy are fluid migrations and energy viscous dissipation in a wider area of fissile materials and crack like structures [50].
Coda attenuation can be quantitative determined via the non-dimensional Q parameter, as a function of scattering and intrinsic absorption [37]. According to LS GAO et. al. [51] and AM DAINTY et. al. [52], this approach is described by the equation:

$$\frac{1}{Q} = \frac{1}{Q_i} + \frac{1}{Q_s} \qquad (2.1)$$

where the Q quantity represents the quality factor, associated to the decay rate of seismic waves, $1/Q_i$ is the intrinsic absorption of the energy and $1/Q_s$ represents the attenuation factor due to scattering effects
A more complex form of this relation (2.1) was given by Dainty in 1981 [52]:

$$\frac{1}{Q} = \frac{1}{Q_i} + \frac{gv}{\omega} \qquad (2.2)$$

In this formula, g represents the turbidity coefficient, v the velocity and ω the frequency of the observed wave. Taking into account the above-mentioned formulas, it becomes clear that the site conditions-characteristics and the propagation path are responsible for the coda waves behavior. Consequently, geological materials with minor absorption of seismic energy but with strong scattering effects can produce long lasting seismic coda waves, such as the observed Lunar quakes, recorded from the Apollo missions [53]. The recent (2018) NASA's mission with the name InSight, through the successive deployment of the first Martian seismometer in Elysium Planitia area, called SEIS, revealed the similarity between Moonquakes and Marsquakes records [54] [55].

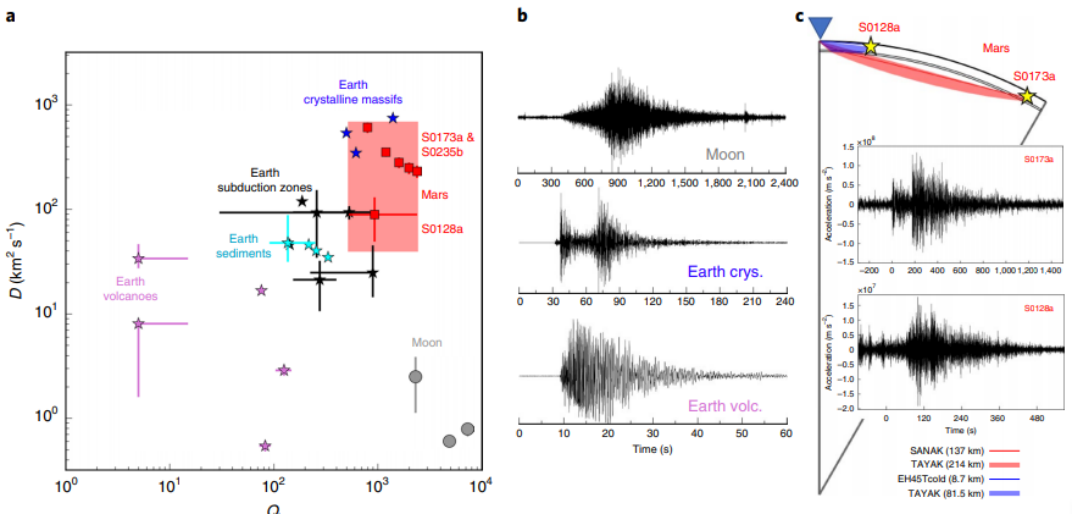

Figure 2.1 a) Diffusivity versus absorption for different seismic sources. b) Impact of geological regimes upon Lunar and Earth seismograms. c) Mars seismograms and ray paths [55].

2.3 Physical origin of Coda waves

In 1969, Aki [36] proposed the first explanation for the seismic attenuated tail waves, based upon the observation that diffraction phenomena can generate long lasting coda waves due to the heterogeneity of the upper lithosphere.

Further research showed that the diffusion approach was not the right one, as initially thought, to explain the origin and behavior of Coda waves. In the early stages, the diffusion theory was widely recognizable and acceptable especially in explosion cases [56]. The very next years, following the Nasa's Apollo project and analyzing the seismograms from the successful passive seismic experiment, deployed by the Apollo 11 mission, it became clear that Lunar seismic records, could reach the characteristic duration of almost one hour, without a specific seismic phase being noticeable. Another characteristic is that Lunar earthquake records presented slow amplitude growth, reaching the duration of 600 seconds. These observations suggested intense scattering effects and less absorption of the Lunar rock materials. The research of Dainty and Toksoz [57] [58] proposed a more like diffusion model. Although the successful utility, especially for Lunar data, this approach was taken into oblivion, as it became clear that the diffusion theory was inapplicable for the Earth's seismic records.

Later, in the study of Aki & Chouet that was published in 1975 [39], a quantitative approach was suggested for the exponential decay behavior of coda waves.

In order to overcome the problem on how the content of a high frequency seismic record can give insight information about the in-situ conditions of any local regime (local at the site of recording), Aki and Chouet proposed a small number of parameters,

capable of characterizing the average properties of the complex heterogeneous medium.

The two advanced models that were proposed were the single scattering and multiple scattering models. According to the single scattering theory, the main idea was based upon the assumption that coda waves are mainly comprised of backscattered waves that are propagating in an isotropic and homogenous medium within a weak scattering wavefield, without the potential of producing secondary scattering waves. Moreover, a single backscattering model is responsible for the generated coda waves, elucidate them as a superposition of reflected primary waves by two dimensional randomly distributed heterogeneities-scatterers.

For weak scattering observations the single approach was sufficient, instead of strong scattering cases that required the consideration of a multiple approach.

In a research presented by Hedlin and Shearer [59], an approach, using the Rayleigh-Born scattering theory, based on the single-scattering model, showed that for specific seismic wave phases, coda wave amplitudes are not sensitive to the vertical scatterers.

Despite the simplicity of the theory and some fundamental limitations, as the single scattering approach violates the energy conservation, and despite some minor additions on the theory [60] [61], this model was considered acceptable for a long time period. The mathematical analysis of this theory indicates that the radial component of energy should always be larger than the transverse and that the attenuation rate of energy is decreased as a function of time.

In addition, the single scattering model is valid in cases for mean free paths (waves between scatterers) greater that the ray path from scatterers to the receiver. This hypothesis rarely occurs in real conditions and the scatterers distribution does not satisfy the wavelength comparison size condition.

Another model that seemed to correspond well to coda wave properties, was considered the one that exhibits the multiple scattering approach introduced by Aki and Chouet, 1975 [39] Gao et al., 1983a [62]. This model described the random propagation of the seismic energy within the scattered earth's interior.

A further development of a robust model was presented by Kopnichev 1977b [63] proposed a uniform and isotropic medium, in which occurring double, triple (or higher order) of scattering phenomena, where the travel distance of the scattered waves was assumed to be larger than the epicentral distance.

This model had been further developed, in the studies of GAO et al. (1983a, b) [62].

These approaches proved to be insufficient in modeling the spatiotemporal distribution of codas energy. This problem, was about to be solved when Wu 1985 [64] [65] proposed the well-known radiative transfer equation. Mode converted waves were later introduced, as an addon in the theory [66] [67]. This theory has been extensively tested for acoustic and elastic full wave simulations by Wegler et al. 2006 and Przybilla et al. 2006 respectively [68] [69].

According to Gusev A. et. al. [70] further theoretical approach of multiple scattering process was conducted by using numerical Monte-Carlo simulation.

Contributing to this theory, the first model in history that had taken into account the energy conservation, by implementing the Monte-Carlo simulation in the three

dimensional space, verified the observed space and time distributed energy density of the high order scattered coda waves from the specification of isotropic scattering without intrinsic absorption, as a function of lapse time [71].
The radiative transfer equation (RTE) was furthermore extended for polarized waves within a potential inhomogeneous medium [72]. Weaver [73] introduced the equipartition property, as an attempt to explain the behavior of diffuse waves. According to this, despite the exponential energy attenuation of P and S waves, the ratio between them is stabilized. This property was also exhibited by the RTE equation, as the RTE predicted that between the elastic -S- waves and the primary -P- waves, the energy ratio for large lapse times (independent of the scatterers properties) is preserved.
For long lapse times, the attenuation of coda amplitude was modeled based on the theory of multiple scattering processes [71].
The difficulties to ascertain the origin of the seismic coda waves, has motivated further scientific researches in order to gain a, relatively, profound understanding of the physical procedures, on how the nature of coda waves are associated with the medium composition and tectonic structure. The dependence of the coda behavior, as a function of local site conditions, has led to the characterization of the propagation medium in terms of stochastic heterogeneities [74].
A more comprehensive approach based on observations has shown that their complex nature and behavior should be considered as a combination among scattering, absorption and site effect. Kin' ya Nishigami, suggested a relationship between the observable variation of coda wave envelope with the spatial fluctuations of scattering coefficient [75].
In conclusion, coda waves are independent of earthquake magnitude and source radiation pattern [76]. Hence, their content is mainly defined by scattering effects [49].
During the past years, more advanced, complex and hybrid approaches have been conducted to investigate and simulate the role of inhomogeneities and how they affect coda waves [77] [78].

2.4 Multi scale scatterers

According to Wu et al. [79], in order to obtain an intuitive perspective of the real complex nature of coda wave procedures, proposed the analysis of scattering phenomena in terms of source to site regimes. In this approach, considering the scale of heterogeneities as -α- and the perturbation index as $\breve{\nu}$, the wave propagation regime can be elaborated as a function of three dimensionless numbers:

1. $ka = \frac{2\pi a}{\lambda}$
2. $\frac{L}{a}$
3. $\breve{\nu}$

where the variable k represents the wavenumber, λ the wavelength within the propagation material and L the propagation length. The term kα is the normalized wave number k, and L/α the normalized propagation length. In accordance to the relatively well defined inhomogeneities, by analyzing well-log data [49], scattering phenomena can occur in one of the following regimes, as given in Table 2.1.

Quasy-homogeneous	**kα<0.01 can be considered as homogeneous due to the small size of heterogeneities**
Rayleigh scattering	kα<<1 in which the scattered power is relative to k^4
Large-angle scattering	with kα≈1 (0.1<ka<10) known as the resonance scattering case where scattering effects are dominant.
Small-angle scattering - forescattering	kα>>1 the parabolic approximation is focused the one-way wave propagation as the back scattering waves are weak.
Geometric Optics regime	kα>1, Λ<1 and ΛΦ<2π limited diffractions
Diffraction regime	kα>1, Λ>1 and Φ<2π since Λ>1 diffractions are occurred.
Saturated regime	Φ>2π and ΛΦ>2π interference between numerous of microrays

Table 2.1 Source to site regimes and scattering occurrences.

2.5 Frequency characteristics of coda waves

The frequency range of coda waves, for a broad band seismometer, can potentially cover the whole bandwidth, limited defined by the Nyquist frequency.
In the example of station CMBO, E-W component, for simplicity reasons the coda wave window has set as red line object and its associate frequency content as given in Figure 2.2 depicts the single side amplitude spectrum.

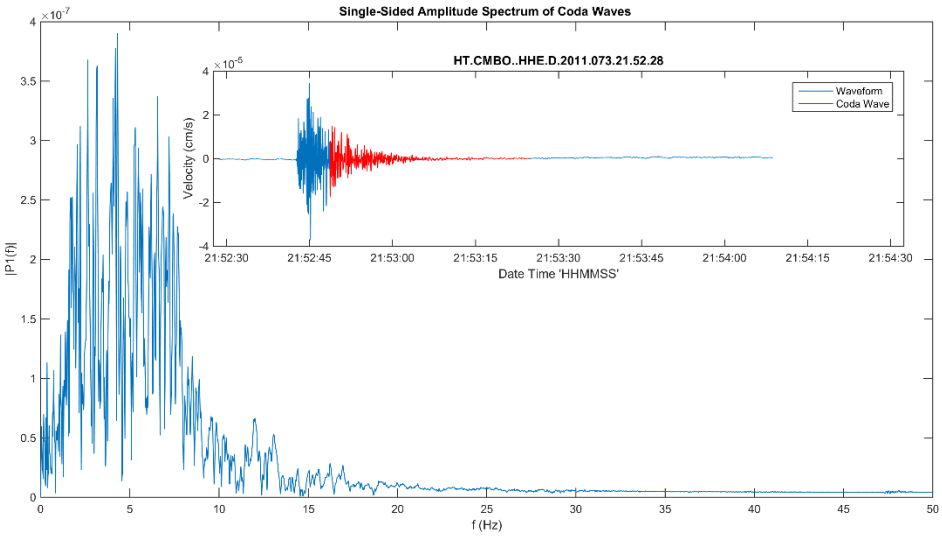

Figure 2.2 Frequency content of coda waves after the implementation of Fourier transform (CMBO station, E component).

For local events, the spectral content is strongly related with the epicentral distance. This dependence decreases as a function of time and finally it vanishes at the onset partition of coda waves [36].

From observational data analysis it was found that for spectral ratios of P (compressional), S (shear) and S-Coda, the S-Coda waves have similar spectrum to those of S-waves. In the study of Rautian and Khalturin (1978) [80] it became clear that after a well-defined duration setting by two times the S travel time, temporal decay of the energy of coda waves was found to be independent of the source and station locations, for the frequency band extended from 0.027 Hz to 40 Hz [49].

In addition, the spectrum of coda waves is decaying as a function of time without having any dependency of the source to site (station) distance and from the earthquake magnitude, at least for low magnitude earthquake events, M_L<6 [39].

Therefore, the coda excitation and attenuation depend on the local site conditions as if, for the same earthquake event, coda duration may vary up to 800% from sedimentary basins, to regions dominated by igneous and metamorphic rock materials.

The verification of coda frequencies below the frequency threshold of 1 Hz, has been found to be a very difficult procedure. In this bandwidth, alongside with scattering effects, arise a numerous of different physical phenomena, setting the isolation of these complex processes, practically impossible. Frequencies lower than 0.05 Hz are assumed to correspond to long period surface (Love and Rayleigh) wave attenuation.

For frequencies that lie above 10 Hz, coda waves are characterized by strong attenuation. This behavior of coda waves, is considered to be associated with the backscattered body waves in the deep highly Q lithosphere and are independent to the

backscattering effects of surface waves, presented from the wavefronts propagation within the inhomogeneous earth's materials [81].
The frequency band in which lithospheric scattering effects become dominant ranges from 1 Hz to 25 Hz [52].
Beyond the frequency limit of 25 Hz, the content of coda is less contaminated by surface energy [82].
The spatial distribution of a fractal-like size scatterers in the earth's interior, causes the attenuation of coda waves to follow a power law form. The attenuation of seismic waveforms as a function of frequency, expressed by the power-law form, is given by the equation:

$$Q(f) = Q_0 \left(\frac{f}{f_0}\right)^n \tag{2.3}$$

where f_0 represents a reference frequency (usually f_0=1 Hz) and Q_0 is the Q (quality factor) value in the case of $f=f_0$ [83]. In a more recent work [37], coda waves attenuation Q_c^{-1}, analyzing the decay of coda power envelope at frequency f, based on the single scattering model, can be given by the formulation:

$$P(r,t) \propto \frac{1}{t^2} e^{-Q_c^{-1} 2\pi f t} \tag{2.4}$$

2.6 Effects of seismic source and focal depth

To understand the relation between the seismic source and the recorded waveforms, a series of parameters should be defined. The rupture velocity of the fault surface, the variation of spectral and pulse shape, the energy flux around the focal sphere, the dynamic stress drop, the source to site distance and path, the local conditions - site effect, are all strong correlated on how the seismic waveforms will be recorded [84].
In the research presented by RAUTIAN, T. G., et al. [85], it became clear that as the source dimension increases, the characteristic wavelength of the generated seismic waves also increases, leading to a lower peak frequency of the spectrum, while the content of coda waves remains unaffected from the seismic moment. Coda waves have also been found to reduce the attenuation rate as the depth increases [86]. This is also an indicator that homogeneity is increasing as a function of depth.
This behavior indicates a more homogeneous media at the lower part of the earth's crust, suggesting a gradually descending correlation among the more structural complex layers of the upper brittle zone, to brittle-ductile transition zone down to crystal-plastic zone, and codas scattering effects.

Recently, in the study of Obermann et.al. [78], the impulse response was calculated by implementing parametric analysis via numerical 2D wavefield simulations upon the apparent relative velocity variation, before and after a minor velocity change, within a thin layer. The coda decay analysis verified the dependency of codas to the different degrees of heterogeneity and depth [87].

2.7 Codas index as an Earth's interior property

The spatial and temporal variations of coda waves attenuation is being identified in a variety of scientific researches, having a close relation with the occurrences of major earthquake events and volcanic eruptions [88].

The attenuation and duration of coda waves for a specific station and under specific earthquake event conditions should not deviate in time. Stress accumulation, often leads to temporal variations of many physical properties, such as fluctuations of the vp/vs ratio [89], density of materials, anisotropy [90], lithosphere-atmosphere coupling phenomena [91] etc. In the case that the accumulated energy is not expressed by aseismic fault slip (creep), the probability of the genesis of an earthquake event should be considered possible, as the physical outcome provided by the elastic rebound stress theory [92] [93]. Further investigation of coda waves decay variation was introduced by Morozov [88], as he proposed the use of the coefficient γ instead of Q_c in order to eliminate the sensitivity of the quality factor, to the inaccurate relations between the geometrical spreading as well as the anelastic dissipation and finally due to the scattering effects. During the last decades, observations have also shown uncertainties between the frequency depending quality factor Q_c with subsurface physical properties, as the two parts are not straightforward.

Nowadays, coda wave attenuation fluctuations can be considered as an index of physical and/or chemical properties variations, within a subsurface volume in a variety of tectonic regimes. According to Mak et al., 2004 [94], in active tectonic areas the Q_c value ranges below 200 (Q_C<200), while in non-active tectonic regions the Q_c value is estimated above the limit of 600. These values are in full agreement with the semi-active (moderate) tectonic regimes, in which Q_c values vary within the above limits. For active tectonic regions, Q_c values are reduced for frequencies between 0.1 Hz and 25 Hz [39].

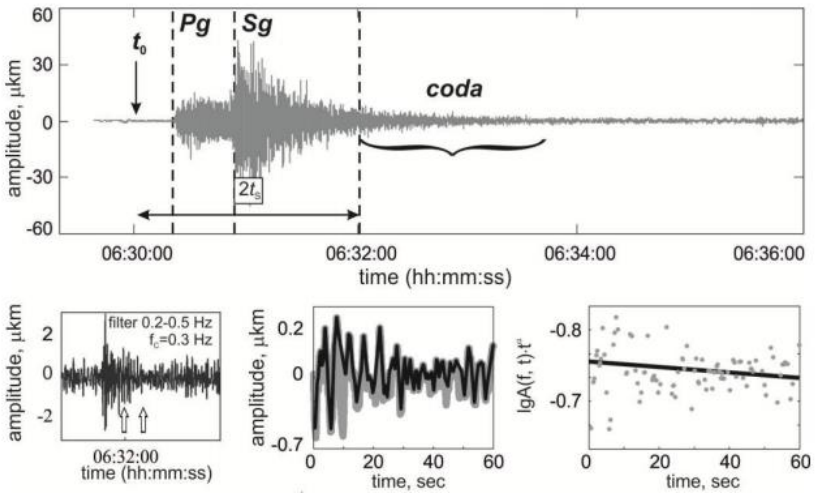

Figure 2.3 Analytic procedure of Q_c evaluation. The left column depicts filtered seismograms. The middle column consists of time segments of filtered coda in time windows of 60 sec. The grey line object represents the time domain waveform, while the black line object represents the envelope based on peak amplitudes. Coda wave amplitudes versus time and fitting regression line for Q_c calculation is given in the right column [95].

The temporal fluctuations of coda waves quality factor have attracted a variety of different approaches, in an effort of emerging an integrated and unified theory of understanding the Earth's interior physical properties. Towards this direction, a significant contribution has been made via the statistical mechanics approach by implementing the generalized framework, as it was proposed by Tsallis [96], known as non-extensive statistical mechanics. In a series of work [97] [98] [1] and by analyzing coda wave increments and seismic noise increments, it became clear that coda waves as well as seismic noise, contain the required information to study changes in the scatterers density-orientation-distribution, as the physical properties of the earth's interior medium, are dynamically developing.
As a result, monitoring coda wave tails by analyzing its frequency content, as well as the decay rate and the standardized increments, can also be used as a precursor index of physical properties variation or even for a potential genesis of a major earthquake event or volcanic eruption [99].

2.8 Coda wave duration

The determination of the coda wave's duration was first associated with the sample point (in time domain), where the amplitude decay starts to behave non-exponentially. On a later stage, a more quantitative approach was introduced, by measuring the travel time between the origin time and the S-phase onset. This duration, after being

multiplied by a factor of two and in some cases by a factor of three, is considered to be the start point of the coda wave [80]. The end of the coda wave duration is assumed to be placed when the signal to noise ratio, SNR, reaches a specific value, set by the user. Usually this factor is set between 1 and 3. This value can be set after taking into consideration the local geotectonic regime, the background noise and any kind of in-situ physical site properties.

The coda wave's duration for volcano-tectonic type, short period (high frequency) seismic events, has also been found to be related with the earthquake magnitude (M_L) [100]. In such cases, empirical laws can be applied in order to retrieve information, both in earthquake magnitude and coda wave duration.

For small earthquake magnitudes, coda wave lengths cannot be considered as a stable estimation, due to the fact that it is not possible to measure backscattered energy from large distances, as discussed in the research of Aki and Chouet 1975 [39].

In other approaches, coda-length, considered as the range between the P-wave arrival and the point, in time, in which the coda peak-to-peak amplitude, reached a specific value [101].

For ideal cases, where the coda waves envelope is characterized with monotonic decay, and seismic stations are located upon bedrock with little to none sedimentary cap, an empirical relation can be produced as an index of the coda waves duration.

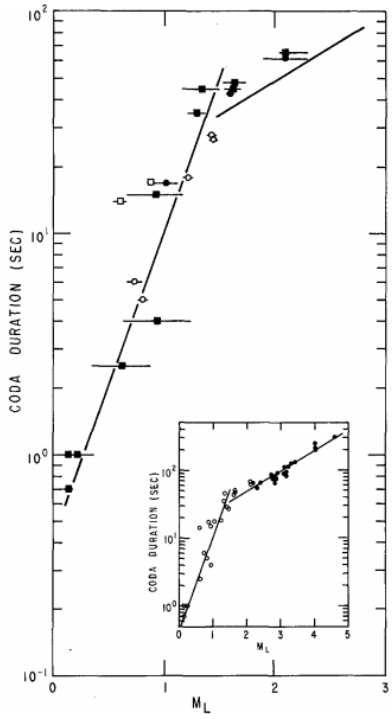

Figure 2.4 An empirical relation for codas duration as a function of local magnitude. The threshold of 40 sec is considered as the point that slope changes. (data retrieved from OKAT station of USGS) [46].

In the empirical relation, resulting by linear regression as seen in Figure 2.4, there is no biased variation between the coda waves duration and local magnitude for different epicentral distances and focal depths.

3 Introduction to statistics

In this dissertation we tried to evaluate the dynamical evolution through the natural processes that govern the wider area of the Santorini's caldera, by investigating the systems' entropy, risen by pure instrumental seismological observations. For that purpose, a profound understanding of how the basic concepts of statistics are associated with the wider study of seismology is mandatory, as well as the transition from statistical mechanics to the generalized framework of non-extensive statistical mechanics-physics (NESM theory).

3.1 Statistical analysis parameters

In the field of statistics, there are two different approaches while working with population and sample data. When the whole population is given, each data point is well determined, but when we investigate a sample of the whole population, it is interpreted as an approximation of the population parameter. For that reason, all formulas are algebraically adjusted to reflect this statistical issue.
The most fundamental parameters in statistics are the mode, median, mean, range, variance and standard deviation. These parameters provide us numerical information about the distribution of any given dataset. The three first parameters (mode, median and mean) refer to the center or central tendency, while the range, variance and standard deviation are measures of spread. More specifically, the mode refers to the data value that is presented most frequently, the median refers to the value that is positioned in the middle of the given ordered dataset and mean is referred to the arithmetic average, while the range can be calculated as the difference between the maximum and the minimum value [102].
The variance measures the dispersion around the mean value. Population variance, denoted as σ^2, is given by the equation:

$$\sigma^2 = \frac{\sum_{i=1}^{N}(x_i - \mu)^2}{N} \qquad (3.1)$$

In addition, sample variance is denoted as S^2 and is given by the formulation

$$s^2 = \frac{\sum_{i=1}^{n}(x_i - \bar{x})^2}{n-1} \qquad (3.2)$$

where N and μ refer to the total number of observations, while n and $\bar{x}$ to sample observations. Consequently, there are population and sample standard deviation. These formulas are the square root of the population variance and square root of the sample variance respectively.
The standard deviation is given by the relation:

$$s = \sqrt{\frac{\sum(x_i - \bar{x})^2}{n-1}} \qquad (3.3)$$

In the scenario of two different datasets, the comparison between them cannot be determined by standard deviation, since it is the measure of variability for a single data set. This statistical problem can be overcome with the utility of the coefficient variation, as an indicator of how close the values are to the mean, in any given dataset.

$$\widehat{c_v} = \frac{s}{\bar{x}} \qquad (3.4)$$

3.2 Gaussian (Normal) distribution

The Gaussian distribution is also known as the 'bell shaped curve' due to its symmetric curve (symmetrical about the mean).
In this type of distribution, the y-axis represents the relative probability of an independent variable that is always centered on the average value.
The width of any curve is defined by the standard deviation. Small values of standard deviation lead to narrow curve bell shapes (Figure 3.1 right). There is a vast number of physical phenomena whose behavior follow the normal distribution. This happens because of the central limit theorem and due to the fact that no matter how many measurements are being conducted, the mean values are always normally distributed. In addition, means calculated from samples taken from a specific uniform distribution (like exponential) are normally distributed. The Cauchy distribution does not need a sample mean; hence it is not limited to a large sample size for the central limit theorem to be valid.
We can use the mean's normal distribution to make confidence intervals, conduct t-student's tests to find a potential difference between the means between two samples and ANOVA (analysis of variance) if we want to find differences among three or more samples.

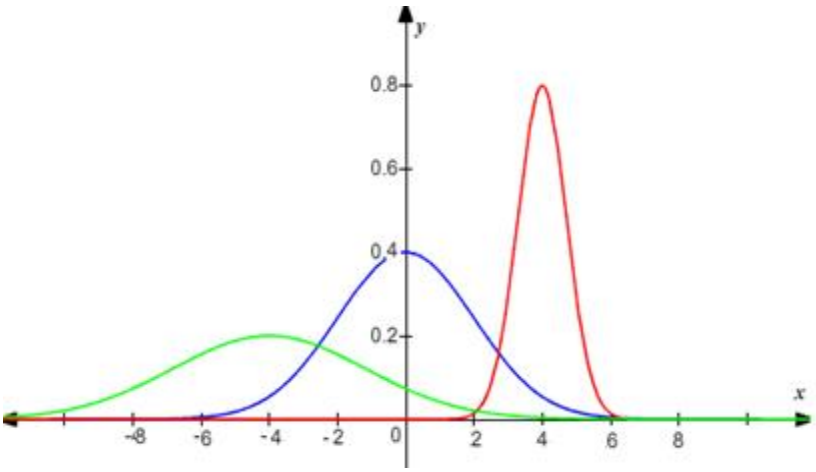

Figure 3.1 Three different normal distributions depicted with different colors. The green line object refers to gaussian distribution with mean value equal to -4 and standard deviation 2 (left). The blue (central) line object refers to normal distribution with mean value 0 and standard deviation 1. Lastly, the red line object (right) has a mean value of 4 and standard deviation equal to 0.5.

In the probability theory, the Gaussian distribution (also known as normal or Laplace-Gauss distribution) is a type of a continuous probability distribution and it is expressed as:

$$f(x) = \frac{1}{\sigma\sqrt{2\pi}} e^{-\frac{1}{2}\left(\frac{x-\mu}{\sigma}\right)^2} \tag{3.5}$$

where μ represents the mean, median and mode of the distribution and σ the standard deviation.
The probability of a random variable having a specific value x_i or exists within an interval of dx, in case of discrete and continuous case respectively, is given by the functions of the random variable X. For the discrete case, the function is known as probability mass function and is given by the relation:

$$f_x(x_i) = P(X = x_i) \tag{3.6}$$

that meets the requirements:

$$f_x(x_i) \geq 0 \tag{3.7}$$

and

$$\sum_{i=1}^{m} f_x(x_i) = 1 \tag{3.8}$$

In case of a continuous random variable X, the function is known as probability density function, and follows the conditions

$$f_x(x) \geq 0 \tag{3.9}$$

and

$$\int_{-\infty}^{+\infty} f_x(x)dx = 1 \tag{3.10}$$

The probability distribution of the random variable X can be determined by the cumulative distribution function $F_x(x)$, indicating the probability of the random variable X of getting values smaller than or equal to a specific x value. For a discrete variable X, we have:

$$F_X(x_i) = P(X \leq x_i) = \sum_{x \leq x_i} f_x(x) \tag{3.11}$$

and for continuous random variable X, the formulation is transposed into:

$$F_X(x) = P(X \leq x) = \int_{-\infty}^{+\infty} f_x(u)du \tag{3.12}$$

The normal distribution is universally unimodal. Its curve is symmetric about the mean value and can be fully characterized by the μ and σ parameters. The notation that is given to a population that follows a normal distribution can be written as:

$$X \sim N(\mu, \sigma) \tag{3.13}$$

Another universal characteristic is that within one standard deviation away from the mean value, the covered area is approximately about 68%. Within the range of two

standard deviations the area reaches the amount of 95%. Furthermore, in the interval of three standard deviations away from the mean, the occupied area is being increased to the percentage of 99.7%. Consequently, we can continue the range of standard deviation with a reciprocal covered area. Since it is never touching the x-axis, the normal distribution will continue to infinity with an arbitrary standard deviation, but in such a case, the probability of an outlier data point will end up close to zero, which is inherently absurd in many natural systems.

3.3 Skewness and Kurtosis

The most common tool, used to measure the asymmetry of any unimodal curve is the skewness which is given by the relation

$$Sk = \frac{\frac{1}{n}\sum_{i=1}^{n}(x_i - \bar{x})\text{^}3}{\sqrt{\frac{1}{n-1}\sum_{i=1}^{n}(x_i - \bar{x})^2}^3} \qquad (3.14)$$

The direction of the skew might be abstract and counterintuitive due to the fact that it does not reflect on which side the line is leaning to, but to where the tails are leaning to.

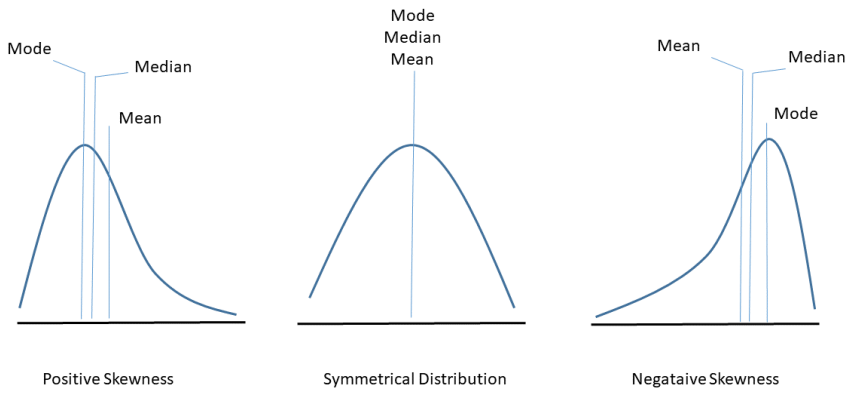

Figure 3.2 (Left) In the case of right or Positive Skewness, the tail on the right is longer or fatter. For positive skew, the mean value is bigger than the median, while the mode is located at the peak of the distribution. (Center) A normal distribution with ideal symmetrical tails. (Right) Left or negative Skewness exhibits longer or fatter left side tail.

The skewness is considered as the degree of distortion, deviating from the initial symmetrical bell-like curve (normal distribution) as it differentiates the extreme outliers on the left side as a function to the right tail and vice versa.
In addition, the behavior of flatness of any given distribution, by taking into consideration extreme values within the tails, can be measured via kurtosis. In the case of normal distribution, the kurtosis is called Mesokurtic curve. while Leptokurtic curve refers to a type of distribution that is peaked higher that Mesokurtic. Additionally, platykurtic curve shape depicts lower peak and has shorter tails due to the fact that they exhibit outlier's paucity [103].
The mathematical approach of kurtosis is given by the relation:

$$Ku = \frac{\frac{\sum_{i=1}^{N}(Y_i - \bar{Y})^4}{N}}{\sqrt{\frac{1}{n-1}\sum_{i=1}^{n}(x_i - \bar{x})^2}^4} \qquad (3.15)$$

3.4 Statistical overview in Seismology

3.4.1 Power law in nature

The power-law distribution is applicable in multi-discipline scientific areas of many physical, chemical, social as well as biological phenomena [104]. In the last decades, scientific research has shown an incredible similarity of statistical behavior, among relatively irrelevant phenomena such as city populations [105] [106] [107], normal immune receptors [108], the frequency of words we use in our lifetime (oral and written) [109] [110] [111] [112], predator strategies and forage pattern in many different species [113], similarity of protein structure sequences [114], gamma-ray intensity of solar flares [106], road and websites traffic as well as citation number of academic researches [115] [106], engaging neural patterns [116], the scale (diameter) distribution of Lunar craters [117], the loss of souls in wars [106], the popularity of opening chess strategies [118], the frequency at which our complex structured brain forgets [119] and of course in earthquake magnitudes and the dissipated release of energy [106] [120] [115] [121].
Whether the systems (phenomena) under investigation are natural, or human made, even biased, almost every time the behavior of power law emerges. This characteristic was first introduced by George Kingsley Zipf. The Zipf distribution is related to the discrete power law Pareto distribution and the Riemann zeta distribution [122] [123].
Pareto distribution, also known as the power law distribution, is given by the formula

$$\Pr(X > x) = \bar{F}(x) = \left(\frac{x_{min}}{x}\right)^{a} \; for\; x \geq \; x_{min} \tag{3.16}$$

3.4.2 The Power Law in Seismology

The empirical Gutenberg and Richter (G-R distribution) scaling relation [124] indicates a power law behavior in earthquake population, as seen in equation (3.17):

$$\log N(N > M) = a - bM \tag{3.17}$$

where N (N>M) represents the cumulative number of earthquakes with magnitude greater than or equal to M and the a-value represents the total seismicity rate of the given region under investigation. The -a- value is associated as the intersection of the linear regression model with y-axis (log N). The b parameter, known as the b-value, represents the proportion of small to large earthquake events. The maximum likelihood solution of the b-value is given by the relation (3.18) [125]:

$$b = 1/\log(10)(\bar{M} - M_c) \tag{3.18}$$

where $\bar{M}$ is the observed mean magnitude and M_c the completeness magnitude.
The generalization form, as presented from [126], is expressed as

$$logN_{>m} = logN + \left(\frac{2-q}{1-q}\right) log\left[1 - \left(\frac{1-q}{2-q}\right)\left(\frac{10^{2m}}{a^{2/3}}\right)\right] \tag{3.19}$$

where -a- is a proportional constant, N remains the total number of events and q stands for the non-extensivity parameter (analytic of non-extensive approach within the next chapter).
The equivalent power law expression of G-R distribution, can be written as

$$N(> M) = 10^{a-bM} \tag{3.20}$$

As a result, the Gutenberg and Richter law implies power-law dependence between the number of earthquakes and magnitude. If we expand the law in terms of energy, then the equation can be written as:

$$N(>E) \sim E^{-\beta-1} \tag{3.21}$$

In this relation, the parameter β has been found to be 2/3 of the b-value [127]. This form, expresses the scale invariance of the magnitude and seismic energy distribution. Furthermore, seismic energy in terms of the seismic moment, is related to the surface fault area according to the equation

$$M_0 = \mu \Delta A \tag{3.22}$$

where M_o represents the seismic moment, μ the rigidity or the shear modulus, Δ the average relative slip of the fault plane [128] and A the surface area of fault. The physical approach of these equations implies that the population of earthquake events with rupture surfaces greater than a specific size A, has a power law dependence of that area (noted as A). This kind of dependence exhibits that the Gutenberg and Richter law has a fractal distribution behavior [129] [121].

Fault structures and fault distributions depict self-similarity, indicating the scale invariant property. Nevertheless, this scale invariance is confined into a narrow finite range of scales that are strongly correlated with the size of the volume under stressed.

As a result, the dynamical fault-population evolution, from fractures and microcracks to large scale faults, indicates a transition from power law and fractal behavior, carrying the memory property, to exponential and memory-lessness, where the non-linearity arises as a function of the accumulated stress [130] [131] [132] [133].

This power law scaling and the exponential behavior has been observed in many scientific researches [134] [131], expressed by the equations (3.23) and (3.24), respectively [121]:

$$N(>L) = AL^{-D} \tag{3.23}$$

where N represents the number of linear faults with size greater that L and D the power-law exponent.

$$N(>L) = Ae^{\left(\frac{-L}{L_0}\right)} \tag{3.24}$$

In the exponential form, L_0 represents a specific length [135]. In both forms, A represents a scaling constant.

Furthermore, the coda wave amplitude attenuation also decreases as a function of power-law, as they exhibit time lapse dependence from the origin time [136].

This power-law behavior of the coda amplitude decay, is inherited as the scattering coefficient decreasing with depth.

The elucidation of the frequency dependence of the coda wave amplitude decay, can be attributed on a power-law scatterers sized distribution.

All these properties, derived from purely observational processes, are indications of nonlinear dynamical procedures throughout the evolution of earthquakes phenomena.

4 Introduction to Statistical Mechanics and the concept of Entropy

4.1 A general Introduction

Statistical mechanics can be described as the mathematical keyhole, in order to understand the physical processes and the dynamical evolution of complex systems, from the specification of the microstate constituents to the macrostate scale. The common interpretation of Entropy is often associated as a measurement of disorder, but the true nature of entropy lies in the probability theory. For a given material, the distribution of the stored energy within its molecular bonds, expresses the total amount of entropy. According to the Statistical mechanics, for a given set of large-scale observable properties, every probable configuration of particles that could potentially result those properties, has the same probability [137] [138]. The term configuration is referred to determine the exact arrangement of any physical characteristic, such as position, velocity, momentum spin (any degree of freedom that can characterize the system under examination) of the microscopic constituents. Each of these possible distributed configurations of energy, are called microstates. On the contrary, the macrostate exhibits the specific combination of large-scale macroscopic properties which are entirely defined by the properties of thermodynamics (pressure, temperature, volume etc.). Consequently, the majority of every potential microstate configuration that statistically emerges for a specific macrostate, has the same probability to be observed.

The inevitability of a system to maximize its entropy is fundamental in statistical mechanics and is derived from the second law of thermodynamics [139] [138].

The nature of entropy emerges in the second law of thermodynamics from the specification of how particles is distributed under the laws of motion. As a result, entropy can explain the thermodynamic behavior of a system, by taking into account the summed result of motion of individual particles, in the specification of Newton's motion laws.

According to the second law of thermodynamics, any physical system started on an inexorable path of increasing its entropy. This property of entropy can be considered as a fundamental, induced property of the forward directivity of time. This concept is not derived from any classical physics or quantum mechanics equations.

Newton's second law and the of law of universal gravitation are given by the equations (4.1) and (4.2), respectively:

$$F = ma \qquad (4.1)$$

$$F_G = -\frac{G_{m_1 m_2}}{r^2}\hat{r} \tag{4.2}$$

The quantum wave function is given by the linear partial differential equation, known as the Schrodinger equation:

$$i\hbar\frac{\partial}{\partial t}\Psi = \frac{-\hbar^2}{2m}\nabla^2\Psi \tag{4.3}$$

where Ψ represents the value of the wavefunction throughout space and time.
At each point in the 3-dimensional space, the complex number of $\nabla^2\Psi$ is given by:

$$\nabla^2\Psi = \frac{\partial^2\Psi}{\partial x^2} + \frac{\partial^2\Psi}{\partial y^2} + \frac{\partial^2\Psi}{\partial z^2} \tag{4.4}$$

Even though the behavior of all subatomic particles is inherently probabilistic, the equation (4.3) does not lie in probabilities. The probability of every possible observation is determined by the wave function, but prior to the observation, the wave function is deterministically evolving-changing. That kind of behavior is never presented on how energy is dissipated and scattered in space-time.
Consequently, entropy is a direct measure of each energy configuration's probability and can be intuitively thought as a measurement of the energy distribution. Low entropy indicates concentrated energy. On the contrary high amount of entropy explains the maximum distribution of the energy. In order to understand the concept of entropy, a dynamical system that changes in time is mandatory. In our case, the genesis of an earthquake, triggers the energy distribution within the earth's interior. The propagation of the seismic body waves, P and S, is responsible for the continuous transfer of the energy between bonds within the crystal lattice and atomic bonds, through the Earth's materials. Hence, as the energy transfers, its configuration is constantly changing. Because of the scattered microstates, the most likely probability is the one where the energy distribution will be dispersed, resulting to a higher entropy for the system. In a large-scale system, the higher entropy is always statistically more likely to occur.
Furthermore, an analogy to understand the concepts of microstate and macrostate, is to think about the spatial distribution of an aftershock sequence that follows a major earthquake event. The recorded seismic events are randomly spatially distributed, or following a fractal like geometry [140]. The individual events occurrences of the aftershock sequence represent the microstate of the system and the density of the

spatial cumulative number of event distribution, obtained by 2D interpolation, can be considered as the macrostate of the system.

To recapitulate, if we think about all the random possible configuration of seismicity, the majority of the potential microstates should correspond to the same macro-state, while any clustered distribution, not following (pre)existing tectonic features (narrow scattered seismicity) should not. As a result, distributed hypocenters within the rupture area are characterized by high entropy.

Our human being sensing limitations cannot determine the overall observable microstates of an existing system; hence we can gain a robust overview via statistics.

As a consequence, the normal outcome of any physical system is that the vast majority of any possible microstate distribution will leave the system very close to a single macro-state, the state of thermal equilibrium.

In many physical phenomena, instead of investigating how particles are being distributed within the three-dimensional space, the microstate is well defined from how the energy is distributed through phase space [141] [142]. Hence, the thermodynamic properties of a given system are defined by the average distribution of particles in phase space.

Phase space is very crucial for the evolution of dynamical systems, as it can estimate the Lyapunov characteristic exponent, an index that quantifies the degree of sensitivity with respect to initial conditions [143].

Processing records, retrieved from time series, can lead to false founding of positive maximal Lyapunov exponent, due to the noise content (analog to digital process, system noise etc.). This procedure can enhance the sensitivity to initial conditions leading to false trigger findings that characterize a system as chaotic, even if it is purely stochastic or semi-deterministic.

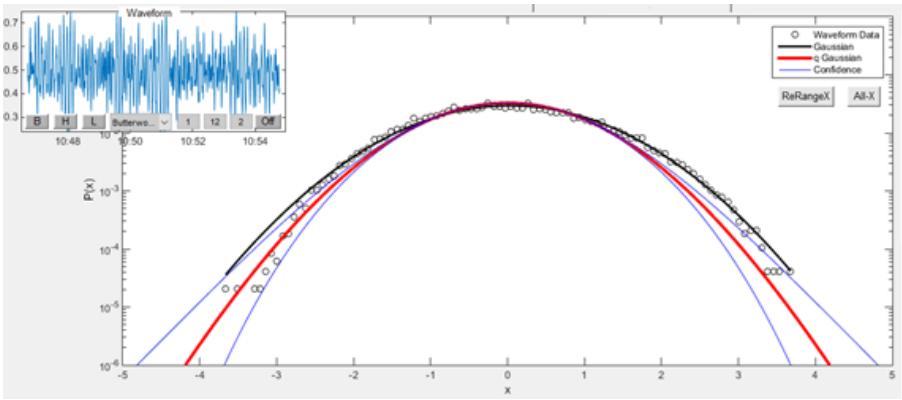

Figure 4.1 An example of coda wave increments containing white gaussian noise, following a gaussian like distribution (q→1).

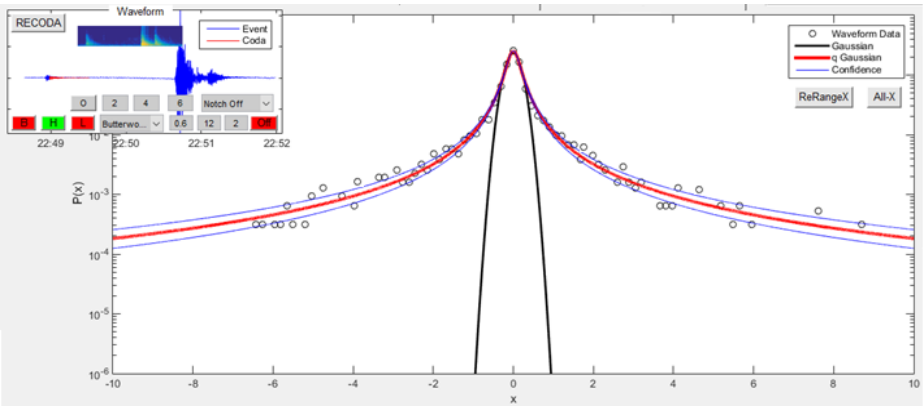

Figure 4.2 Pure coda wave increments, exhibiting fat tailed characteristics (long memory effects) following a q-gaussian distribution (q→2.1) (explanation of q-gaussian distribution within the next chapter). Station CMBO | Time: 2011 346 22:50 (YYYY JJJ HH:MM).

4.2 Boltzmann Gibbs Statistical Mechanics

When systems under examination are large enough in size, the small-scale exact states are transposed into large scale average states, by assigning probabilities to the system being in different states.
The once false explanation and status quo of the physical fluid known as caloric [144], according to which it was responsible for the heat flow, superseded by the thermodynamics approach and Ludwig Boltzmann, founder of the statistical mechanics.
Entropy, based on the second law of thermodynamics, exhibits the relation between the microscopic and macroscopic states. This relationship is given by the formula (4.5)

$$S = -k \sum_i p_i log p_i \tag{4.5}$$

where $0 \leq P \leq 1$, Σ is the sum of all state probabilities marked as p_i and k represents a positive constant, which in the field of thermodynamics expresses the Boltzmann's constant (K_B =1.38*10^{-23} J/k). This equation (4.5) is referred as the Boltzmann's Gibb's entropy S_{BG}.
In the case in which all probabilities are equal,

$$p_i = \frac{1}{W} \quad , \forall i \tag{4.6}$$

the eq. (4.5) can take the form of equation (4.7)

$$S = k\, ln\, W \tag{4.7}$$

This formulation of entropy corresponds to the specific case, where all microstates of a given system have equal probability of occurrence and as the microstates increase, the higher the entropy will be.
For continuous variable x, the eq (4.5) is given by:

$$S = -k \int_0^\infty p(x) \ln p(x)\, dx \tag{4.8}$$

The most likely macroscopic state can be retrieved by the maximization of entropy, subject to the normalization of p(x) constraints:

$$\int_0^\infty p(x)dx = 1 \tag{4.9}$$

The average x value is given by:

$$\langle x \rangle = \int_0^\infty xp(x)dx \tag{4.10}$$

In accordance to the previous defined constraints and by using the Lagrange multiplier method, the probability that maximizes the Boltzmann's Gibb's takes the form of the Boltzmann distribution:

$$p(x) = \frac{e^{-\beta x}}{\int_0^\infty e^{-\beta x} dx} \tag{4.11}$$

where $e^{-\beta x}$ represents the Boltzmann factor and β stands for the Lagrange multiplier.
If we combine two independent sub-systems A and B with its states, noted as W_A and W_B respectively, in such a way that their conjugated probabilities satisfy the relation (4.12):

$$p_{ij}^{A+B} = p_i^A p_j^B \big(\forall (i,j)\big) \tag{4.12}$$

then the entropy S_{BG} is called additive. This property can be mathematically expressed by the following relations:

$$S_{BG}(A+B) = -k\sum_{i=1}^{W_A}\sum_{j=1}^{W_B} P_{ij}^{A+B} \ln P_{ij}^{A+B} \tag{4.13}$$

$$S_{BG}(A) = -k\sum_{i=1}^{W_A} p_i^A \ln p_i^A \tag{4.14}$$

$$S_{BG}(B) = -k\sum_{j=1}^{W_B} p_j^B \ln p_j^B \tag{4.15}$$

The Boltzmann-Gibbs entropy is the basis of the classical Boltzmann-Gibbs statistical mechanics, from which the Boltzmann distribution emerges for the case of thermal equilibrium.
Boltzmann-Gibbs entropy and distribution are benchmarks of statistical mechanics for a variety of natural phenomena and procedures.
One of the most important properties of S_{BG} entropy is the non-negativity. If we assume a specific probability then we can assume that:

$$\lim_{x\to 0}(xlnx) = 0 \tag{4.16}$$

$$S_{BG} = -k\langle lnp_i\rangle = k\, ln\langle\frac{1}{p_i}\rangle \tag{4.17}$$

The amount of lnp_i and $\ln(1/p_i)$ represent the mean value of probabilities under examination.
The entropy is always positive since:

$$\ln\left(\frac{1}{p_i}\right) > 0(\forall i) \tag{4.18}$$

S_{BG} is always maximizing the entropy. For a given set of probabilities p_i and p_i', correlated in a system of W states, the S_{BG} will reach its maximum state in the case of:

$$S_{BG}(\{p_i''\}) > \lambda S_{BG}(\{p_i\}) + (1-\lambda) S_{BG}(\{p_i'\}) \tag{4.19}$$

where pi'' probability set has the property of:

$$p_i'' = \lambda p_i + (1-\lambda) p_i' \ (\forall\ i\ 0 < \lambda < 1) \tag{4.20}$$

The above property derives from the second law of thermodynamics and mathematically implies that when the system is under equilibrium, the entropy acquires its maximum value.
The extensivity of Boltzmann Gibbs entropy is taken into consideration when the limit of equation (4.21) exists:

$$\lim_{N\to\infty} \frac{X(N)}{N} \tag{4.21}$$

With:

$$X(N) \propto N(N \to \infty) \tag{4.22}$$

where X (physical quantity) is proportional to the system size. In such cases and for systems whose elements are not correlated to each other, the entropy of Boltzmann-Gibbs is considered as extensive:

$$S_{BG}(N) \propto N \tag{4.23}$$

and

$$0 < \lim_{N\to\infty} \frac{S_{BG}(N)}{N} < \infty \qquad (4.24)$$

4.3 q - Functions

On the contrary, when the elements of systems under examination are strongly correlated (long range interaction, long memory etc.), then the entropy cannot be further characterized as extensive. In addition, the Boltzmann-Gibbs entropy cannot be considered as a universal form, due to the fact that it is not applicable for systems whose elements are correlated. By expanding the area of S_{BG}, we can assume the following differential equations and their solutions y [145] [146]:

$$\frac{dy}{dx} = 0\ ,\ y(0) = 1\ \text{ , y = 1} \qquad (4.25)$$

$$\frac{dy}{dx} = 1\ ,\ y(0) = 1\ \text{, y = 1 + x} \qquad (4.26)$$

$$\frac{dy}{dx} = y\ ,\ y(0) = 1\ \text{, y = } e^x \qquad (4.27)$$

Combining these differential equations and by taking into consideration the concept of linearity, the q-parameter is produced.

The equation (4.28) is a mathematical solution approach of the Cauchy problem [147]:

$$\frac{dy}{dx} = y^q\ , y(0) = 1 \qquad (4.28)$$

The non-linear differential equation (4.28) has an analytic solution [147] for the case of q≠1:

$$\frac{dy}{dx} = y^q \Leftrightarrow \frac{dy}{y^q} = dx \tag{4.29}$$

$$\Leftrightarrow \int \left(\frac{1}{y^q}\right) dy$$

$$= \int dx + c \Leftrightarrow \int y^{-q}\, dy = x + c$$

$$\Leftrightarrow \frac{1}{1-q}\int (1-q)y^{-q}\, dy = x + c \Leftrightarrow \frac{y^{1-q}}{1-q} = x + c$$

$$\Leftrightarrow y^{1-q} = (1-q)(x+c) \Leftrightarrow y(x) = \big((1-q)(x+c)\big)^{\frac{1}{1-q}}$$

In addition, for the case of y(0) = 1 we have:

$$[(1-q)c]^{\frac{1}{1-q}} = 1 \Leftrightarrow (1-q)c = 1 \Leftrightarrow c = \frac{1}{1-q} \tag{4.30}$$

When c = 1/(1-q) the solution of (4.28) can be given by the equation:

$$y(x) = [1 + (1-q)x]^{\frac{1}{1-q}}\ , y(0) = 1, \qquad q \in R,\ \ q \neq 1 \tag{4.31}$$

By analyzing the properties derived from this class of functions, we can produce an analytic overview of the well-known q-exponential, q-logarithmic and q-gaussian functions.

For the q-exponential function we assume the relation (4.31), as given above, and that the limit of the q index tends to 1. Then the equation (4.28) can be analyzed into:

$$\lim_{q\to 1} e_q^x = \lim_{q\to 1}[1 + (1-q)x]^{\frac{1}{1-q}} = \lim_{q\to 1} e^{ln[1+(1-q)x]^{\frac{1}{1-q}}} \tag{4.32}$$

$$= \lim_{q\to 1} e^{(1-q)^{-1}\ln(1+(1-q)x)} = e^{\left[\lim_{q\to 1}(1-q)^{-1}\ln(1+(1-q)x)\right]}$$

$$= e^{\left[\lim_{q\to 1}\frac{\ln(1+(1-q)x)}{1-q}\right]} = e^{\left[\lim_{q\to 1}\frac{\frac{\mathrm{d}}{\mathrm{dq}}\ln(1+(1-q)x)}{\frac{d}{dq}1-q}\right]}$$

$$= e^{\left[\lim_{q\to 1}\frac{\left(\frac{1}{(1+(1-q)x)}\right)\frac{d}{dq}[1+(1-q)x]}{-1}\right]} = e^{\left[\lim_{q\to q} -\frac{x}{-1}\right]} = e^{\left[\lim_{q\to 1} x\right]}$$

$$= e^x$$

Therefore, for the case of q→1, we have:

$$e_q^x = e_1^x = e^x \tag{4.33}$$

This category of e_q^x functions represents the q-exponential class and for every single value of q index, emerges a unique q-exponential function.
In addition, the q-exponential distribution can be described by the probability density function of:

$$p(x) = p_0 \left[1 - (1-q)\frac{x}{x_0}\right]^{\frac{1}{1-q}} \tag{4.34}$$

For the case of q→1, the equation (4.34) recovers the simple form of the exponential distribution, as the q-exponential function recovers the exponential function in the limit of q→1.

This form of q-exponential distribution can be considered as a Zipf-Mandelbrot generalization [148]. In the case of q>1, the q-exponential distribution displays an asymptotic power law, while in the case of 0<q<1 a cutoff appears [149]:

$$X_c = \frac{1}{1-q}\beta_q \tag{4.35}$$

The inverse solution of equation (4.31) emerges the q-logarithmic functions class [147]. If we assume the relation:

$$y = [1 + (1-q)x]^{\frac{1}{1-q}} \Leftrightarrow y^{1-q} = 1 + (1-q)x \Leftrightarrow x = \frac{y^{(1-q)} - 1}{1-q} \tag{4.36}$$

then, the inverse of (4.31) is given by the equation:

$$y^{-1}(x) = \frac{x^{1-q} - 1}{1-q} \equiv ln_q x, \qquad x > 0, \qquad q \in R \tag{4.37}$$

For the inverse of e_q^x and analyzing [147] the case of q→1

$$\lim_{q\to 1} ln_q x = \lim_{q\to 1} \frac{x^{1-q}-1}{1-q} = \lim_{q\to 1} \frac{e^{lnx^{1-q}}-1}{1-q} \qquad (4.38)$$
$$= \lim_{q\to 1} \frac{\left(e^{lnx^{1-q}}-1\right)lnx}{(1-q)\,lnx} = lnx\left(\lim_{q\to 1} \frac{\left(e^{lnx^{1-q}}-1\right)}{(1-q)\,lnx}\right)$$
$$= lnx\left(\lim_{q\to 1} \frac{\frac{d}{dq}\left(e^{lnx^{1-q}}-1\right)}{\frac{d}{dq}(1-q)\,lnx}\right)$$
$$= lnx\left(\lim_{q\to 1} \frac{-(1-q)lnx\, e^{1-q\,lnx}}{-lnx}\right)$$
$$= lnx\left(\lim_{q\to 1}(1-q)e^{lnx^{(1-q)}}\right) = lnx\,, \qquad x>0,$$
$$ln_1 x = lnx$$

The q-logarithm function is non-additive because of the mixing terms that appear in the case of summation of two independent q-logarithms of A and B terms.

$$ln_q x_A x_B = ln_q x_A + ln_q x_B + \left[ln_q x_A ln_q x_B\right] \qquad (4.39)$$

This property is called pseudo-additivity.

4.4 Non extensive statistical mechanics

Statistical mechanics and its associated concept of entropy were initially applied exclusively in the field of classical thermodynamics and the kinetic theory of gasses [121]. Later, it expanded to other scientific disciplines, in order to provide a principle for inferring the least biased probability distribution from limited information [139].
Scientific research [150] [151] has shown that empirical laws with simple forms seem to correspond well to the collective properties of either earthquake or fault population. The approach of statistical mechanics in these two specific fields of earthquake and fault population can be considered as the link between the transition from the micro-cracking and fracturing within the upper rigid crust, to the genesis of a significant earthquake event, expressed by a fault rapture [152].

Toward that direction, the generalized framework of non-extensive statistical physics, based on the concept of entropy, has also been used to explain some of the complex seismological dynamic processes, such as the change of local scattering evolution, by analyzing coda waves and seismic noise of seismographic stream records [98] [1].
In a more general form, it can be used in order to estimate the macroscopic configuration of the seismological occurrences, such as earthquakes, evolution of faulting, time intervals of aftershock sequences, time domain samples increment etc. [98] [153] [121], from the specification of the relevant microscopic components and their interactions [154].
The true nature of such complex systems implies that the occurrence of an individual constituent is strongly correlated with the state and the occurrence of some other micro-constituent.
BG statistical mechanics corresponds well to physical systems that presents short-range interactions and short memory, found in Markovian chain processes [155]. However, for the macroscopic behavior of physical systems whose elements present weak chaotic dynamics, the Boltzmann-Gibbs-Shannon approach has limited applicability. These systems, violate essential properties of the Boltzmann's Gibb's distribution [156], as they follow distributions with asymptotic power law behavior, exhibiting long-range interactions, long memory and heavy tails, enhanced by multi-fractal geometries [121].
Heavy tailed distributions refer to distributions whose "tail" is heavier compared to an exponential distribution. These cases are characterized by relatively many high valued outliers and are categorized in fat tailed, long tailed and sub exponential distribution [157]. Cauchy, log normal, Pareto, Zipf and Students t-distributions exhibit heavy tails.

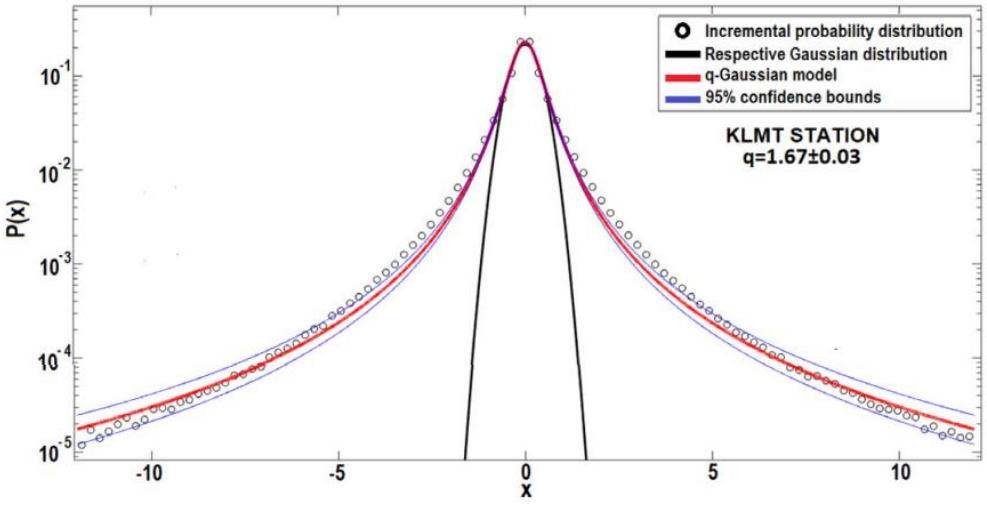

Figure 4.3 Example of fat tailed distribution risen from the probability density function of the normalized increments, of seismic ambient noise. Data obtained from the Medicane (Mediterranean hurricane) occurred on 28/09/2018 at KLMT station. [153].

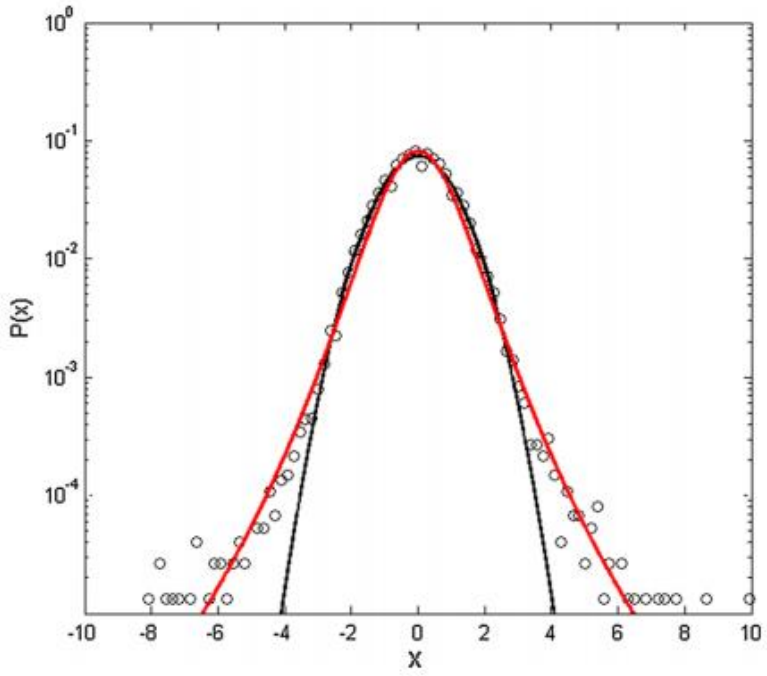

Figure 4.4 Fat tailed probability density function of ambient seismic noise for normalized increments. PDF has been implemented for a 10-minute duration of seismic record [97].

The statistical mechanics description of such systems can be achieved by a generalized framework proposed by Tsallis, known as non-extensive statistical mechanics (NESM) [96].

The main advantage of NESM is that it takes into account all scale correlation between the elements of a system. To quantify the nonextensivity, the concept of entropy is used to infer the least biased distribution via the concept of maximum entropy principle [158].

Central to NESM is the non-additive entropy Sq. For discrete cases. Sq is given by the equation:

$$S_q = k\frac{1-\sum_{i=1}^{W} p_i^q}{q-1} \qquad (4.40)$$

where q∈ R).

Here, k represents a positive constant assumed to be the Boltzmann's constant, W represents the number of microscopic configurations and q the entropic index.

Taking into account the entropy:

$$S_q = kln_q(\frac{1}{p_i}) \tag{4.41}$$

and the q-logarithmic as presented in (4.37):

$$y^{-1}(x) = \frac{x^{1-q} - 1}{1-q} \equiv ln_q x, \qquad x > 0, \qquad q \in R \tag{4.42}$$

we get the form of:

$$ln_q p_i = \frac{p_i^{1-q} - 1}{1-q} \Leftrightarrow ln_q(1/p_i) = \frac{\left(\frac{1}{p_i}\right)^{1-q} - 1}{1-q} = \frac{\left(\frac{1}{p_i^{1-q}} - 1\right)}{1-q} = \frac{\left(\frac{1 - p_i^{1-q}}{p_i^{1-q}}\right)}{1-q} \tag{4.43}$$

and finally, [147] get:

$$ln_q(1/p_i) = \frac{1 - p_i^{1-q}}{(1-q)p_i^{1-q}} \tag{4.44}$$

We now replace the equation (4.44) in (4.41) and impose the normalization constraint of:

$$\sum_{i=1}^{W} p_i = 1 \tag{4.45}$$

In order to retrieve the equation:

$$S_q = k(ln_q(1/p_i) \tag{4.46}$$

$$= k\sum_{i=1}^{W} \frac{ln_q\left(\frac{1}{p_i}\right)}{p_i}$$

$$= k\sum_{i=1}^{W} \frac{1}{p_i}\left(\frac{1-p_i^{1-q}}{(1-q)p_i^{1-q}}\right)$$

$$= k\sum_{i=1}^{W} \left(\frac{1-p_i^{1-q}}{(1-q)p_i^{-q}}\right)$$

$$= k\left(\frac{1}{1-q}\right)\sum_{i=1}^{W} \frac{1-p_i^{1-q}}{p_i^{-q}}$$

$$= k\left(\frac{1}{1-q}\right)\sum_{i=1}^{W} p_i^q\left(1-p_i^{1-q}\right) = k\left(\frac{1}{1-q}\right)\sum_{i=1}^{W}(p_i^q - p_i)$$

$$= k\left(\frac{1}{1-q}\right)\left(\sum_{i=1}^{W} p_i^q - \sum_{i=1}^{W} p_i\right) = k\left(\frac{1}{1-q}\right)\left(\sum_{i=1}^{W} p_i^q - 1\right)$$

As a result, the relation (4.41) is equivalent to the Tsallis entropy [147] [96] , as presented in the equation below:

$$S_q = k\frac{1-\sum_{i=1}^{W} p_i^q}{q-1} \tag{4.47}$$

For continuous variables, the Sq is given via the equation:

$$S_q[p] = k\frac{1}{q-1}(1-\int p(x)^q dx) \tag{4.48}$$

This form is considered as the generalized framework of the classical Boltzmann-Gibbs entropy of statistical mechanics, as it converges to ordinary S_{BG} in the case of ($\lim_{q\to 1}$). This association is understandable if we think about the limit of q as it approaches the value one in (4.47). Then we have:

$$\lim_{q\to 1} S_q = \lim_{q\to 1} k\frac{1-\sum_{i=1}^{W} p_i^q}{q-1} = \mathrm{k}\lim_{q\to 1}\frac{1-\sum_{i=1}^{W} p_i^q}{q-1} = k\ \lim_{q\to 1}\frac{1-\sum_{i=1}^{W} p_i p_i^{q-1}}{q-1} \qquad (4.49)$$
$$= k\ \lim_{q\to 1}\frac{1-\sum_{i=1}^{W} p_i\, e^{(q-1)lnp_i}}{q-1}$$

Furthermore, by implementing Taylor series expansion for $e^{(q-1)lnp_i}$ we [147] get:

$$e^{(q-1)lnp_i} = \sum_{n=0}^{\infty}\frac{(q-1)^n \ln^n p_i}{n!} \qquad (4.50)$$

If we assign n = 0 we get:

$$e^{(q-1)lnp_i} = \frac{(q-1)^0 \ln^0 p_i}{0!} + \frac{(q-1)^1 \ln^1 p_i}{1!} + 0\left(ln^n p_i\right) \qquad (4.51)$$
$$= \sum_{n=0}^{\infty}\binom{q-1}{n}\left(p_i-1\right)^n$$

$$\left.\begin{aligned} &\sum_{n=0}^{\infty}\binom{q-1}{n}\left(p_i-1\right)^n \\ &e^{(q-1)lnp_i} \approx 1+(q-1)lnp_i \end{aligned}\right\} \qquad (4.52)$$
$$= \lim_{q\to 1} S_q \approx k\lim_{q\to 1}\frac{1-\sum_{i=1}^{W} p_i[1+(q-1)lnp_i]}{q-1}$$
$$= k\lim_{q\to 1}\frac{1-\sum_{i=1}^{W} p_i + \sum_{i=1}^{W}(q-1)p_i lnp_i}{q-1}$$
$$= k\lim_{q\to 1}\frac{(q-1)\sum_{i=1}^{W} p_i lnp_i}{q-1} =$$
$$= k\lim_{q\to 1}\sum_{i=1}^{W} p_i lnp_i = k\sum_{i=1}^{W} p_i lnp_i = k\frac{S_{BG}}{k_B}$$

From the above, it is clear that the generalized form of Tsallis entropy is equivalent to the Boltzmann-Gibbs entropy in the case of lim $_{q\to 1}$ and k = k_B.

There are three potential cases for the entropic index q. The first is recovered when q<1 and is called super-additivity. The second case emerges when q=1 and is actually the limit of the q index as it approaches the value 1 (lim $_{q\to1}$) and is called additivity. This case retrieves the Boltzmann-Gibbs entropy. The third one arises in the case of q>1 and corresponds to sub-additivity. Despite the fact that the Tsallis entropy shares the majority of properties with the entropy of Boltzmann-Gibbs, the Tsallis q entropy is non-additive [96] [159], while the S_{BG} is additive:

$$S_{BG} = (A + B) = S_{BG}(A) + S_{BG}(B) \tag{4.53}$$

This behavior introduces the non-additivity concept for the NESM theory. The main difference between S_{BG} and S_q entropy is generated by the concept that instead of summing the entropy of the two probabilistically independent subsystems, A and b, to obtain the total entropy of the main system (A, B), the non-additive entropy approaches the main system entropy via the formula of:

$$\frac{S_q(A+B)}{k} = \frac{S_q(A)}{k} + \frac{S_q(B)}{k} + (1-q)\frac{S_q(A)}{k}\frac{S_q(B)}{k} \tag{4.54}$$

This concept, was first incorporated by Tsallis in 1998 [96], influenced by multifractality physics, and describes that the generalized framework of BG statistical mechanics initiates bias in probabilities.
Taking into account the maximization of S_q under the conditions of (4.55) and (4.56):

$$\int p(x)dx = 1 \tag{4.55}$$

and

$$\int p_q(x)U(x)dx = U_q \tag{4.56}$$

The p_q is given by the formula:

$$p_q(x) = \frac{p_q(x)}{\int p_q(x)dx} \tag{4.57}$$

and represents the escort probability [159], U(x) is the function that describes the system under examination and U_q is referred as the q-average.
The escort distribution is a simple parameter deformation of the original distribution that emerges consequently from the maximum entropy theory, between the distribution under examination and the uniform distribution [160].
For complex systems, a custom long tailed probability distribution is critical and mandatory. The essential role of a custom-made PDF is assigned into a generalized or into a sequence of escort distributions, as they are considered more useful due to the fact that they meet the conditions of the respective statistical analysis and are effectively implemented into complex and anomalous statistical physics [161].
The escort distribution procedure can also be considered as a fundamental approach of giving suitable weight for individual fat tailed constituents.
The mentioned approach is assigned to the multi-fractal attributes of nonlinear dynamic systems [162].
In the case of a parabolic function, the U(x) is given by (4.58)

$$U(x) = x^2 \tag{4.58}$$

In the case of (4.58) the U_q, as presented in (4.56), behaves as a fluctuation intensity index. Implementing the Lagrange Multipliers method to equation (4.48), we obtain the probability distribution function and under the constraints of (4.55) and (4.56) we derive the relation [146] of (4.59):

$$p(x) = \frac{1}{Z_q(B)}[1 + B(q-1)U(x)]^{-\frac{1}{q-1}}, \quad q > 1 \tag{4.59}$$

where Z_q

$$Z_q(B) = [B(q-1)]^{-\frac{1}{2}} \frac{\Gamma\left(\frac{1}{2}\right)\Gamma\left(\frac{1}{q-1}, \frac{1}{2}\right)}{\Gamma\left(\frac{1}{q-1}\right)} \tag{4.60}$$

The formulation of (4.60) is characterized as a generalized q-partition function, with Γ a gamma function. The above is considered as a generalized canonical distribution under the frame of Tsallis statistics. For (4.58) the distribution becomes:

$$p(x) = \frac{1}{Z_q(B)}[1 + B(q-1)q^2]^{-\frac{1}{q-1}} \qquad (4.61)$$

This formulation is the so-called q-Gaussian distribution and it converges into a normal Gaussian distribution in the specific case of ($\lim_{q\to 1}$).
The comparison of probability density functions, between Gaussian and q-Gaussian distributions, is given in Figure 4.5.

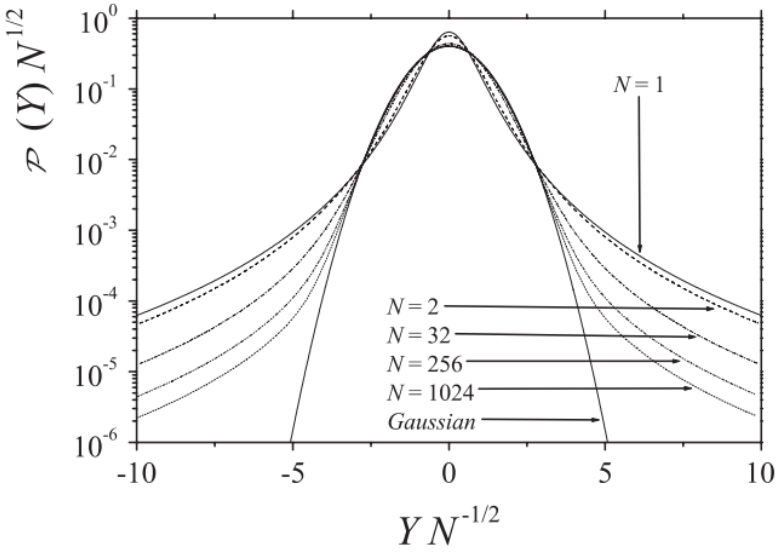

Figure 4.5 Probability density function, P(Y), versus Y in a logarithmic linear scale. In this diagram the y-axis represents the sum (N) of a given independent variable X, having a q-Gaussian distribution behavior. As the N lim$_{\to\infty}$, P(Y) inherently approaches the form of a Gaussian distribution [159].

The illustration for different values of q index, and the conversion to a Gaussian like distribution when the limit of q tends to 1, is given in Figure 4.6. It is clear that as the q index increasing, the outliers are also increasing, exhibiting fat tail distributions.

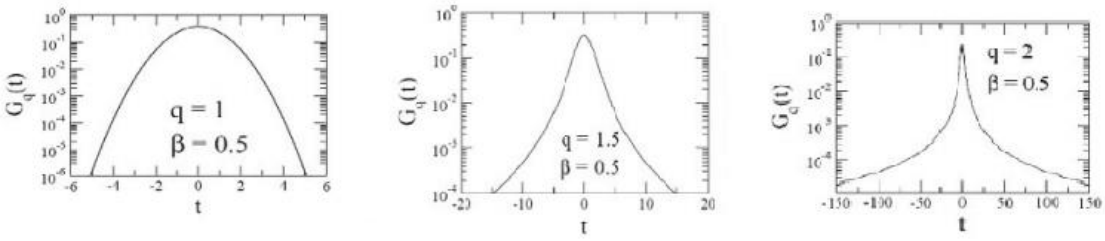

Figure 4.6 q-Gaussians in logarithmic linear scale for cases of q=1, q=3/2 and q=2, respectively [159]. As the q index increases, the fat tails are becoming dominant (memory effect).

5 SeisComplex

5.1 Introduction to SeisComplex Software and its applications.

In recent years, the development of technology has brought a tremendous breakthrough in computational power and in the way of data acquisition and processing, in all scientific disciplines.
The concept of entropy through the theory of non-extensive statistical physics, as proposed by Tsallis in 1988 (see 4.3 for more details), has recently become a fast-growing topic in Earth Science disciplines.
In an effort to bridge the gap between statistical mechanics and its application upon geosciences, we developed the 'SeisComplex V.1.0' software. SCP V.1.0 provides both automatic as well as manual procedures and allows users to collect and set the desired structure of any available geophysical data, such as seismic waveforms, GPS time series, triaxial tests, etc. (for the online mode, data must be officially provided by a data acquisition server).
For data processing, the signal analysis and the non-extensive statistical physics tools are provided to the user.
The results are compatible with a variety of external and/or third-party programs, as they are available in binary and ascii structures.

5.2 Seismological implementation.

The dominant characteristic of the software is the simplicity and the integrated automatizations, both in data acquisition as well as in data processing.
A schematic representation of SeisComplex and its plugins, is configured below.

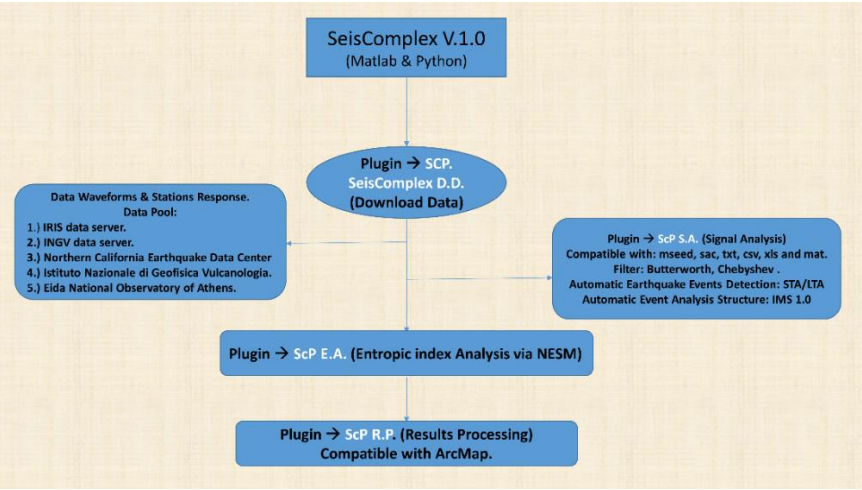

Figure 5.1 Flow chart of the SeisComplex software (06/2020).

The user can automatically login and retrieve seismological time series (seismic waveforms and response files) via the SeisComplex (ScP) Download data plugin (Figure 5.2), from a variety of data acquisition servers, as listed below:

1. IRIS data server.
2. INGV data server.
3. Northern California Earthquake data server.
4. Istituto Nazionale di Geofisica Vulcanologia data server.
5. Eida - National Observatory of Athens.

External sources can also be available to users, by the modification of the initialization source file. Furthermore, waveforms via response files can be additionally processed through the Deconvolution graphical user interface, by setting the mandatory parameters of the inventories, the water level of deconvolution, the frequency domain bandpass filter, the zero mean and cosine taper (the three last processes take place before the deconvolution procedure), as presented in Figure 5.3.

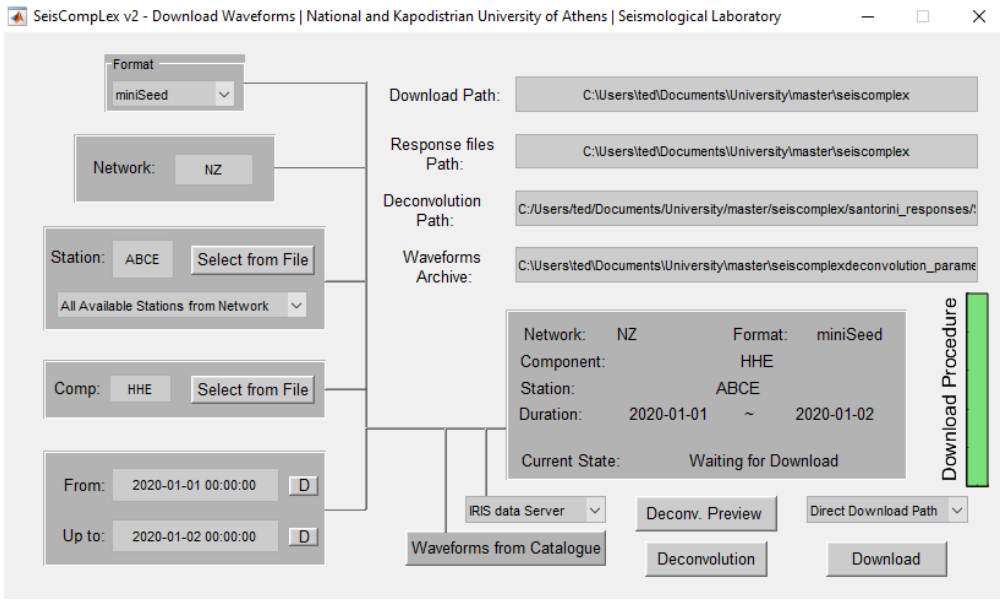

Figure 5.2 The graphical user interface of the ScP. Download Data plugin.

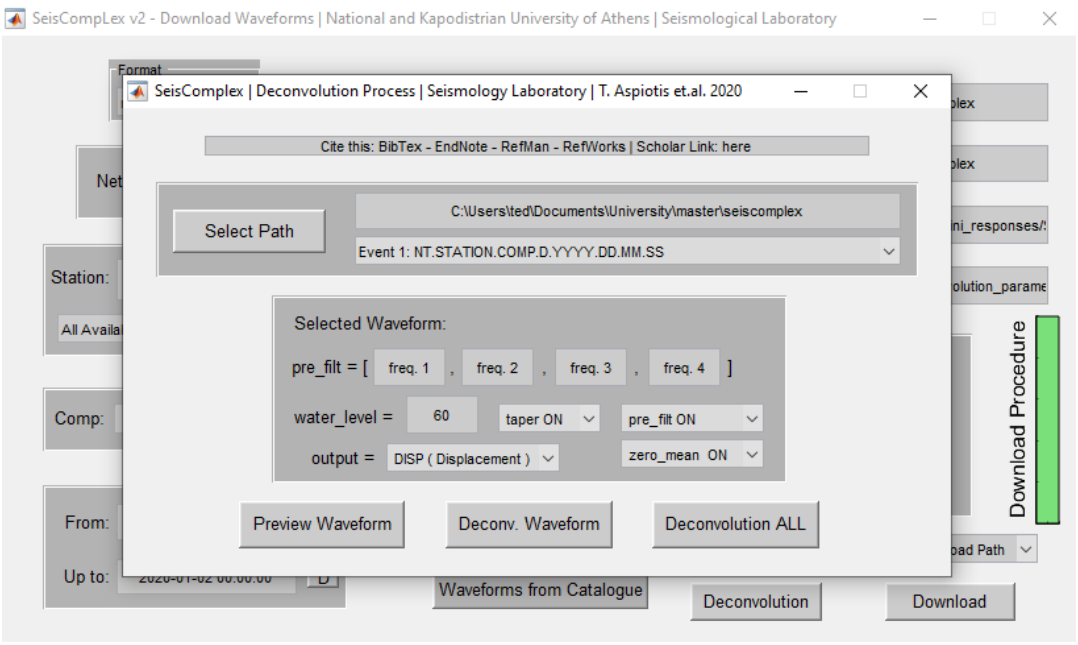

Figure 5.3 The deconvolution process graphical user interface for seismic waveforms.

5.2.1 Signal Analysis

Prior to the statistical analysis, the tool of Signal Analysis (S.A.) provides a variety of processing procedures.

The plugin can import seismic catalogues as well as hypocenter solutions under IMS 1.0 structure (one or multiple events separated by flag). For raw data without pre-processing, the automatic procedure can generate the onsets of P and S body waves, by applying a combination of STA/LTA, STFT and Aki statistics (weighted solutions) methodology. In both cases, individual waveforms can be separated per component and per earthquake event with the utility of the 'cut2mseed' function-button, a procedure based on Matlab & Python. The 'MakeEvents' function-button generates a seismic list.

The S.A. plugin is compatible with mseed, sac and ascii formats. The data structure can be as simple as two columns with extensions txt, xls, csv or dat. The filtering of time series can be executed, either by implementing Butterworth or Chebyshev filters with the options of highpass, lowpass, bandpass and bandstop configuration, at any given filter order.

The order of filter is a crucial parameter, as it can enhance or eliminate ringing artifacts and Gibb's effect, an inherent phenomenon in cases of finite series truncation.

In the example presented in Figure 5.4, we design a first and a fourth order lowpass Butterworth filter, upon a synthetic signal, with a characteristic cutoff frequency of 0.084 Hz, normalized to the signal Nyquist frequency. In comparison with the fourth ordered lowpass filter with the abrupt cutoff transition, but rippling before and after the

cutoff frequency, the low ordered filter, depicts a larger transition zone within the cutoff frequency, without showing any signs of Gibb's effect.

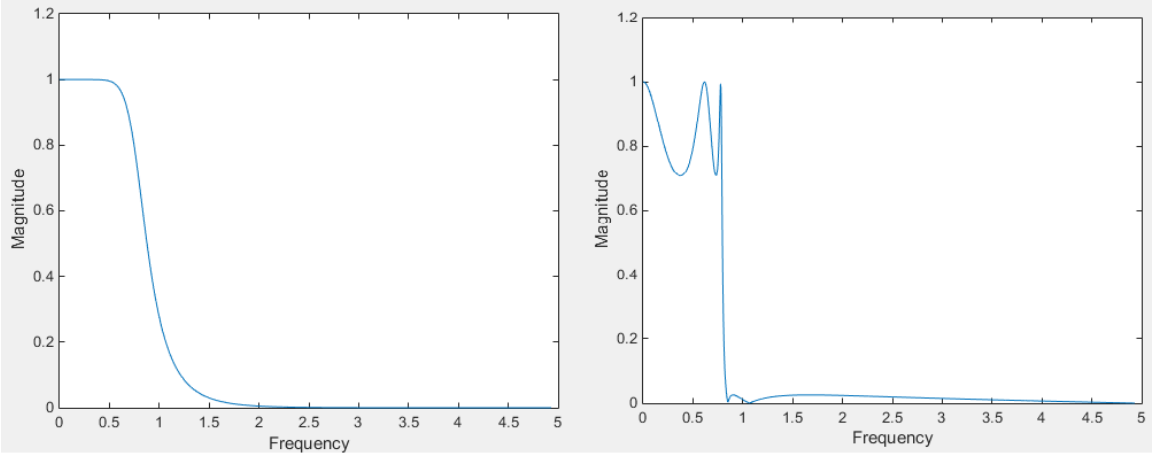

Figure 5.4 Transition from passband to stopband for first (left) and forth (right) order Butterworth filter.

SeisComplex provides a zero-phase forward and reverse digital filtering. With this technique, the filter magnitude is unaffected by the reversed direction, due to the fact that it will always be restricted to 0 or 100% of the initial amplitude, depending on the frequency.

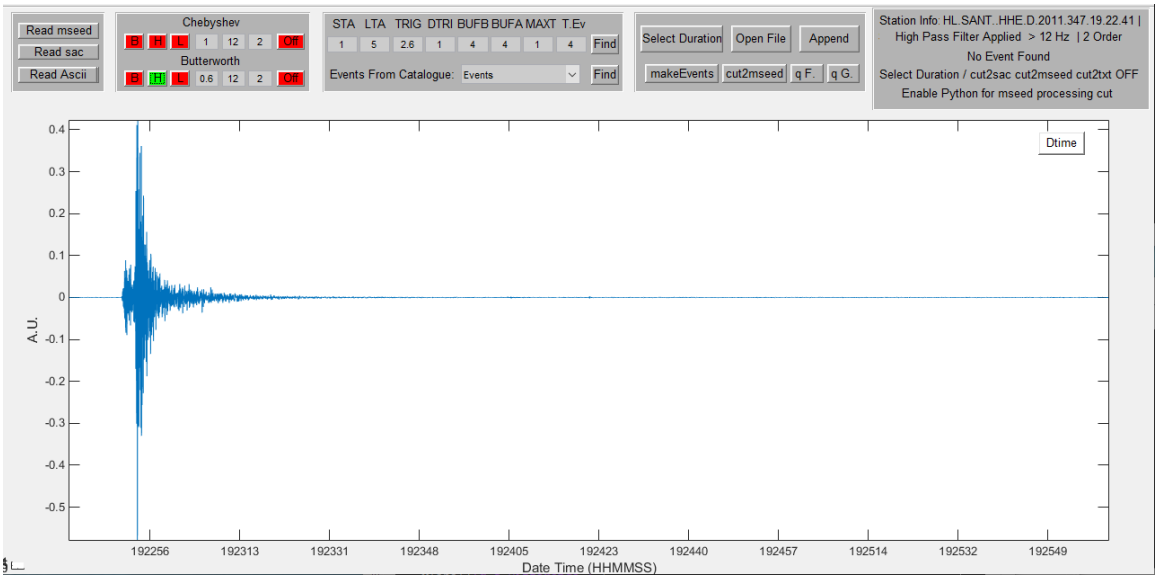

Figure 5.5 The graphical user interface of the ScP. S.A. plugin (Signal Analysis).

After the implementation of the proper filter, the vectorized approach of STA/LTA procedure can provide an instant estimation of the potential existence of Earthquakes events. After extensive testing of the parameters (as given in Table 1.1) the method can distinguish micro-events with time buffer up to 4 seconds.

Input function parameters	Assigned variable details
SIGNAL	Vector of raw or filtered signal (component)
SAMRA	Sampling rate
TDIF	Sampling interval (time domain)
STA	Short time average window
LTA	Long time average window
ENGA	Engaging the triggering process
DISE	Disengaging the triggering
TIME_LAPSE_1	Time before triggering
TIME_LAPSE_2	Time after triggering
TIMEA	Duration threshold of potential event

Table 5.1 The multi-parameter assignment of STA/LTA procedure.

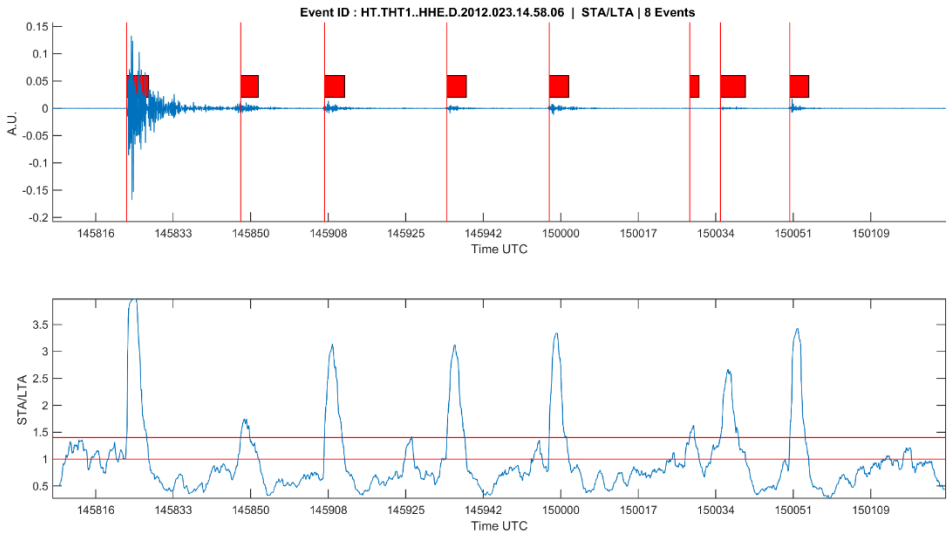

Figure 5.6 Automatic determination of earthquake event and micro-events after the implementation of the SeisComplex STA/LTA procedure. Station THT1, E-W Component, date 2012023145806 (YYYYJJJHHMMSS).

5.2.2 Coda Determination

The signal to Noise Ratio is widely used as an indicator of a general approximation for the coda wave duration. In the framework of this dissertation and in order to dump out earthquake events with “hidden” frequencies or local overlapping micro-events, as well as volcanic tremors, spasmodic bursts and low frequency events, along with the effort not to minimize the site amplification signatures (scattering effects) in all the recorded seismic waveforms throughout the unrest period of Santorini’s Volcano, a five-step procedure was implemented.
Standardization directives of coda wave determination include the signal to noise ratio (SNR), the short time average over long time average (STA/LTA) in time domain waveforms (Figure 5.6), the novel STA/LTA procedure implemented upon Hilbert transformation signal, the short time Fourier transform (frequency domain) in order to reveal unwanted ‘’hidden’’ micro-events within codas and finally, a manual verification and/or re-estimation step, as shown in Figure 5.7.

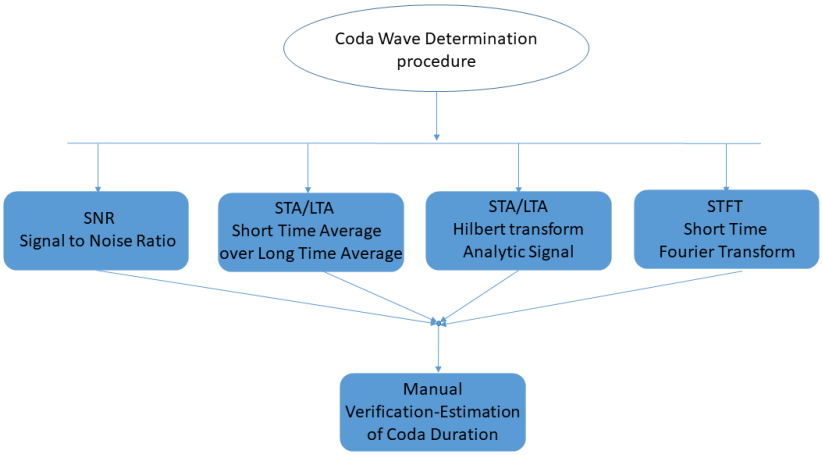

Figure 5.7 Coda wave duration determination procedure (flow chart of SeisComplex software).

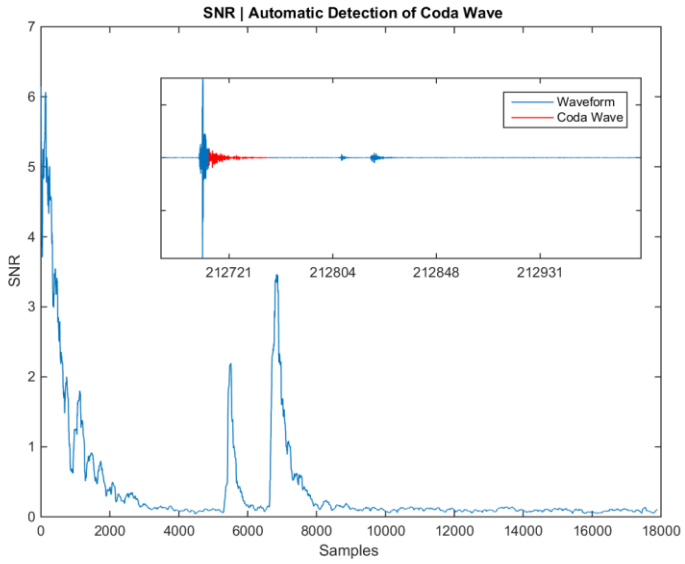

Figure 5.8 The Signal to Noise Ratio (SNR) process as a part of the five-step coda wave length determination.

The exponential attenuation of the signal to noise ratio, as seen in Figure 5.9, can give valuable information about the intrinsic absorption and the scattering attenuation factor of the medium and the propagation path (following the ray tracing), leading to the Q quality factor.

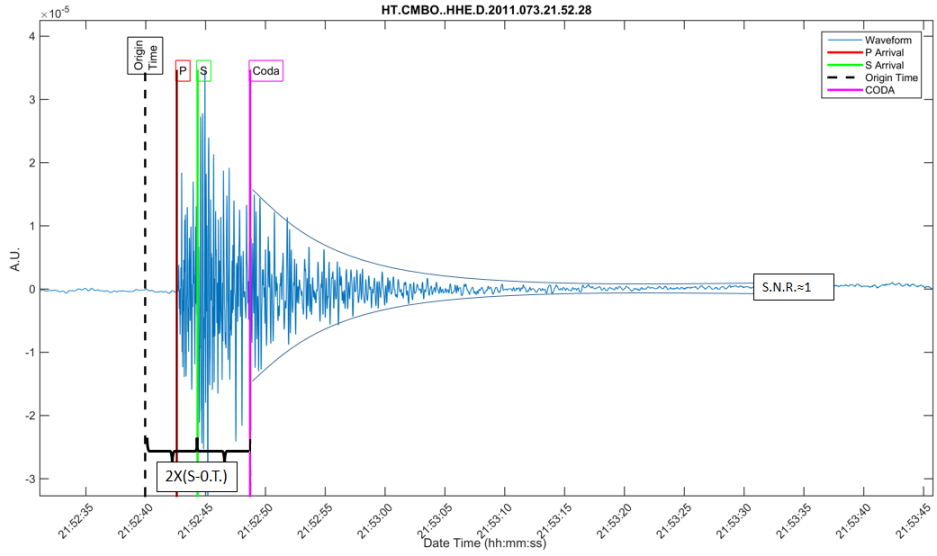

Figure 5.9 Determination of coda waves. Station CMBO, Comp. HHE, (14 March 2011).

Our novel procedure of coda wave length-duration determination, includes the STA/LTA like method, implemented upon the deconvolved time domain waveforms. In order to enhance the micro-event detection analysis, the computation of the cross product between the real and the imaginary part of the Hilbert transformed signal was performed, as shown in Figure 5.10 and Figure 5.11.

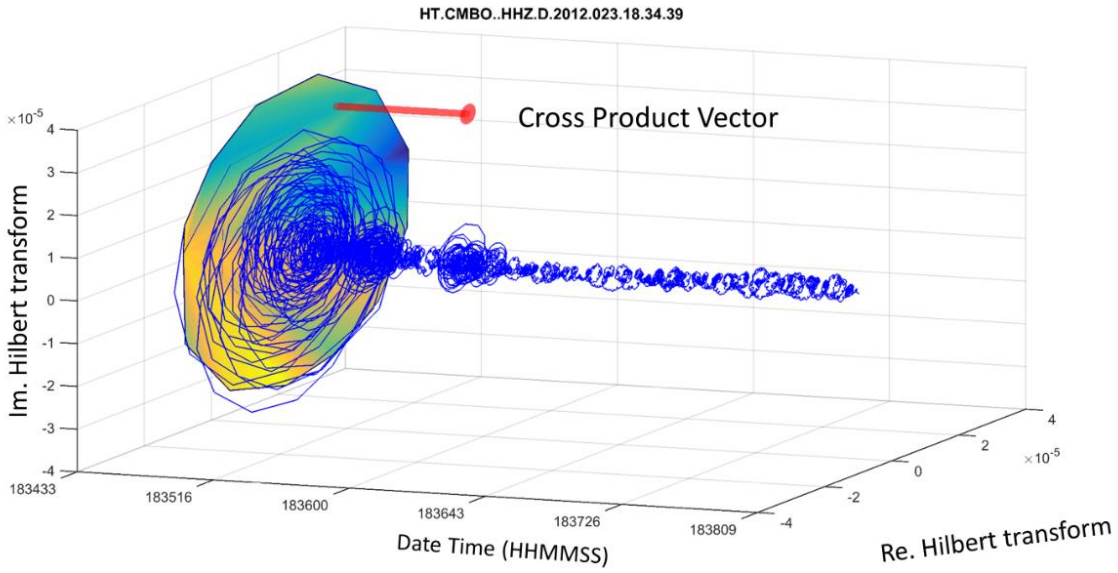

Figure 5.10 The helical wavefunction after implementing Hilbert transformation. The 2D surface (colored surface and red arrow) represents the cross product between the real and the imaginary part of the seismic Hilbert transformed waveform.

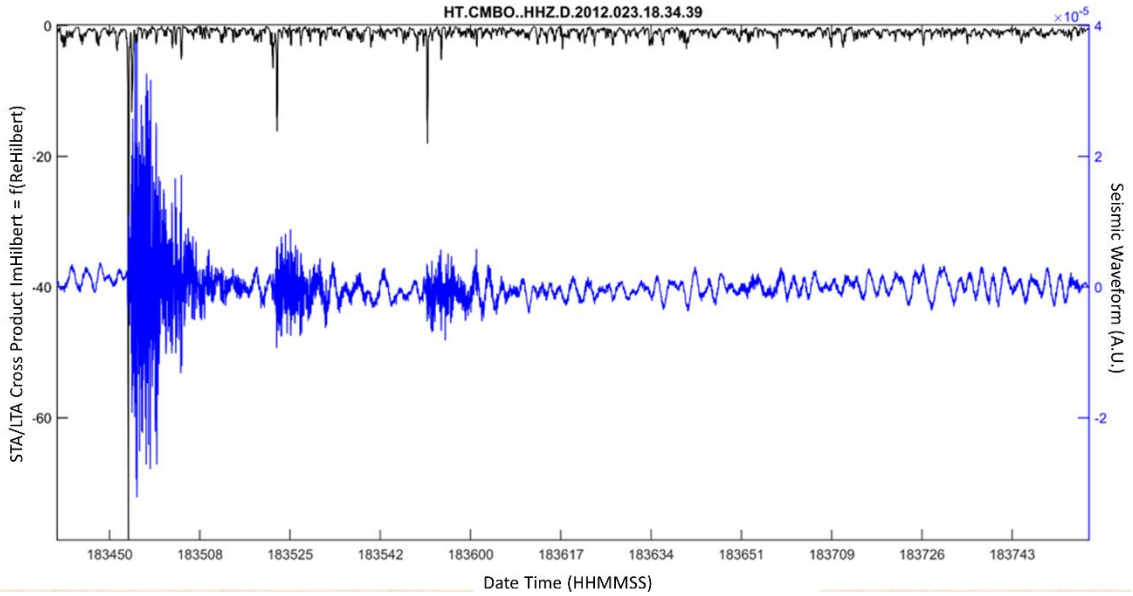

Figure 5.11 Presentation of the STA/LTA procedure, based on the cross product vector of the helical wavefunction, as presented in Figure 5.10.

The Hilbert transformation formula is given by the relations (5.1) and (5.2) [163]:

$$H(u)(t) = \frac{1}{\pi}\int_{-\infty}^{\infty} \frac{u(\tau)}{t-\tau} d\tau \qquad (5.1)$$

where the H(u)(t) represents the time domain signal. The inverse is given by the equation (5.3) [163]:

$$g(y) = H[f(x)] = \frac{1}{\pi} PV \int_{-\infty}^{\infty} \frac{f(x)dx}{x-y} \qquad (5.2)$$

$$f(x) = H^{-1}[g(y)] = -\frac{1}{\pi} PV \int_{-\infty}^{\infty} \frac{g(y)dy}{y-x} \qquad (5.3)$$

where PV represents the Cauchy value, known as the principal value integral (Henrici 1988) and is given in equation (5.4):

$$PV \int_a^b f(x)dx = \lim_{\varepsilon \to 0^+} \left[\int_a^{c-\varepsilon} f(x)dx + \int_{c+\varepsilon}^b f(x)dx \right] \qquad (5.4)$$

Our enhanced automatic detector is taking into account the vectors of ex.1 and ex.2 as shown below and computes the cross product as given in (5.5).

- ImHilbert = [IHz, IHz+1, IHz+2] ex.1
- TDomain = [TDz, TDz+1, TDz+2] ex.2

$$ImHilbert \times TDomain = \begin{vmatrix} i & j & k \\ IH_z & IH_{z+1} & IH_{z+2} \\ TD_z & TD_{z+1} & TD_{z+2} \end{vmatrix} = \begin{vmatrix} IH_{z+1} & IH_{z+2} \\ TD_{z+1} & TD_{z+2} \end{vmatrix} i - \begin{vmatrix} IH_z & IH_{z+2} \\ TD_z & TD_{z+2} \end{vmatrix} j + \begin{vmatrix} IH_z & IH_{z+1} \\ TD_z & TD_{z+1} \end{vmatrix} k \quad (5.5)$$

where ImHilbert represents the linear 3 samples moving window of the imaginary part wave vector and TDomain represents the 3 samples moving window of the real part wave vector, which in our case is the Hilbert's transformed signal of the time domain velocity.

Furthermore, to eliminate the probability of getting into account poor quality coda records, Fourier and Gabor transformation, a short time Fourier transform by using gaussian windowing as a window function, was applied, as presented in Figure 5.12.

$$G_x(t,f) = \int_{-\infty}^{\infty} x(\tau)\varphi(\tau - t)^{e^{j2\pi f\tau}} d\tau \quad (5.6)$$

where the ϕ(τ) is the Gabor analysis window and t represents the location of the window center. In this case the window is considered to be a Gaussian function. It is clear from (5.6) that the Gabor transform is a special case of short time Fourier transformation by implementing a Gaussian window. The selection of Gaussian window was chosen, due to its low leakage factor (0.01%) and low relative sidelobe attenuation (-44.1 dB).

In the cases of finite series x[i], the discrete Gabor transformation is given by the equation:

$$\boldsymbol{G_x(m,n) = \sum_{i}^{L-1} x[i]\gamma[i - m\Delta M]W_L^{-n\Delta N_i}} \quad (5.7)$$

where ΔM represents the time sampling interval and ΔN the frequency sampling interval. Finally, the variables M and N indicate the length of sampling in time and frequency domain, respectively [164].

$$\gamma[k] = e^{\pi k^2} \quad (5.8)$$

$$W_L^{\pi k^2} = e^{j\left(\frac{2\pi}{L}\right)^{ki}} \quad (5.9)$$

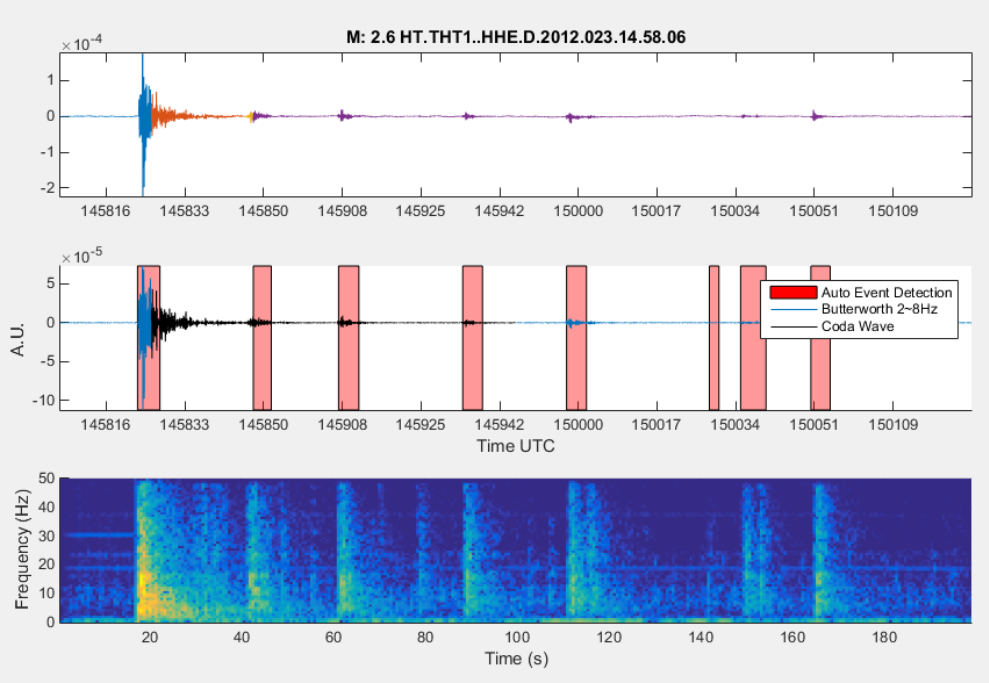

Figure 5.12 Seismic time domain waveform (up), STA/LTA process (middle) and implementation of Short Time Fourier Transform (down), as a part of the integrated coda determination procedure.

Last, all waveforms were manually checked for the final evaluation and/or re-estimation of 'coda duration', as a prerequisite quality procedure step.

5.2.3 q-Gaussian

The concept of the entropic index via the theory of NESM (paragraphs 4.3 and 4.4) has led many researchers, to investigate a variety of natural phenomena, from the micro-scale [165] up to the macro-scale of galaxies [166] [167]. In between, for planetary applications, the entropic index, under specific considerations and procedures (as presented in this dissertation), can be considered as a scattering entropic index.

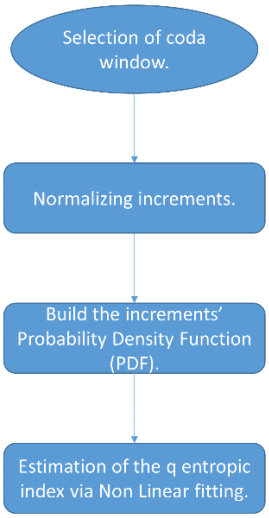

Figure 5.13 Flow chart of the entropic scattering index, qs, analysis procedure.

The q_s (scattering entropic index) can be processed and analyzed via the q-Gaussian plugin named 'Entropic Index Analysis', as shown in Figure 5.14.

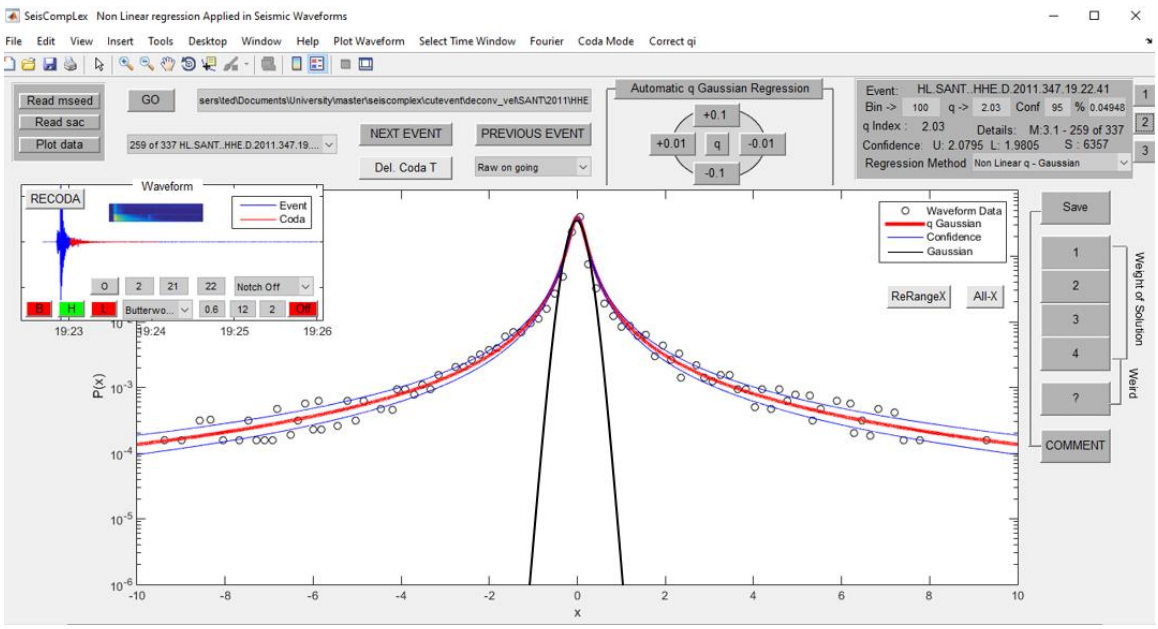

Figure 5.14 q-Gaussian procedure and its graphical user interface of the SeisComplex ScP S.A. plugin.

In order to obtain the q_s of codas, the differences of continuous ground velocity, acceleration or displacement samples, is configured. In case of velocity, we have:

$$X(t) = V(t+1) - V(t) \tag{5.10}$$

Then, the vector of X(t) is standardized as given below:

$$x = \frac{X - \langle \bar{X} \rangle}{\sigma_x} \tag{5.11}$$

where <X> represents the observed mean value and σ_x the standard deviation of X(t).
Furthermore, the entropic index for discrete series, as presented in (4.47):

$$S_q = k \frac{1 - \sum_{i=1}^{W} p_i^q}{q-1}$$

after the maximization, under the conditions of (4.55) and (4.56) and after applying the Lagrange multipliers method, in the case of U(x)=x2, led to the generalized q-Gaussian distribution, as presented in (4.59):

$$p(x) = \frac{1}{Z_q(B)} [1 + B(q-1)q^2]^{-\frac{1}{q-1}}$$

which is the mandatory probability density function (PDF).
If we assume that:

$$\frac{1}{Z_q(B)} = A1 \tag{5.12}$$

and

$$B = \frac{1}{b(2)}, q = b(1) \tag{5.13}$$

Then, the p(x) takes the form of (5.14):

$$P(x) = A1\left[1 + \frac{1}{b2}(q-1)x^2\right]^{-\frac{1}{b1-1}}$$

$$b(1) - 1 = -\Big(1 - \big(b(1)\big)\Big) \; and \; -\frac{1}{b(1)-1} = \frac{1}{1-b(1)}$$

$$P(x) = A1\left[1 - \frac{1}{b2}(1-b1)x^2\right]^{-\frac{1}{1-b1}} \qquad (5.14)$$

This formulation depicts the fat tailed q-Gaussian function, which is the nonlinear solution of the entropic index q_s, since seismic coda waves present long-term memory effects.

The q_s is a very sensitive index and it must be analyzed under restricted frequency examination. In the Figure (5.14), the frequency sensitivity becomes clear.

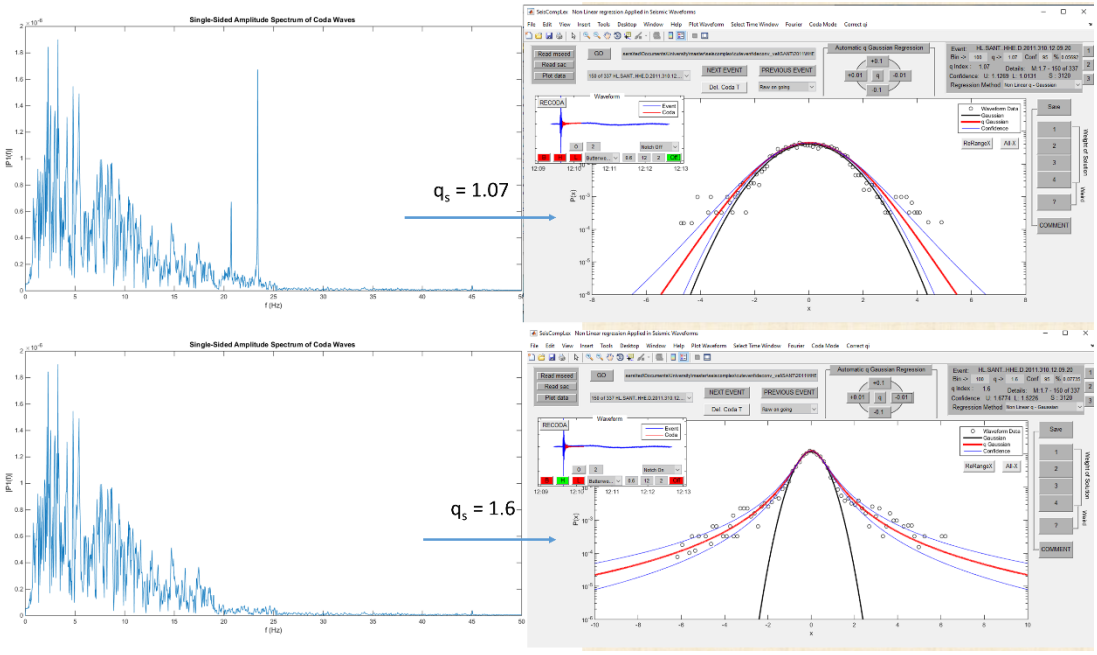

Figure 5.15 The q_s index before and after the implementation of two narrow notch filters. The nonlinear solution for coda increments ranges from 1.07 to 1.6.

A second and more robust procedure of cutting out unwanted and parasitic frequencies, can be achieved via the 'FilterOnDemand' function, by implementing inverse fast Fourier transform:

$$\breve{g}: R \rightarrow \mathrm{C}\,, \breve{g}(\omega) = \frac{1}{2\pi} \int_{-\infty}^{\infty} g(t) e^{i\omega t} dt \qquad (5.15)$$

5.3 Results processing

The abbreviation of ScP. R.P. (as given in Figure 5.1) represents the SeisComplex results processing tool. The main utility of R.P. tool, is the instantly manipulation of data, by applying a variety of spatio-temporal and seismic catalogue filters, as well as quality evaluation.
This tool is suitable for a variety of scientific data, as it can manipulate both ascii and binary protocol. As far, it has been extensively used with seismic catalogues data, seismic array data, GPS time series and triaxial material strength tests, analyzing the statistics of the microcracks occurrence. The structure of individual data is changeable, as it can be manipulated via a graphical user interface, setting specific forms of input.
The processing of the respective data, is carried out through a collection of Matlab functions, which for a large volume of data sets, can operate in parallel processing (parallel computing), depending on the computational power of each terminal. In addition, time consuming functions, such as those appearing in the application of transformations, can be handled by using the GPUArray method.
The graphical user interface of the result processing plugin, is given in Figure 5.16. All results, are compatible with G.I.S. ArcMap for further analysis.

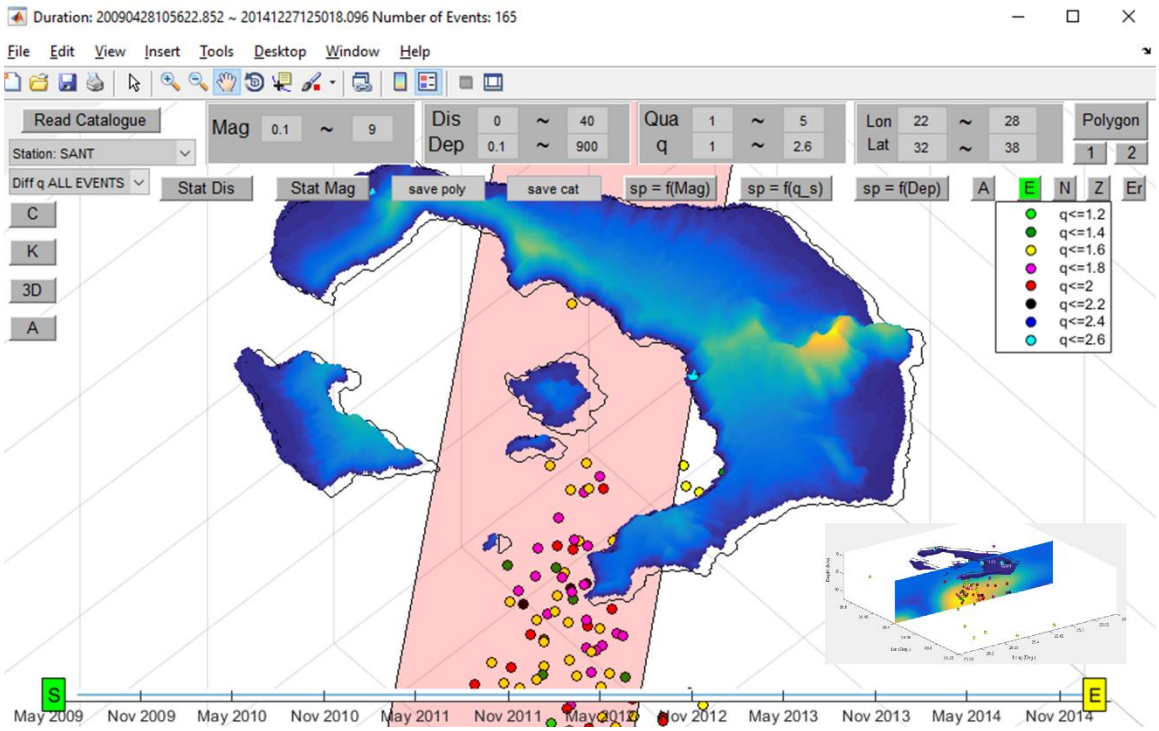

Figure 5.16 The graphical user interface of ScP R.P. (result processing) plugin.

6 Data selection

6.1 Seismological stations and seismic events.

The data that were used for the purposes of this dissertation had been downloaded via the SeisComplex D.D. plugin using the EIDA data center of the National Observatory of Athens (http://eida.gein.noa.gr/). The response files were obtained by EIDA node and Geofon gfz Potsdam data center.

NETWORK	STATION	COMPONENT	Selected Duration
GE, HL	SANT	HHE	2009 - 2014
		HHN	
		HHZ	
HT	CMBO	HHE	2011 - 2014
		HHN	
		HHZ	
HT	THT1	HHE	2011 - 2014
		HHN	
		HHZ	
HA	SNT1	HHE	2012 - 2014
		HHN	
		HHZ	
HA	SNT2	HHE	2012 - 2014
		HHN	
		HHZ	
HA	SNT3	HHE	2012 - 2014
		HHN	
		HHZ	
HA	SNT5	HHE	2014
		HHN	
		HHZ	

Table 6.1 The seismic database of SANT, CMBO, SNT1, SNT2, SNT3, SNT5 and THT1 stations.

The selection of the SANT, CMBO and THT1 seismological stations to obtain the final results was based upon the data availability during the volcanic unrest period. SANT station was the only local station in operation, before during and after the Santorini's unrest period of 2011-2012. CMBO and THT1 have recorded many events during the intense seismicity period, in comparison with SNT1, SNT2, SNT3 and SNT5. The azimuthal distribution was also a mandatory criterion of selection, in order to

investigate the scattering procedures within the caldera's volume. As a result, SNT_x stations due to the lack of the necessary amount of earthquake events, were excluded from results.

Seismic networks of Table 6.1, correspond to the Hellenic Seismic Network, HL, doi:10.7914/SN/HL, the Seismological Network of Aristotle University of Thessaloniki, HT, doi:10.7914/SN/HT, the Seismological Network of University of Patras, HP, doi:10.7914/SN/HP, and the Seismological Network of National and Kapodistrian University of Athens HA, doi:10.7914/SN/HA.

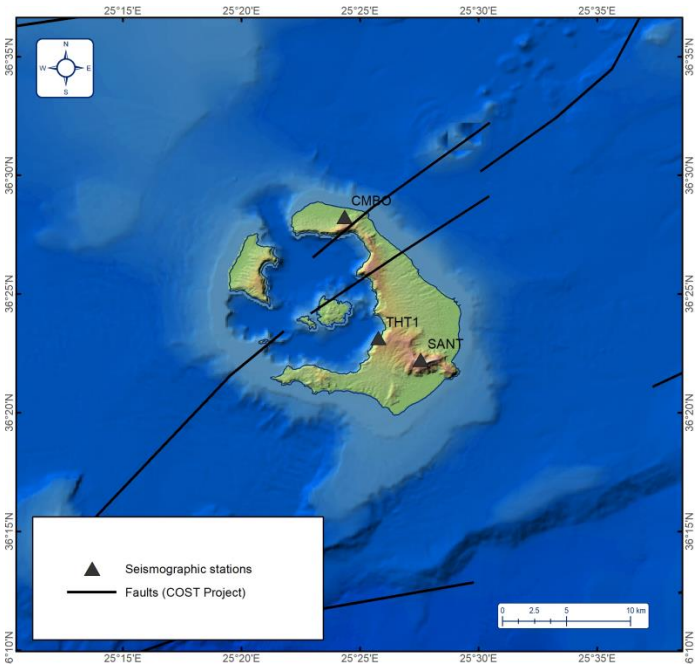

Figure 6.1 Spatial and azimuthal distribution of the three selected seismic stations and the main seismotectonic features of the wider area.

The official seismic catalogue of the National observatory of Athens, Geodynamic Institute [168] consists of 908 seismic events for the period from 2009 to 2014, as seen in Figure 6.2 and Figure 6.3.

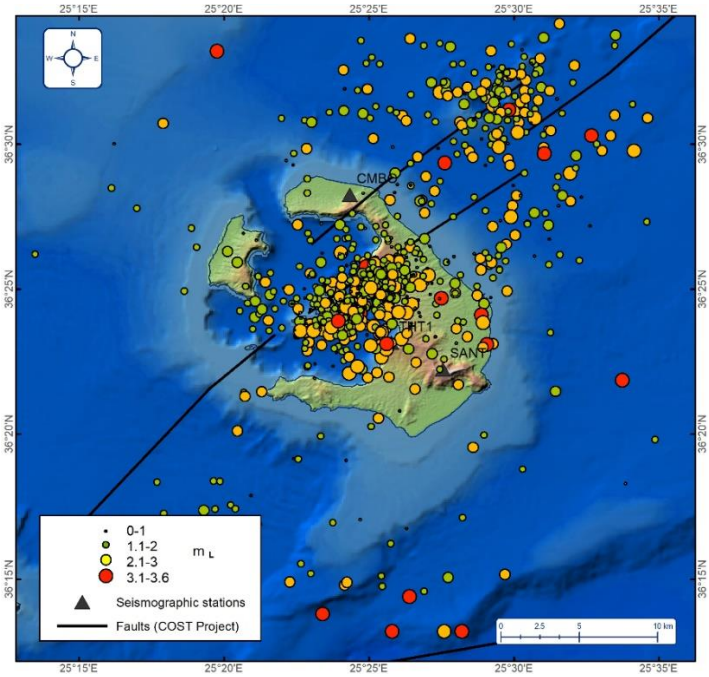

Figure 6.2 Seismicity of Santorini's wider area from 2009 to 2014 (GEIN-NOA).

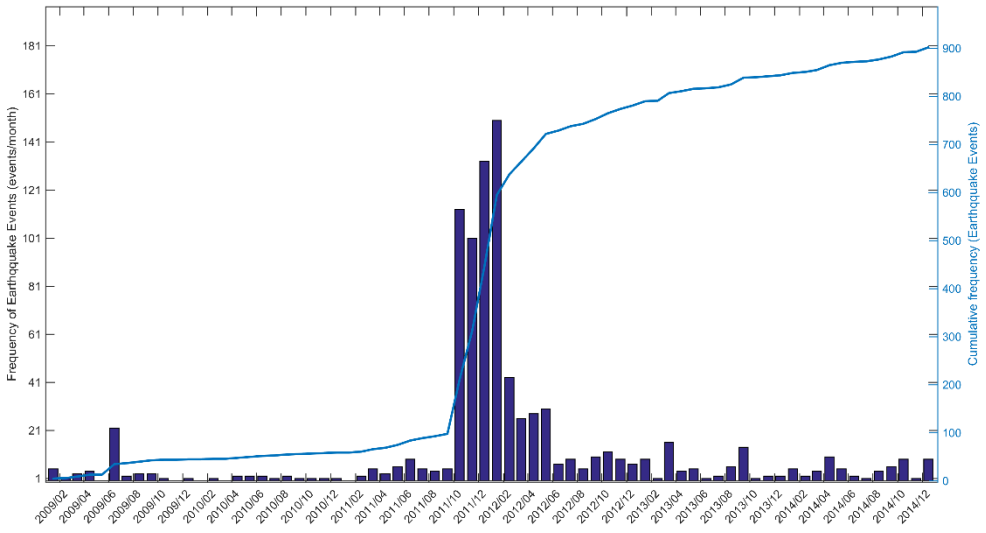

Figure 6.3 Statistical overview of the NOA, Geodynamic institute seismic catalogue.

6.2 Data processing

All seismic waveforms were transformed from counts into velocity [169].

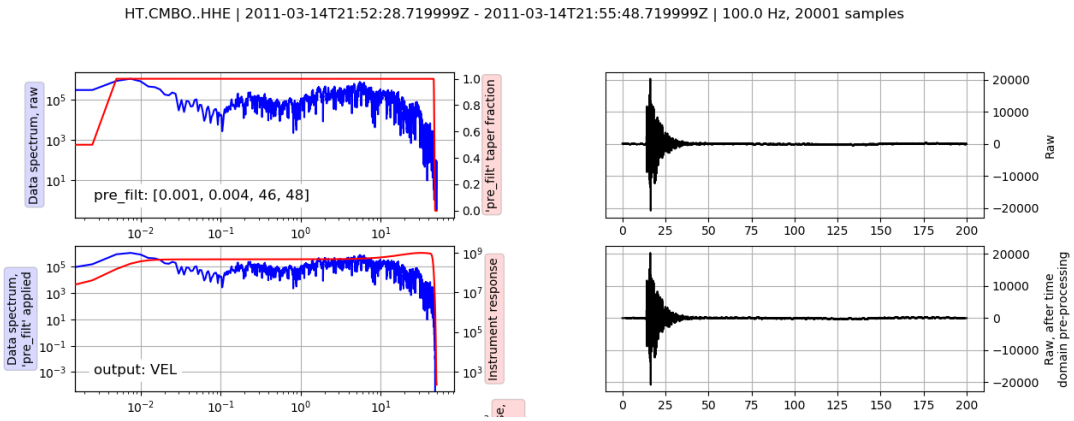

Figure 6.4 Data spectrum, taper fraction of raw data and the relative seismic waveform (up line). Instrument response, data spectrum under the implementation of a given filter and the relative time domain waveform.

To eliminate signal artifacts, all filtering processes were conducted upon detrended and cosine tapered signals, with a buffer of 100 samples/sec, since all instruments hold a sampling rate of 100, before and after the coda wave duration.
A high pass filter of 0.6 Hz was applied upon all deconvolved waveforms to eliminate unwanted long periods.
Different values of water level and the outcome in a deconvolved waveform is given in Figure 6.5.
The meaning of the water level is to produce an acceptable noise level for the associated receiver function. The threshold of water level can play the important role of a filter, since it sets the amplitude spectrum level, in which specific frequencies can vanish.

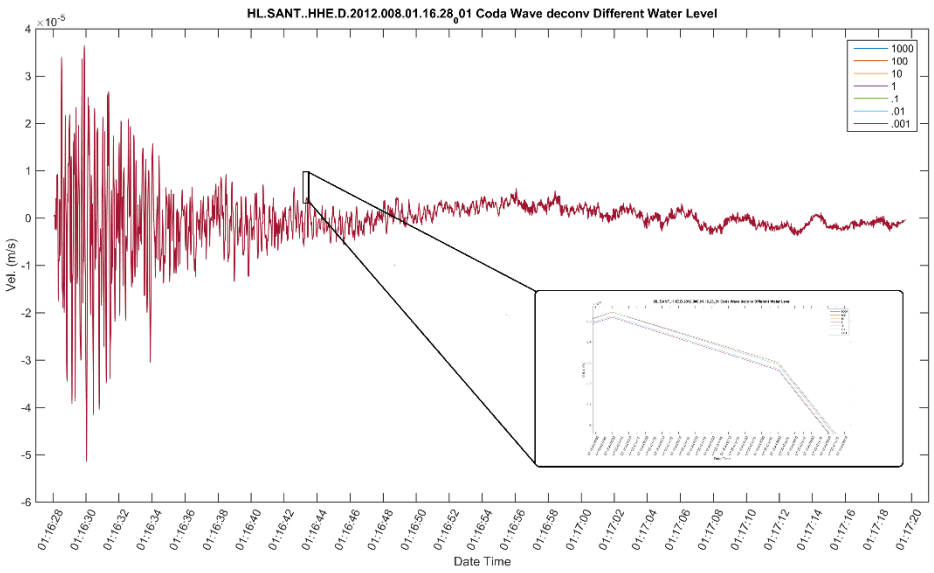

Figure 6.5 Deconvolution process upon coda waves for different values of water level, ranging from 0.001 to 1000.

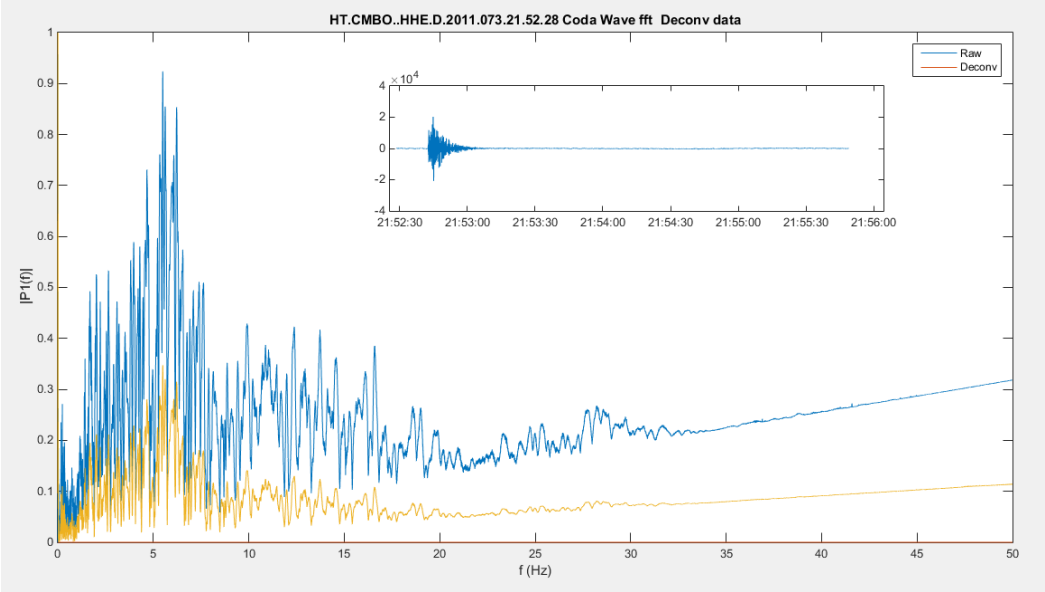

Figure 6.6 Frequency content for the seismic event of 2011.073.21.52.28 for CMBO station (HHE component), prior and after the deconvolution process.

After extensive manual analysis process, all seismic events were assigned with a quality index, with a proportional increase of importance.

Conf. Intervals	Quality Factor	Events		
Confidence intervals 95%	Quality 1	127	Error <0.1	Earthquake Events 350
	Quality 2	223		
	Quality 3	81		
	Quality 4	210		
	Quality 5	267		

Table 6.2 Analytic details of quality factor for all earthquake events, listed in the seismic catalogue of GEIN-NOA.

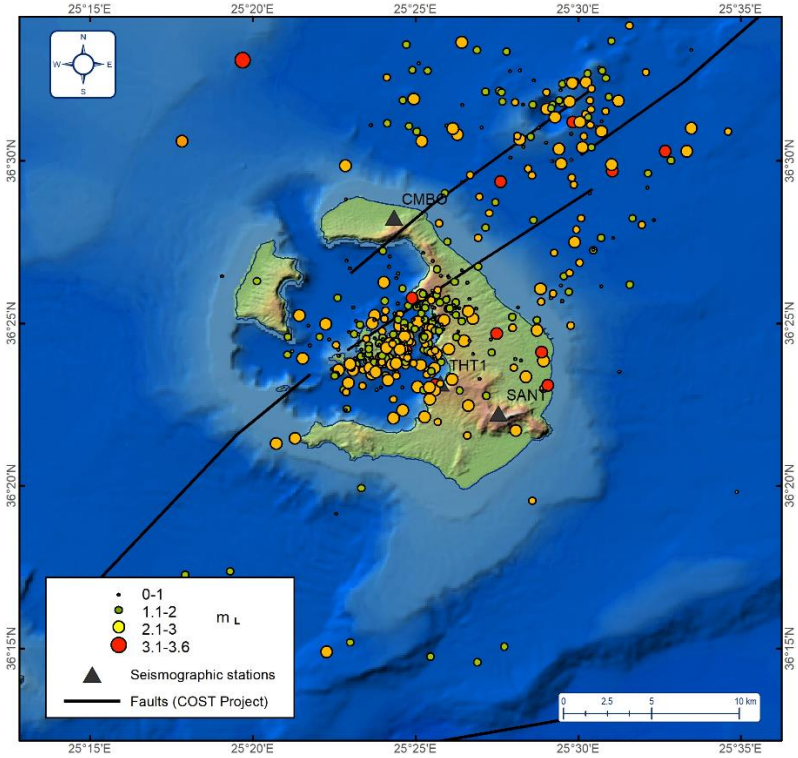

Figure 6.7 Earthquake events with quality factor 1 & 2.

7 Results

7.1 Temporal variation of q_s index

In order to have a physical insight of the scattering entropic index q_s throughout the unrest period of Santorini, we analyzed individual earthquake events from NOA's seismic catalogue in all three components, HHE, HHN and HHZ (for analytic explanation, see chapter 5.2).
The values of q_s are depicted with different colors (as seen in y-axis and legends) and the linear objects above and below individual solutions represent the errors, covering the area for the 95% of confidence interval, of the entropic scattering indices.
The error model that was used was constant, using a standard zero-mean and unit-variance 'C' as given below:

$$y = f + aC \qquad (7.1)$$

The confidence intervals were computed for 95% by using the estimated coefficients, retrieved from the nonlinear fitting procedure via Jacobian matrix.
In the following figures (Figure 7.1 to Figure 7.9) the temporal variation of the entropic scattering index q_s is presented.

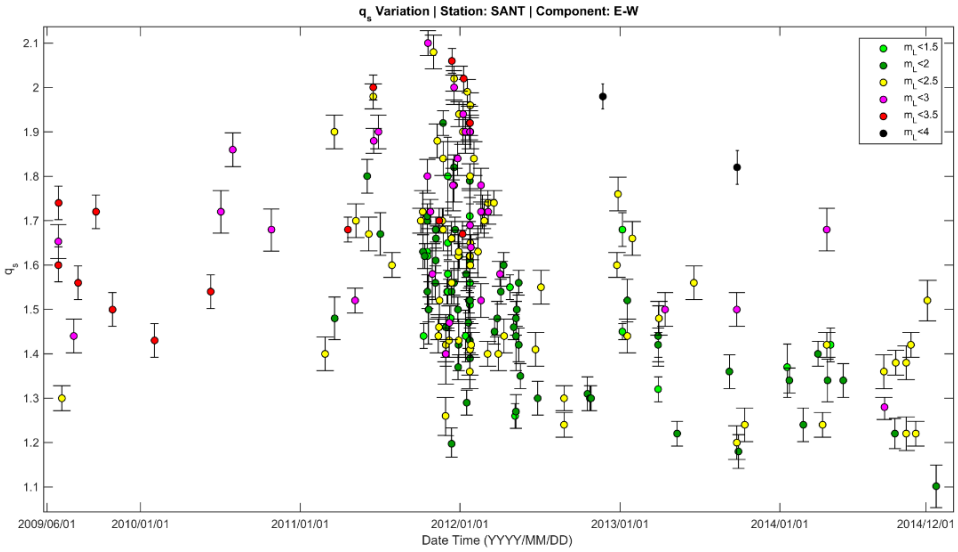

Figure 7.1 Temporal variation of q_s index for station SANT and for HHE component, prior, during and after the unrest period.

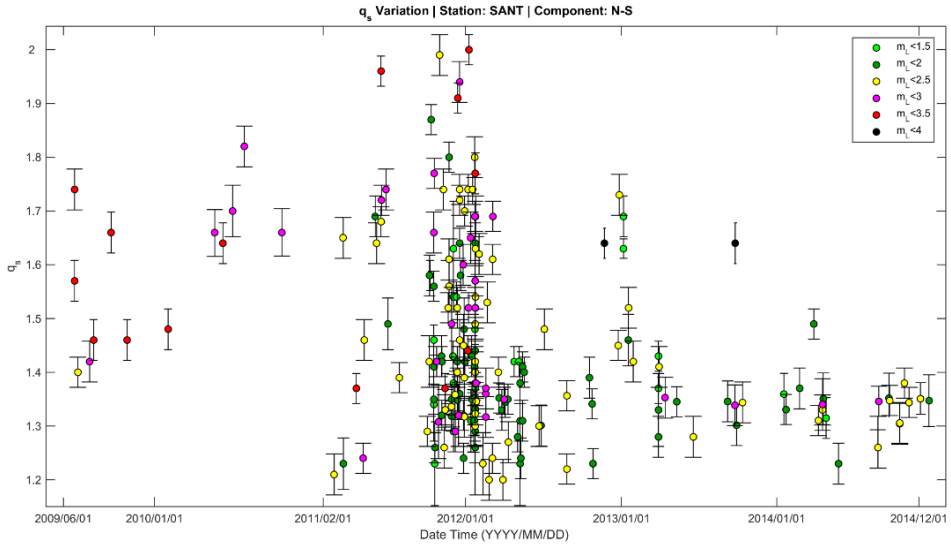

Figure 7.2 Temporal variation of q_s index for station SANT, for HHN component.

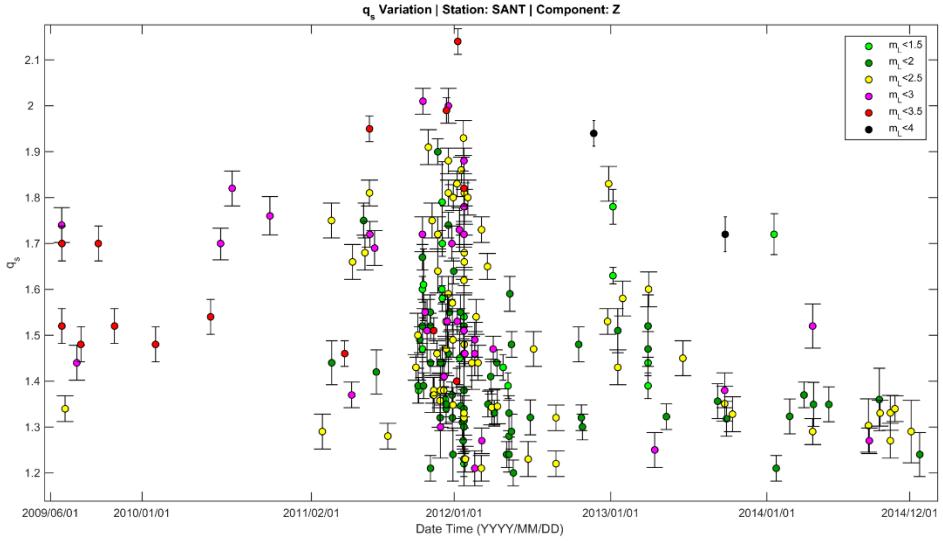

Figure 7.3 Temporal variation of q_s index for station SANT, for HHZ component.

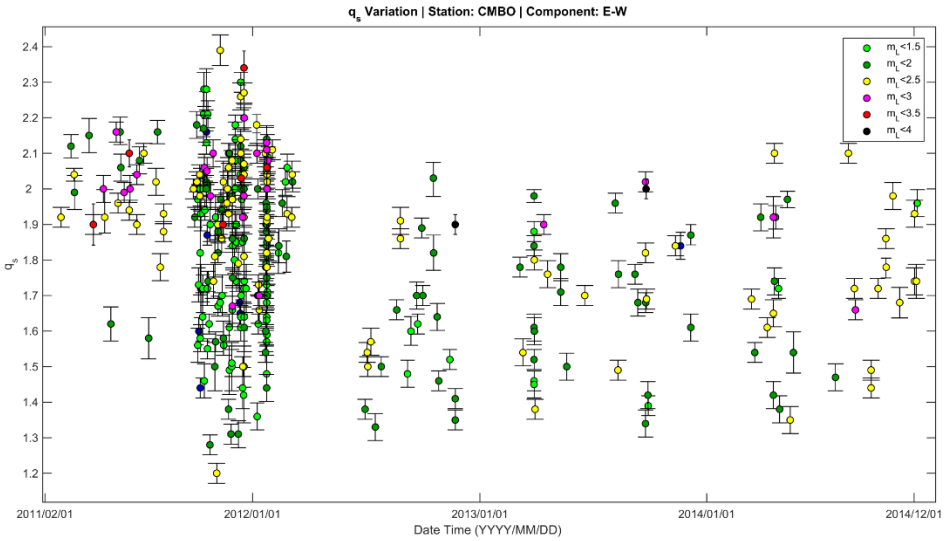

Figure 7.4 Temporal variation of q_s index for station CMBO, for HHE component.

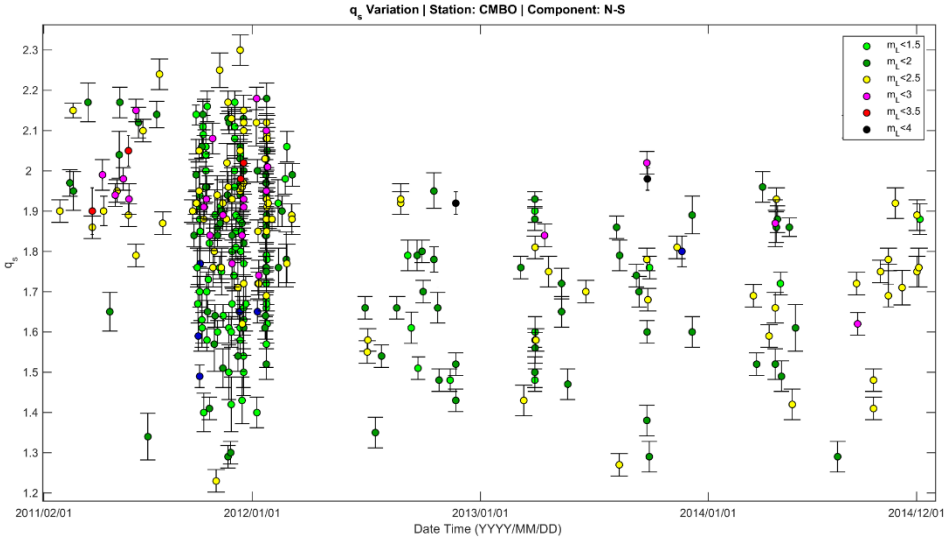

Figure 7.5 Temporal variation of q_s index for station CMBO, for HHN component.

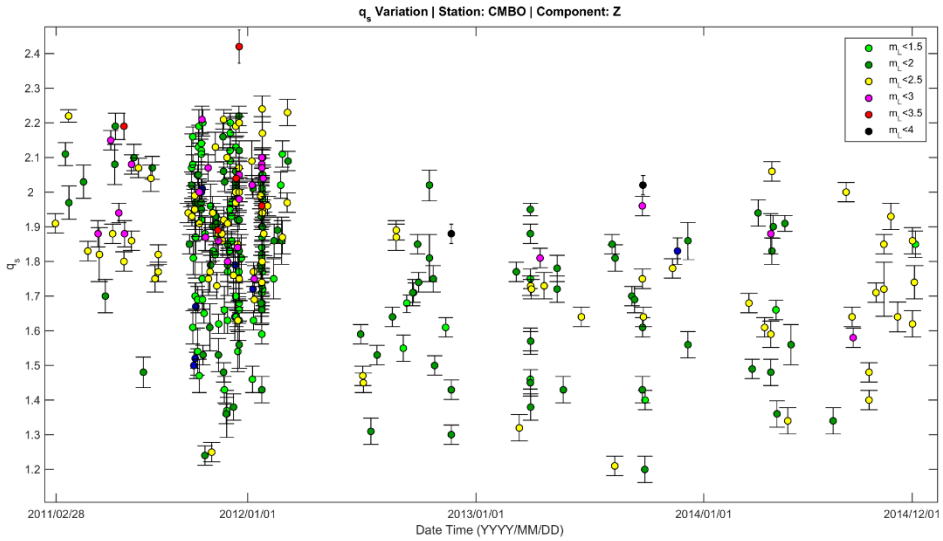

Figure 7.6 Temporal variation of q_s index for station CMBO, for HHZ component.

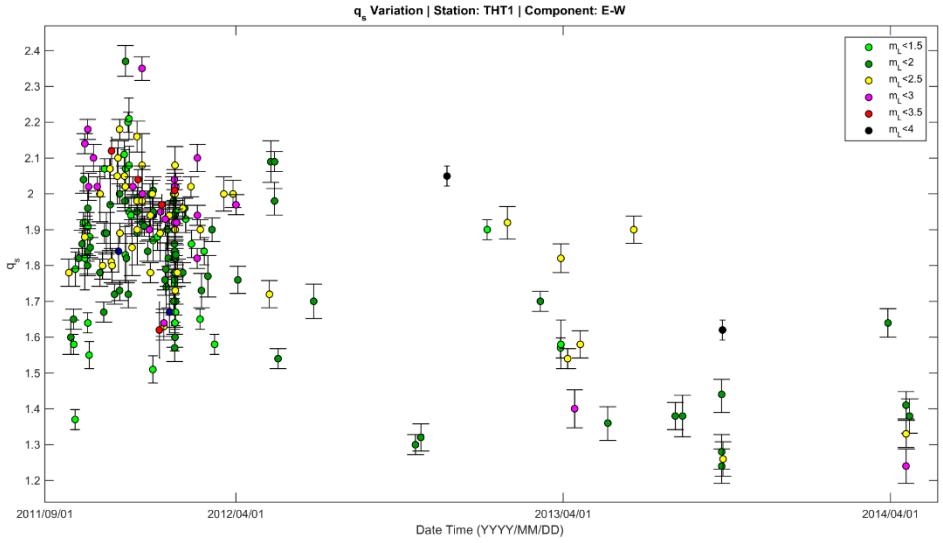

Figure 7.7 Temporal variation of q_s index for station THT1, for HHE component.

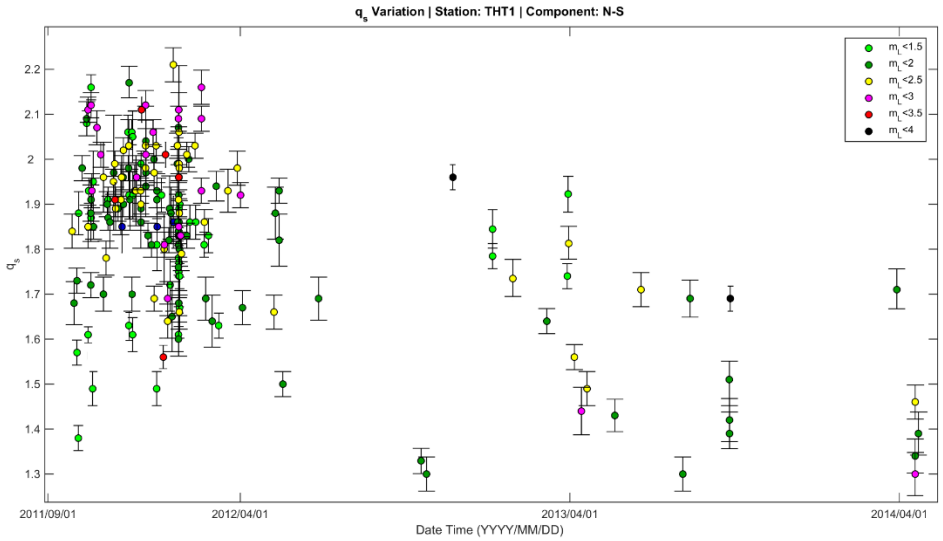

Figure 7.8 Temporal variation of q_s index for station THT1, for HHN component.

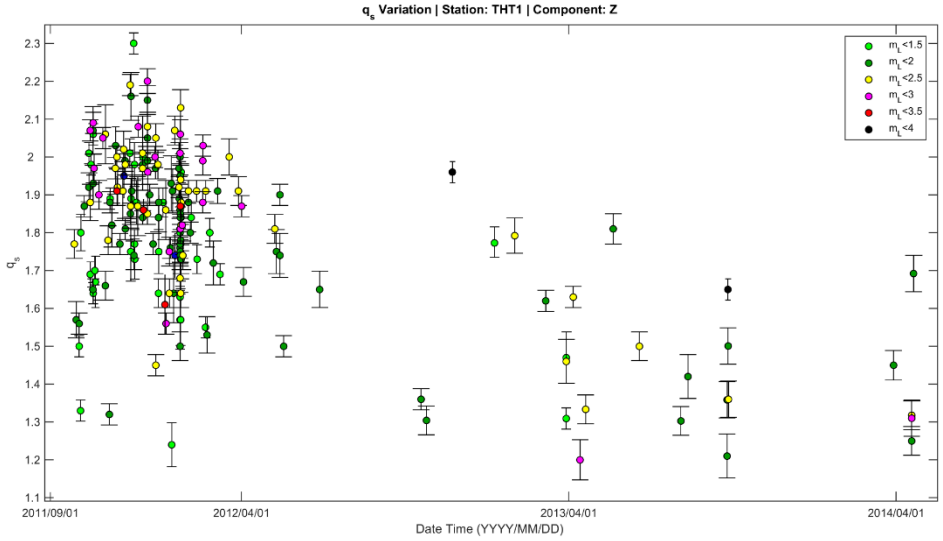

Figure 7.9 Temporal variation of q_s index for station THT1, for HHZ component.

7.2 Spatiotemporal variation of q_s index

Santorini's volcanic complex is an area with high tectonic activity. Especially in the case of volcanic activity, it can produce immense seismicity, mostly confined within the Kameni and

Columbo tectono-volcanic lineaments. These major tectonic features can be seen in the presented maps, as two linear black objects with NE to SW orientation, following the stress-field of the wider area. In order to retrieve information of the dynamically changing entropic index, a physical property of the medium, we investigate the q_s variations both in space and time.

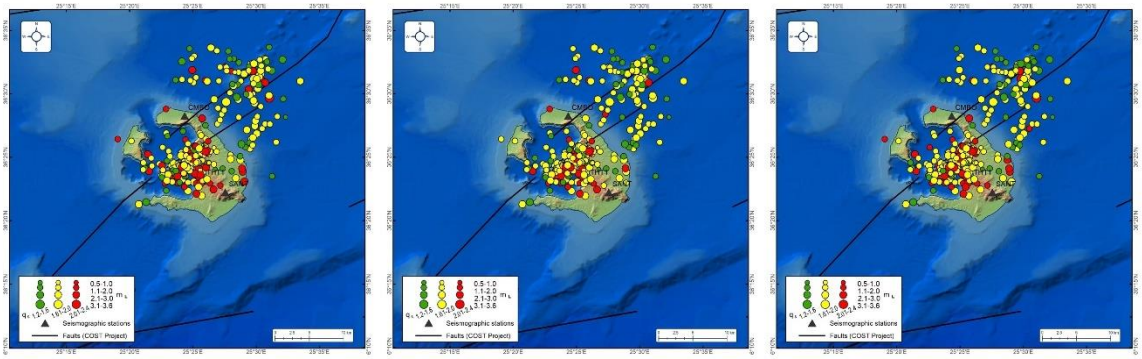

Figure 7.10 The q_s variation for CMBO station during the unrest period. Component E-W (left), N-S (middle), Z (right).

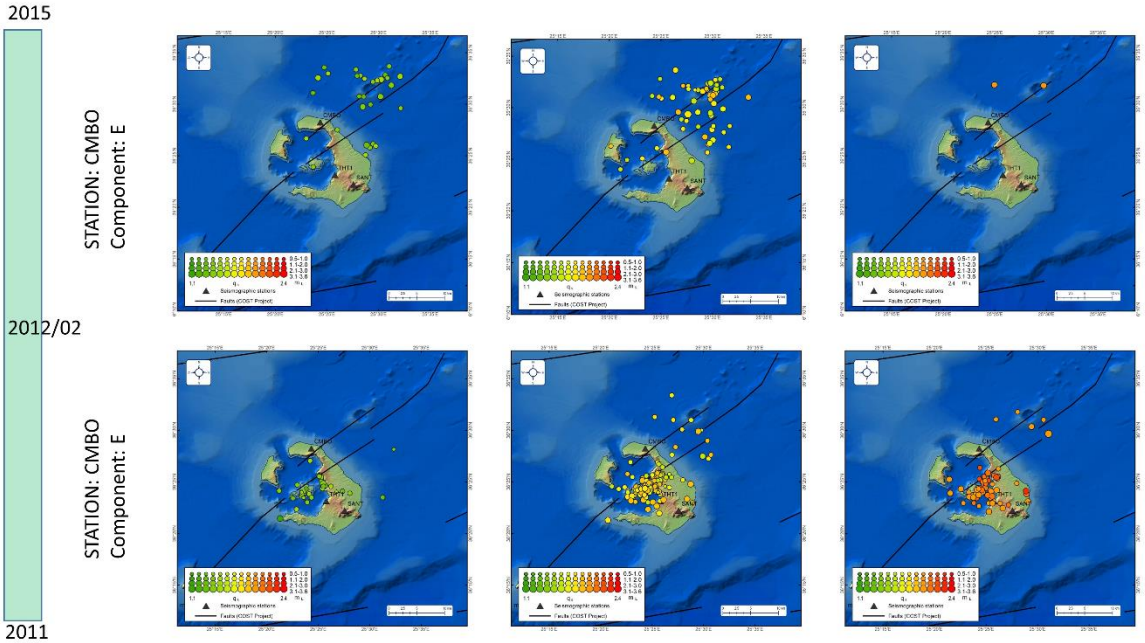

Figure 7.11 Spatial distribution for different values of the q_s index for station CMBO and E-W component, before and after the critical point of 02/2012 where the seismicity reduced dramatically.

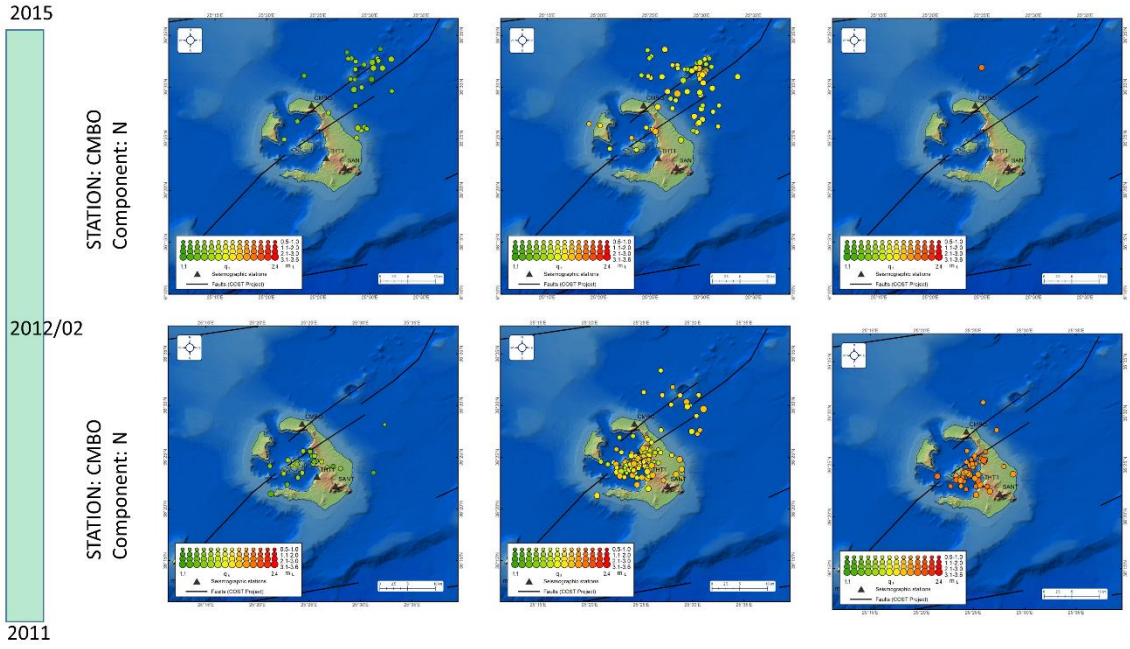

Figure 7.12 Spatial distribution for different values of the q_s index for station CMBO and N-S component, before and after the critical point of 02/2012 where the seismicity reduced dramatically.

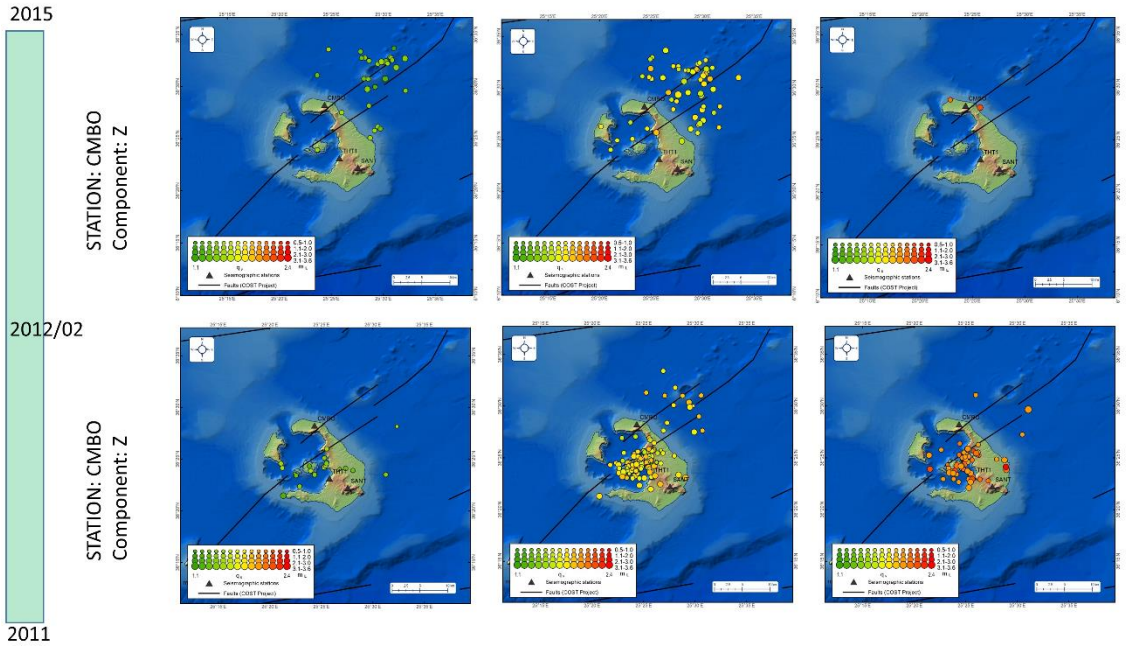

Figure 7.13 Spatial distribution for different values of the q_s index for station CMBO and Z component, before and after the critical point of 02/2012 where the seismicity reduced dramatically.

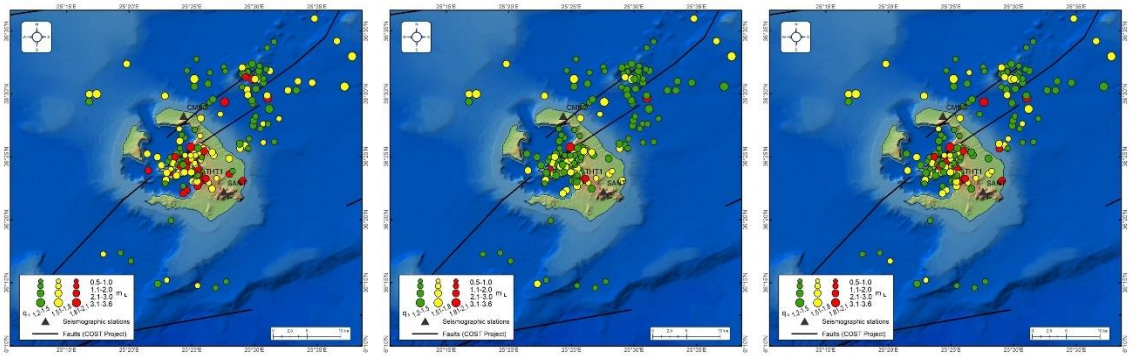

Figure 7.14 The q_s variation for SANT station. Component E-W (left), N-S (middle), Z (right).

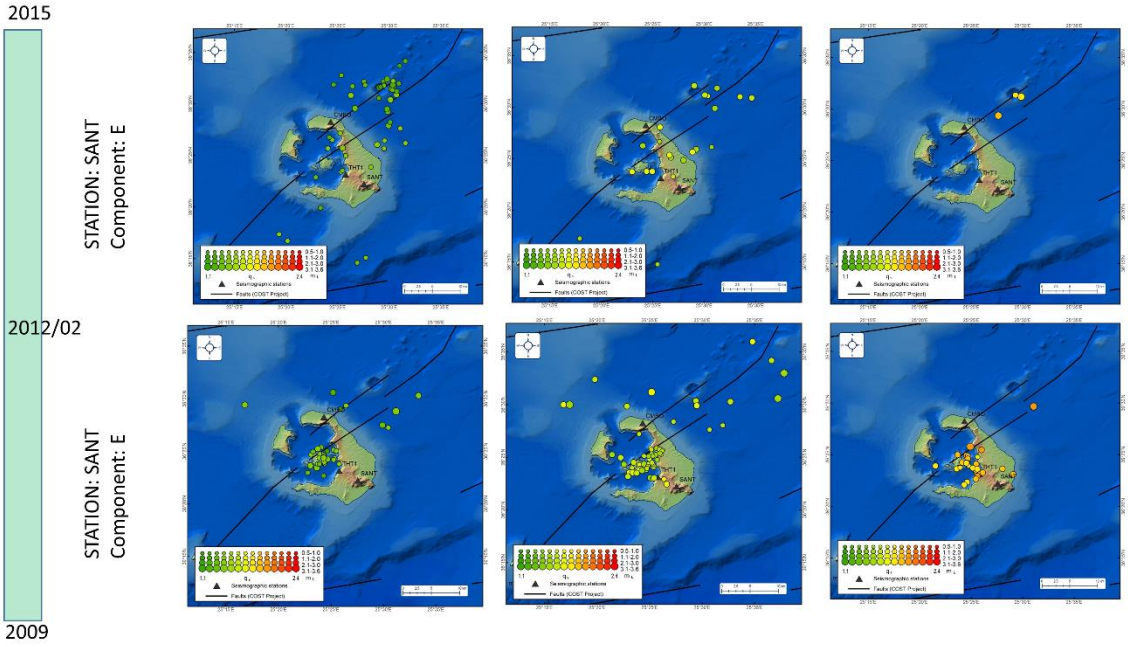

Figure 7.15 Spatial distribution for different values of the q_s index for station SANT and E-W component, before and after the critical point of 02/2012 where the seismicity reduced dramatically.

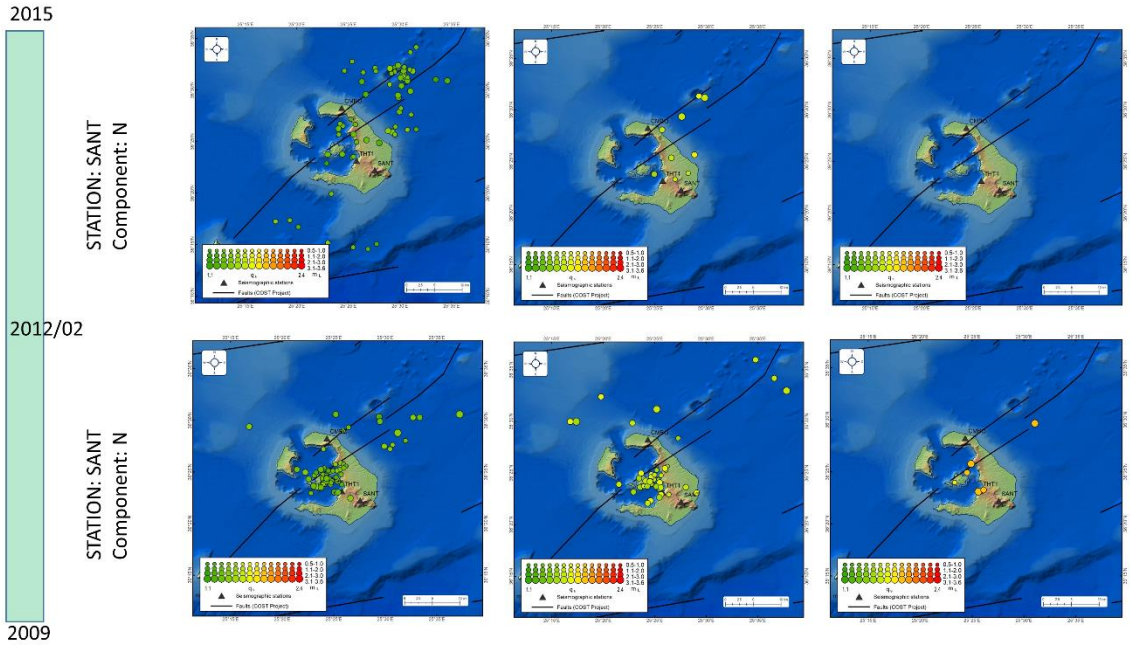

Figure 7.16 Spatial distribution for different values of the q_s index for station SANT and N-S component, before and after the critical point of 02/2012 where the seismicity reduced dramatically.

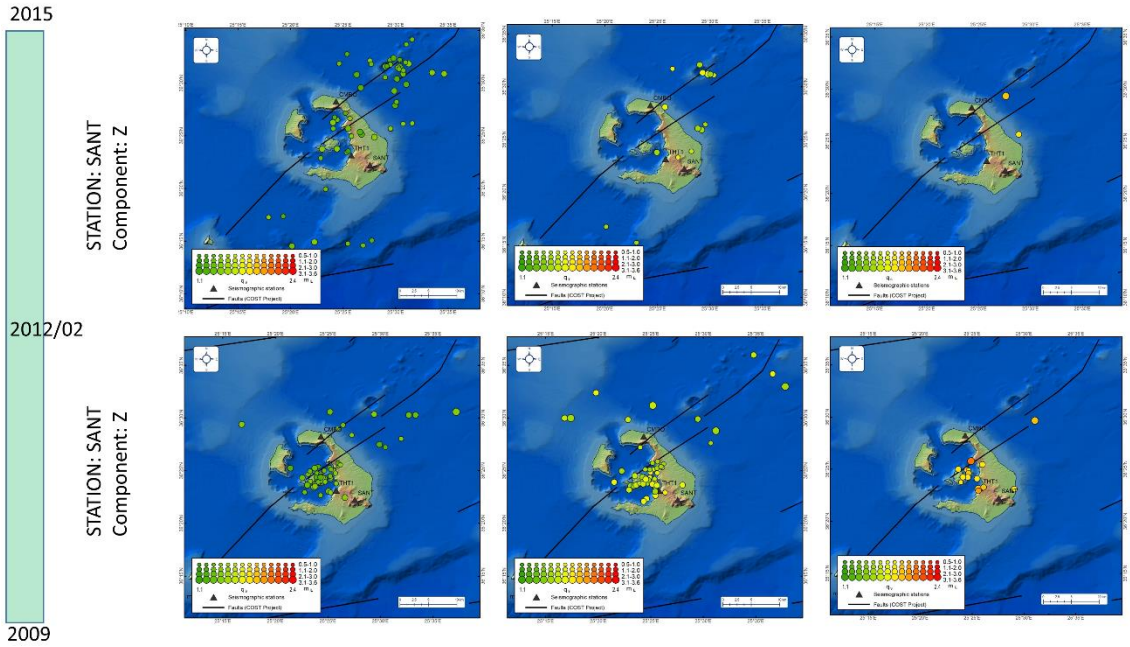

Figure 7.17 Spatial distribution for different values of the q_s index for station SANT and Z component, before and after the critical point of 02/2012 where the seismicity reduced dramatically.

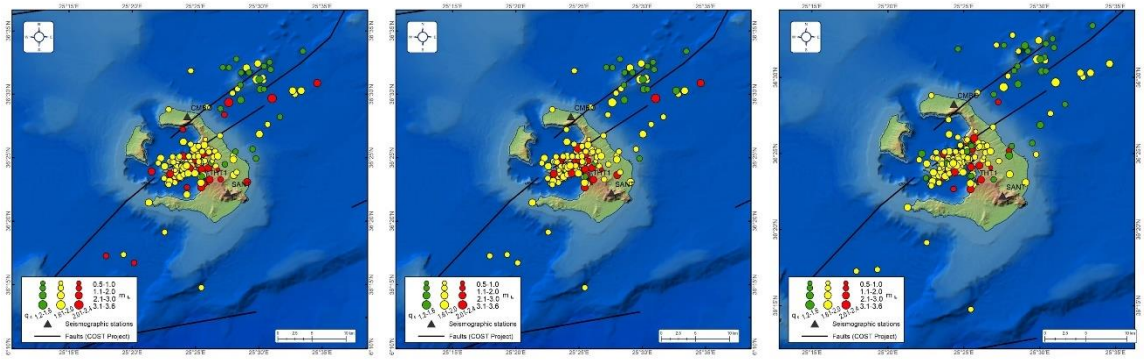

Figure 7.18 The q_s variation for THT1 station. Component E-W (left), N-S (middle), Z (right).

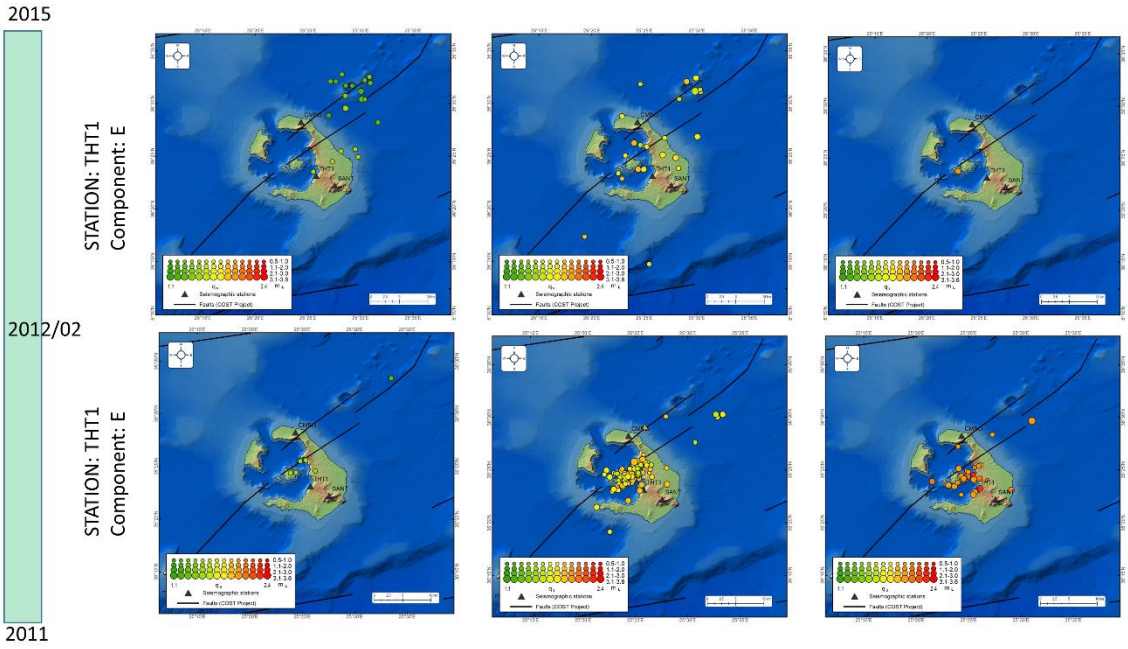

Figure 7.19 Spatial distribution for different values of the q_s index for station THT1 and E-W component, before and after the critical point of 02/2012 where the seismicity reduced dramatically.

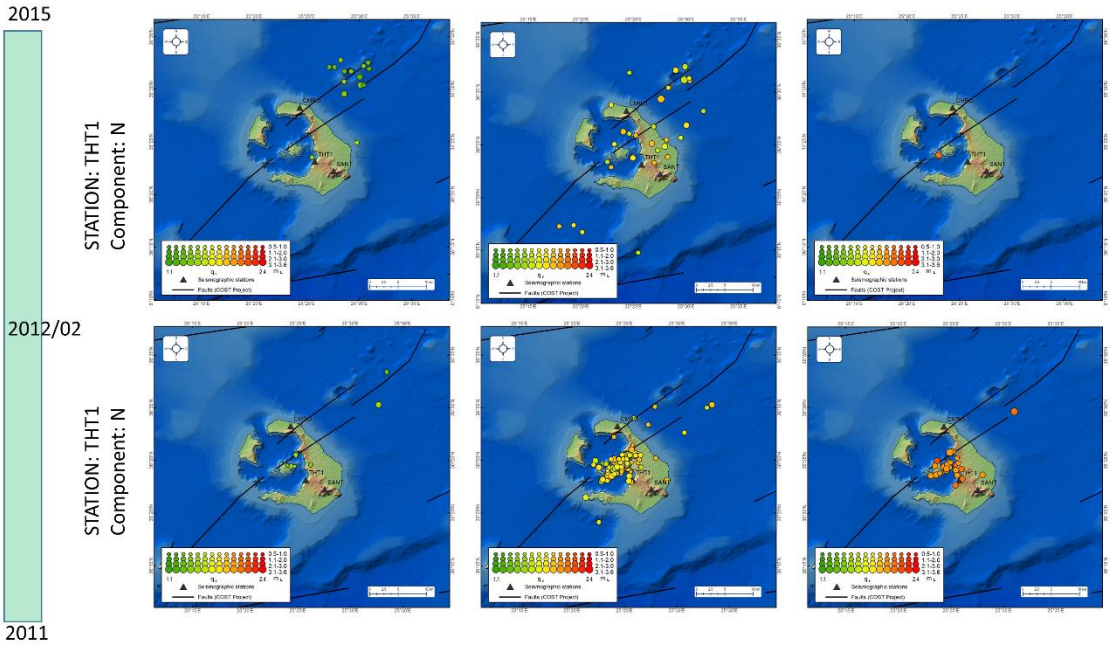

Figure 7.20 Spatial distribution for different values of the q_s index for station THT1 and N-S component, before and after the critical point of 02/2012 where the seismicity reduced dramatically.

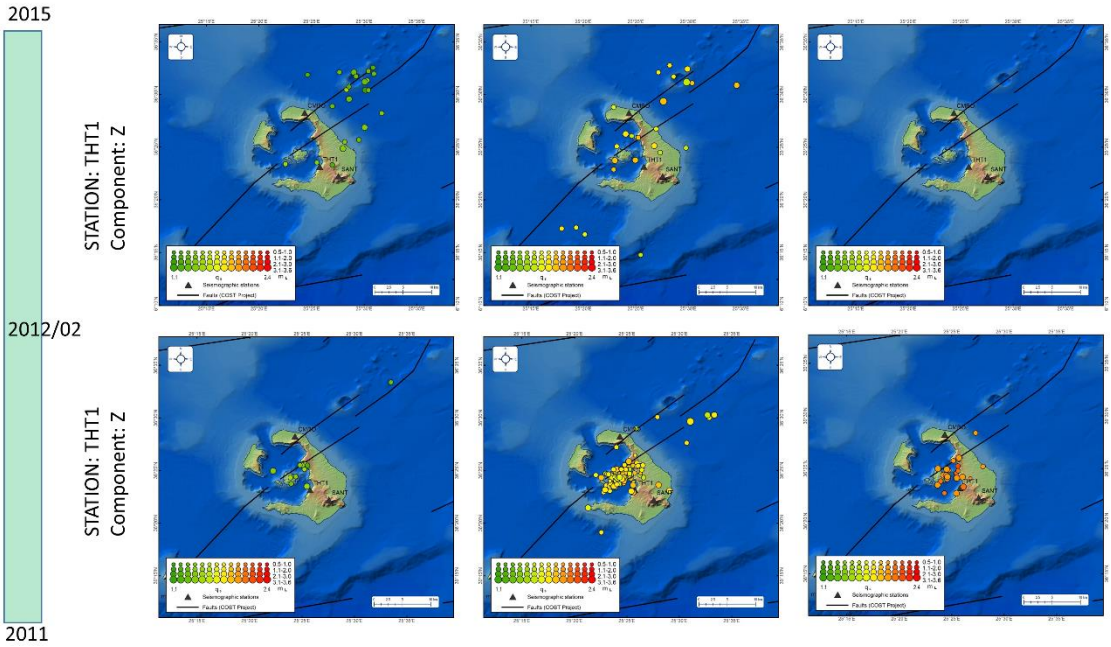

Figure 7.21 Spatial distribution for different values of the q_s index for station THT1 and Z component, before and after the critical point of 02/2012 where the seismicity reduced dramatically.

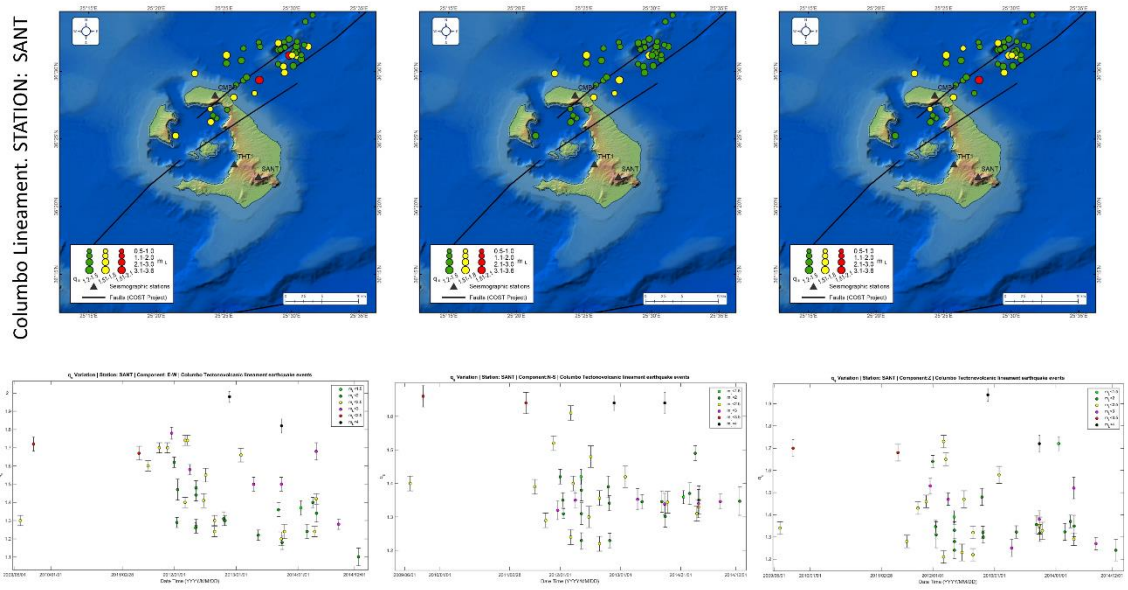

Figure 7.22 Spatial distribution of q_s along the Columbo tectonovolcanic lineament throughout the unrest period for station SANT. Component E-W (right), N-S (middle) and Z (left).

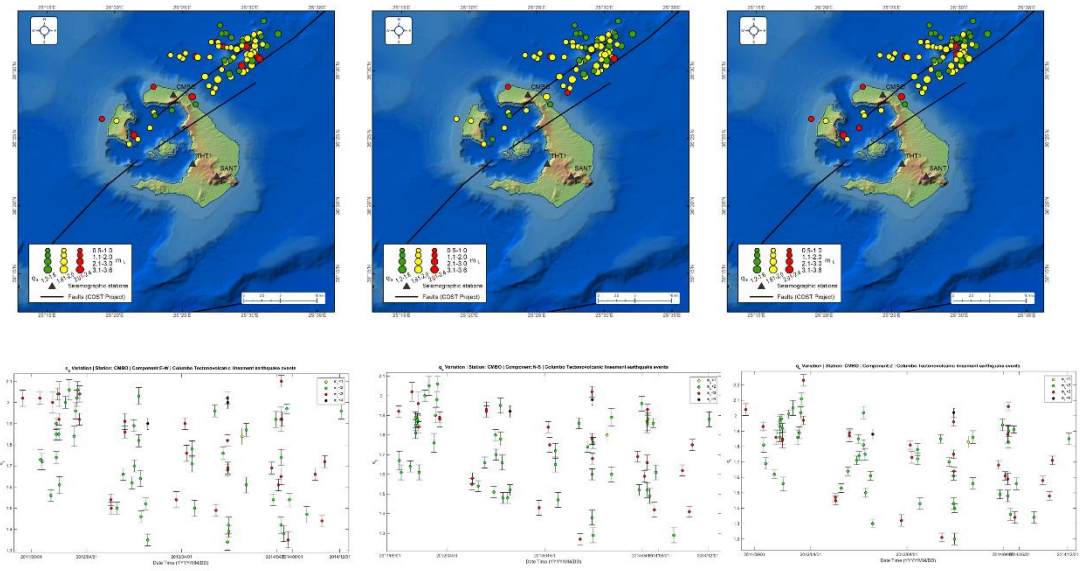

Figure 7.23 Spatial distribution of q_s along the Columbo tectonovolcanic lineament throughout the unrest period for station CMBO. Component E-W (right), N-S (middle) and Z (left).

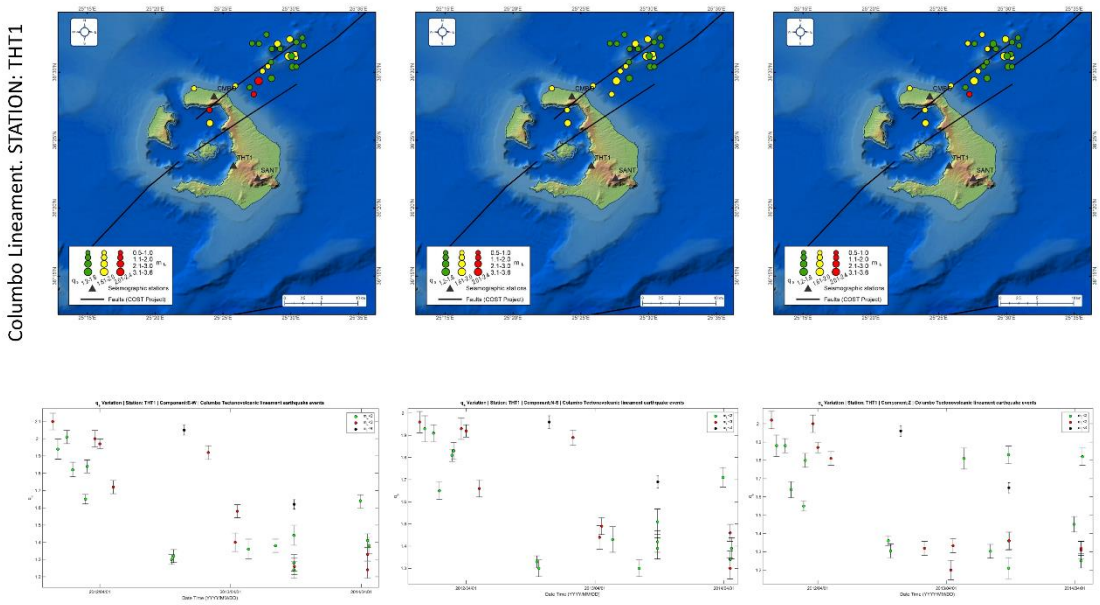

Figure 7.24 Spatial distribution of q_s along the Columbo tectonovolcanic lineament throughout the unrest period for station THT1. Component E-W (right), N-S (middle) and Z (left).

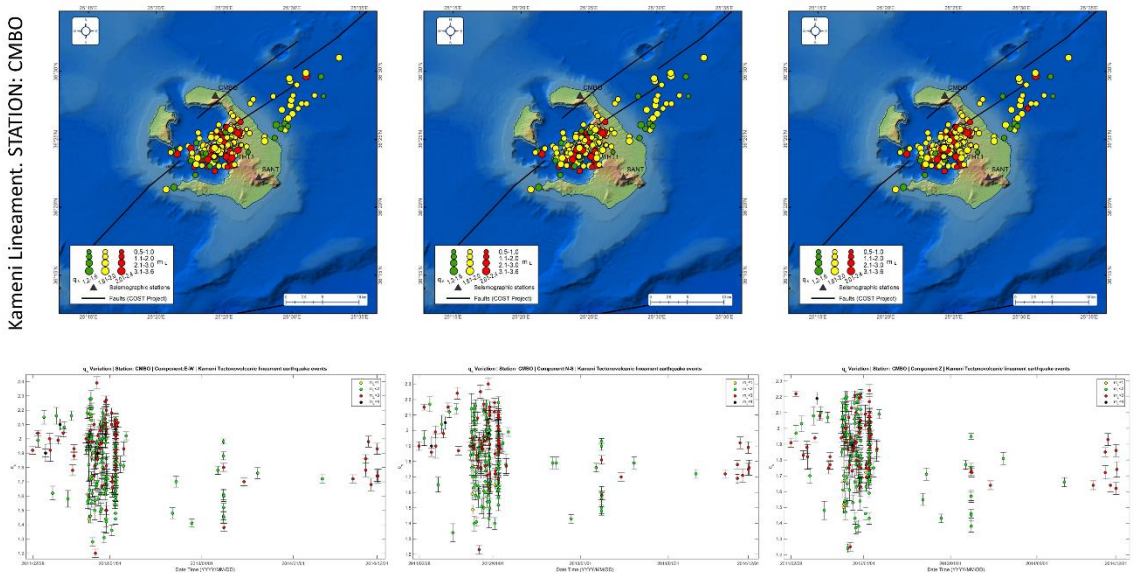

Figure 7.25 Spatial distribution of q_s along the Kameni tectonovolcanic lineament throughout the unrest period for station CMBO. Component E-W (right), N-S (middle) and Z (left).

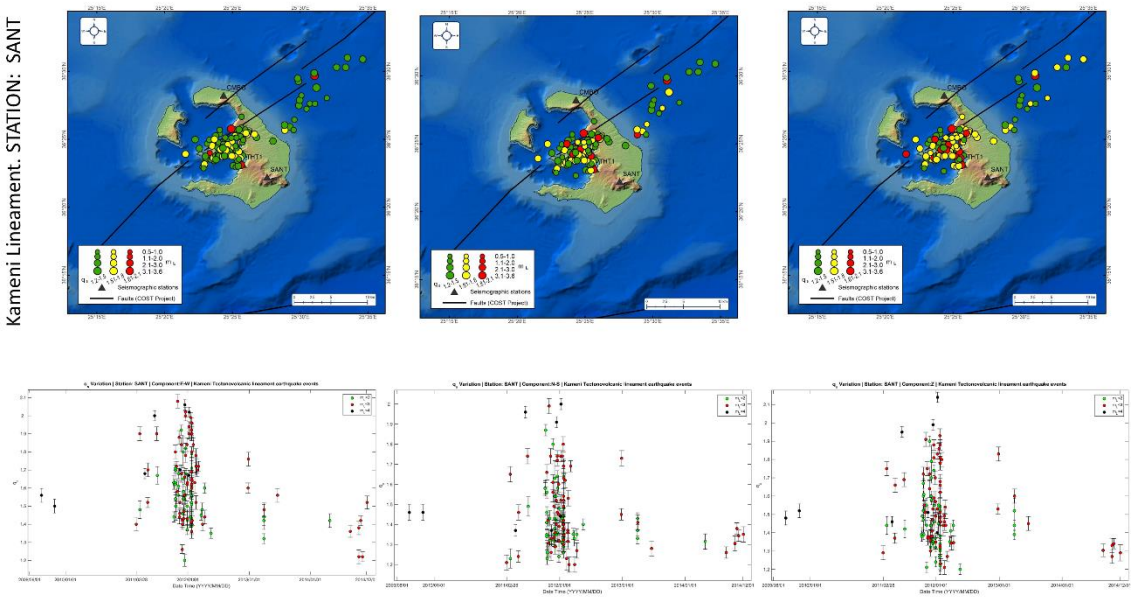

Figure 7.26 Spatial distribution of q_s along the Kameni tectonovolcanic lineament throughout the unrest period for station SANT. Component E-W (right), N-S (middle) and Z (left).

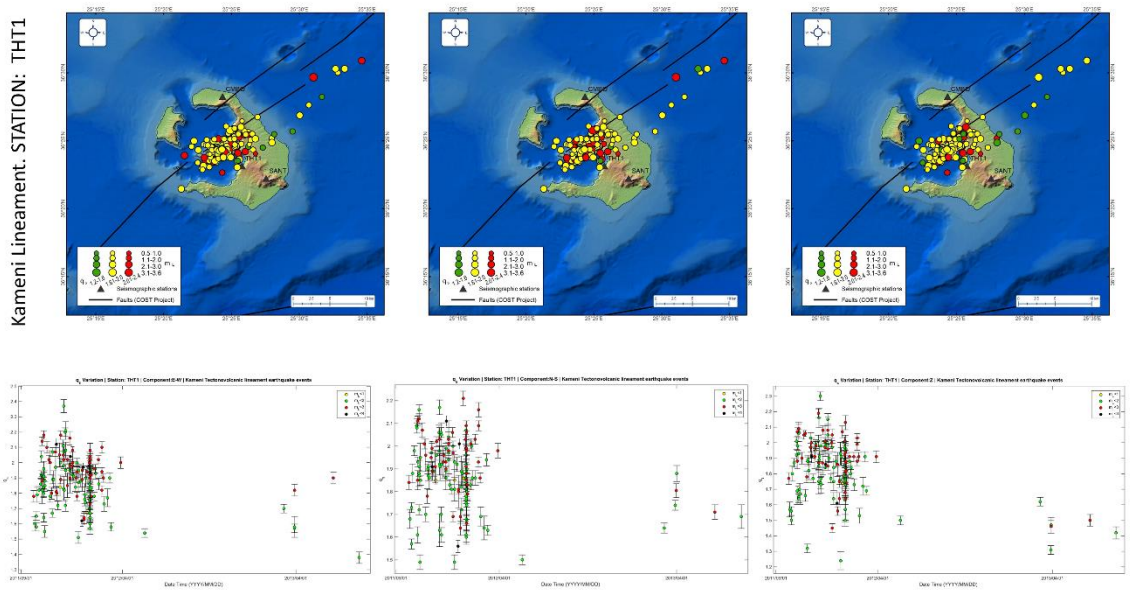

Figure 7.27 Spatial distribution of q_s along the Kameni tectonovolcanic lineament throughout the unrest period for station THT1. Component E-W (right), N-S (middle) and Z (left).

7.3 Statistical overview of q_s index

The statistical analysis of the entropic scattering index, revealed a relation with the observed local magnitude (M_L) and epicentral distance (measured in km.). The statistical overview of the q_s was conducted via the boxplot procedure. This approach manifests information from a seven-number summary. It is not presenting a distribution, as a histogram does, but it gives useful information about the spread of a distribution and if this distribution is skewed about the range of its values away from median, as well as individual outliers. In more details, rectangle boxes, as given in the following figures, represent the upper and the lower quartiles of the observed data (q_s indices).
The interquartile box area contains the range between the 25th and 75th percentiles. The second quartile index, depicted with a red parallel line with the x axis within the box, represents the median value. The line black objects, extended above and below the boxes, are called whiskers and represent extreme data, not considered to be outlier values. The outlier values are given individually at the edges of each whisker diagram (box plot) as red crosses.

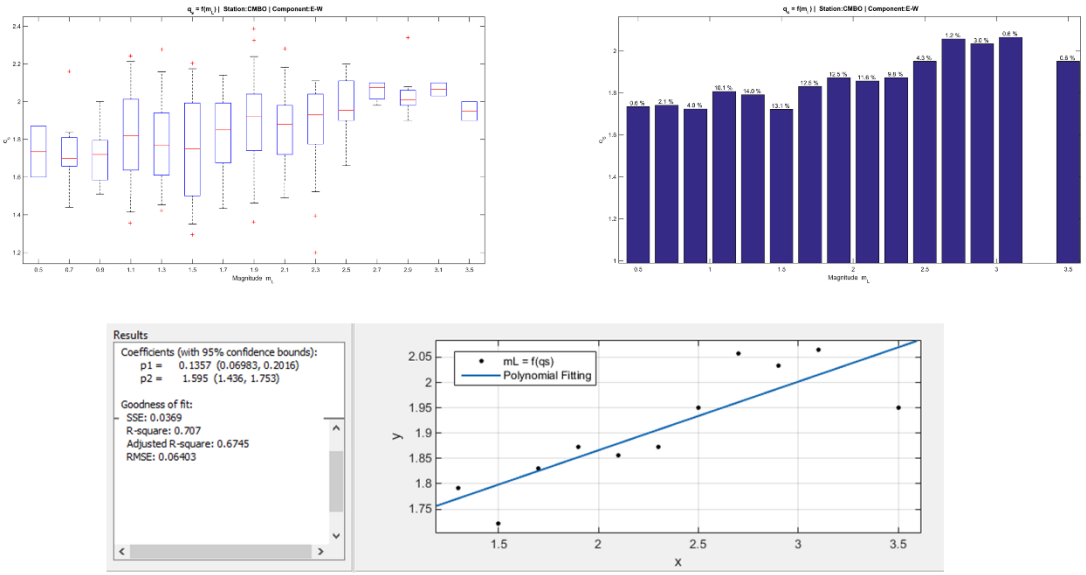

Figure 7.28 Whisker plot statistical analysis of q_s as a function of local magnitude (M_L) for station CMBO and E-W component.

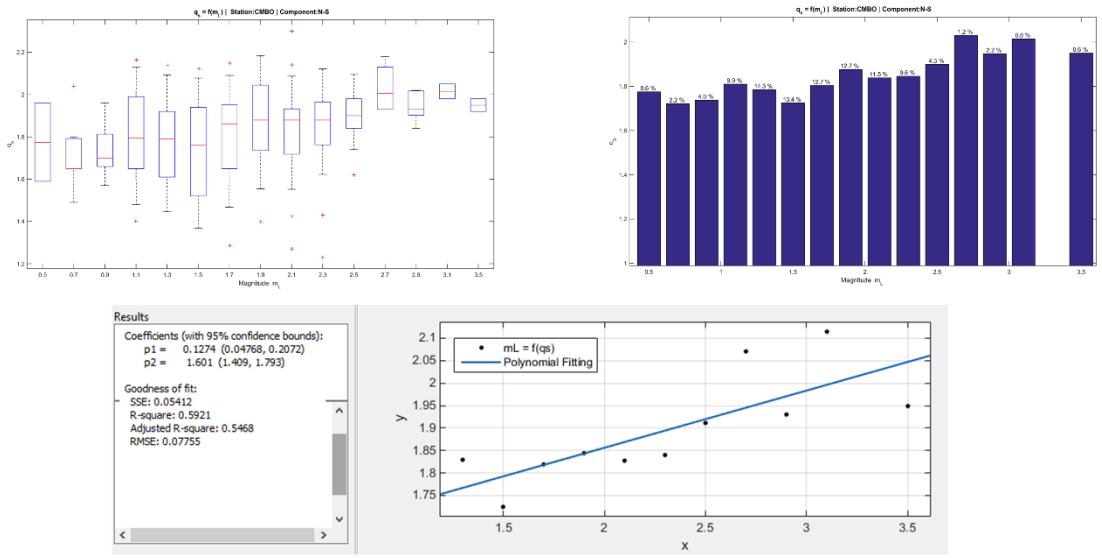

Figure 7.29 Whisker plot statistical analysis of q_s as a function of local magnitude (M_L) for station CMBO and N-S component.

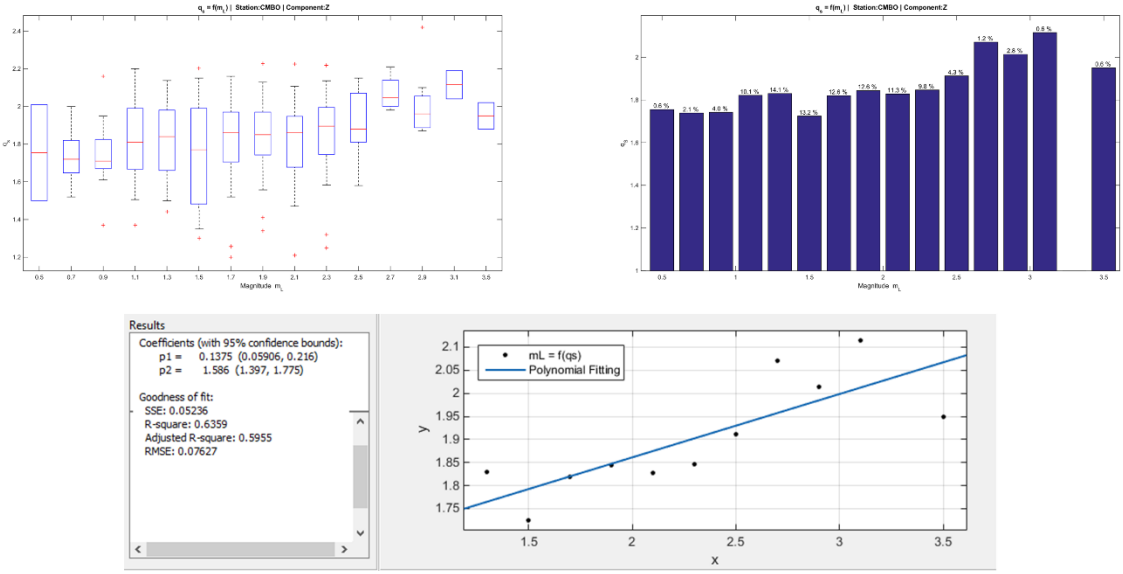

Figure 7.30 Whisker plot statistical analysis of q_s as a function of local magnitude (M_L) for station CMBO and Z component.

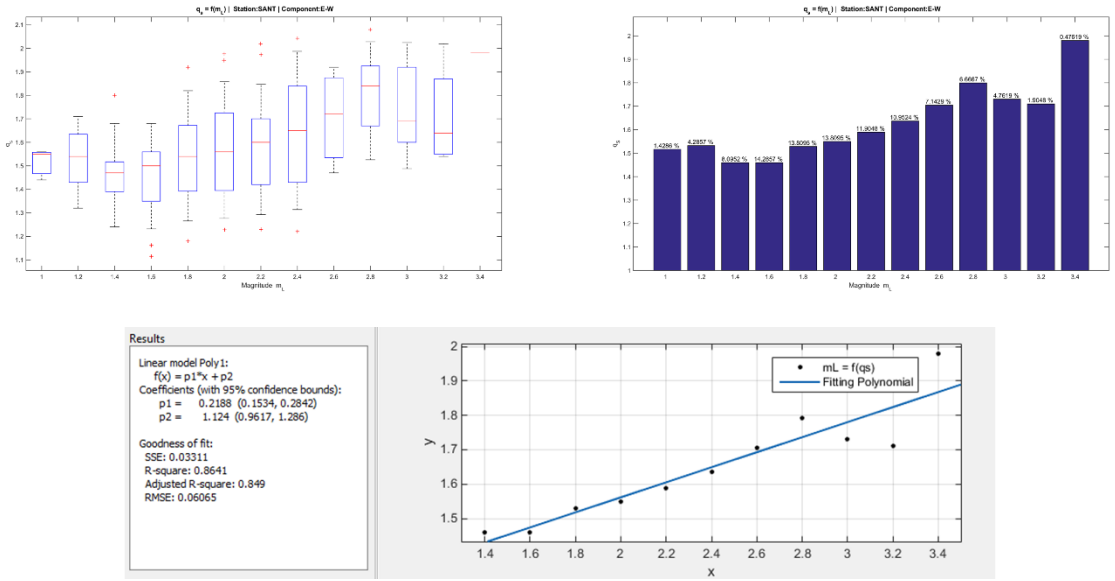

Figure 7.31 Whisker plot statistical analysis of q_s as a function of local magnitude (M_L) for station SANT and E-W component.

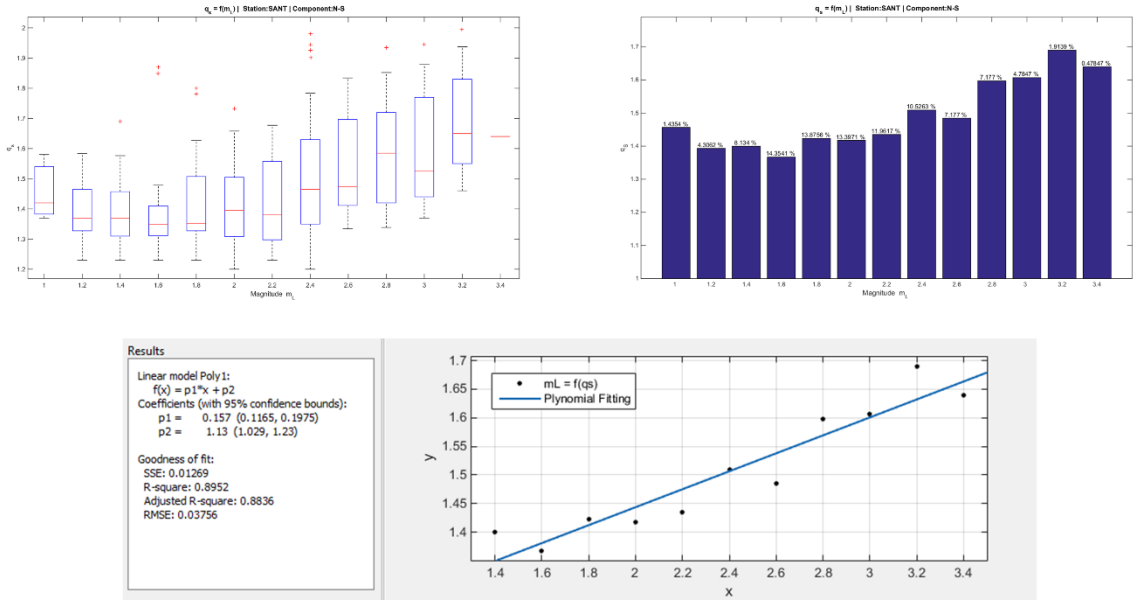

Figure 7.32 Whisker plot statistical analysis of q_s as a function of local magnitude (M_L) for station SANT and N-S component.

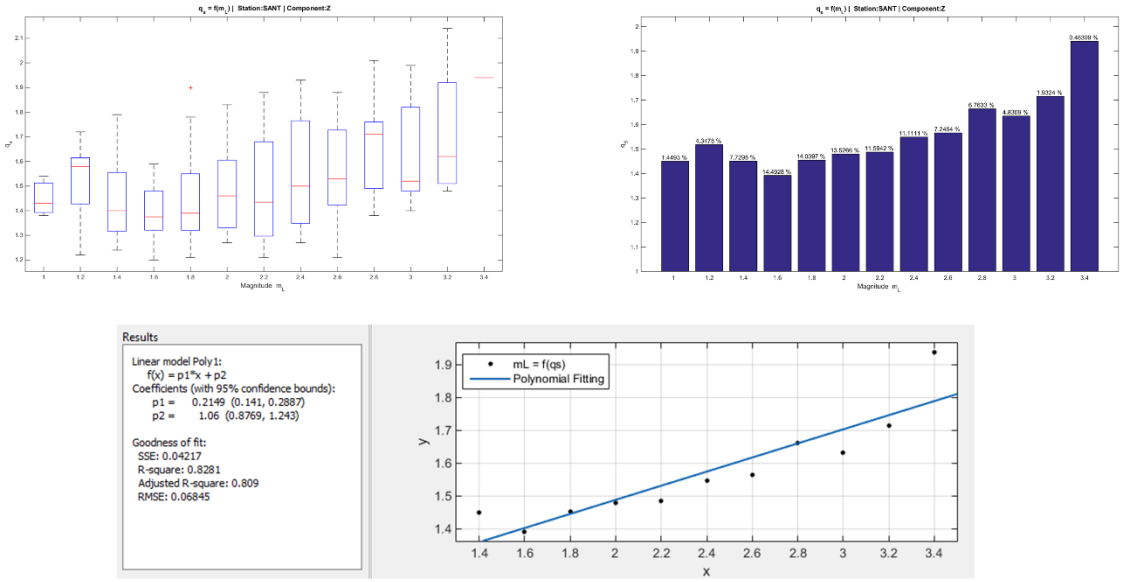

Figure 7.33 Whisker plot statistical analysis of q_s as a function of local magnitude (M_L) for station SANT and Z component.

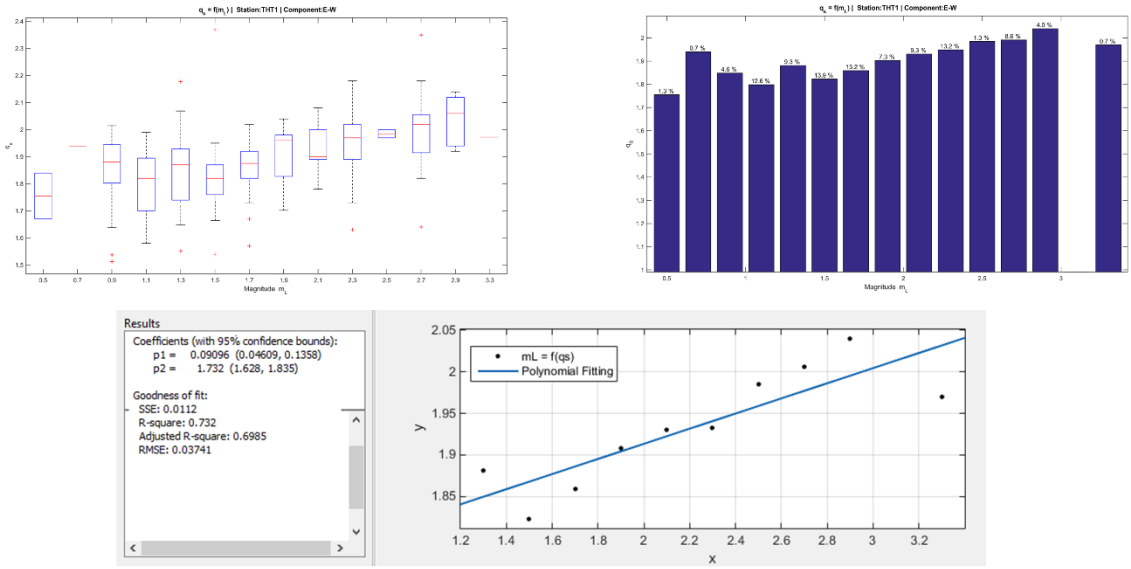

Figure 7.34 Whisker plot statistical analysis of q_s as a function of local magnitude (M_L) for station THT1 and E-W component.

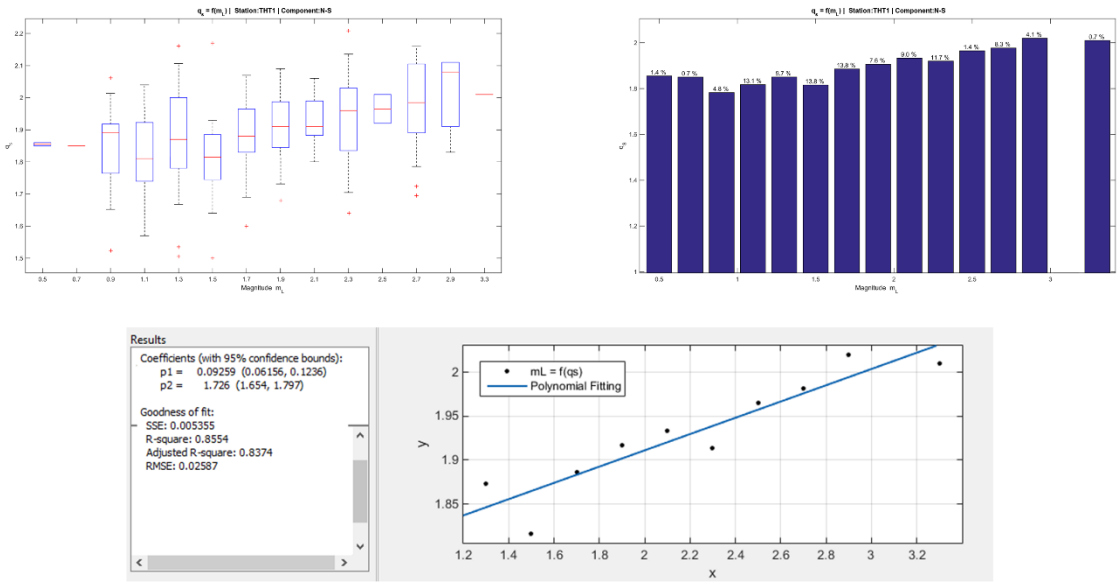

Figure 7.35 Whisker plot statistical analysis of q_s as a function of local magnitude (M_L) for station THT1 and N-S component.

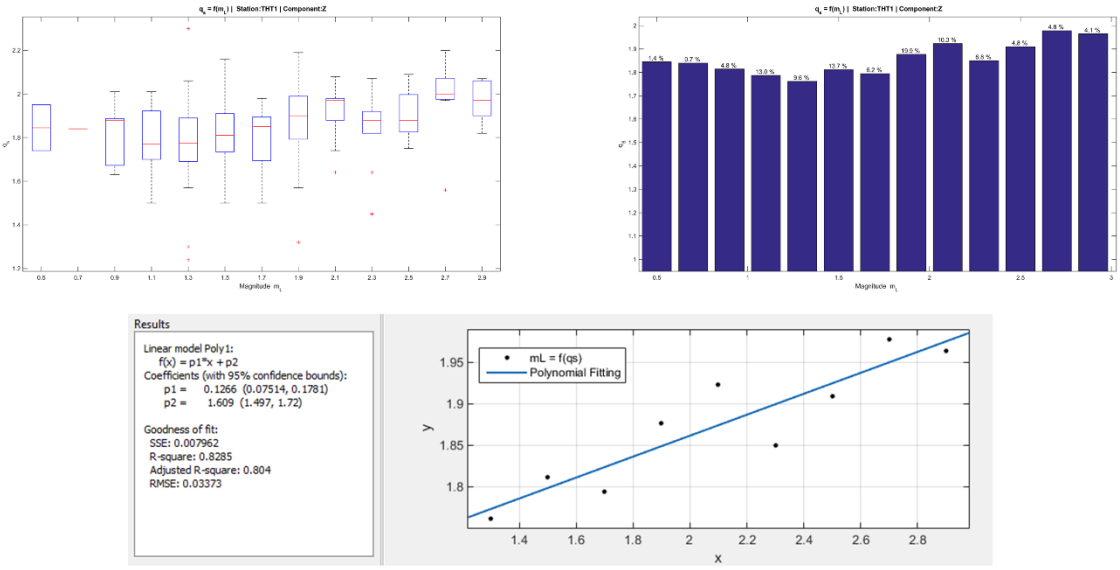

Figure 7.36 Whisker plot statistical analysis of q_s as a function of local magnitude (M_L) for station THT1 and Z component.

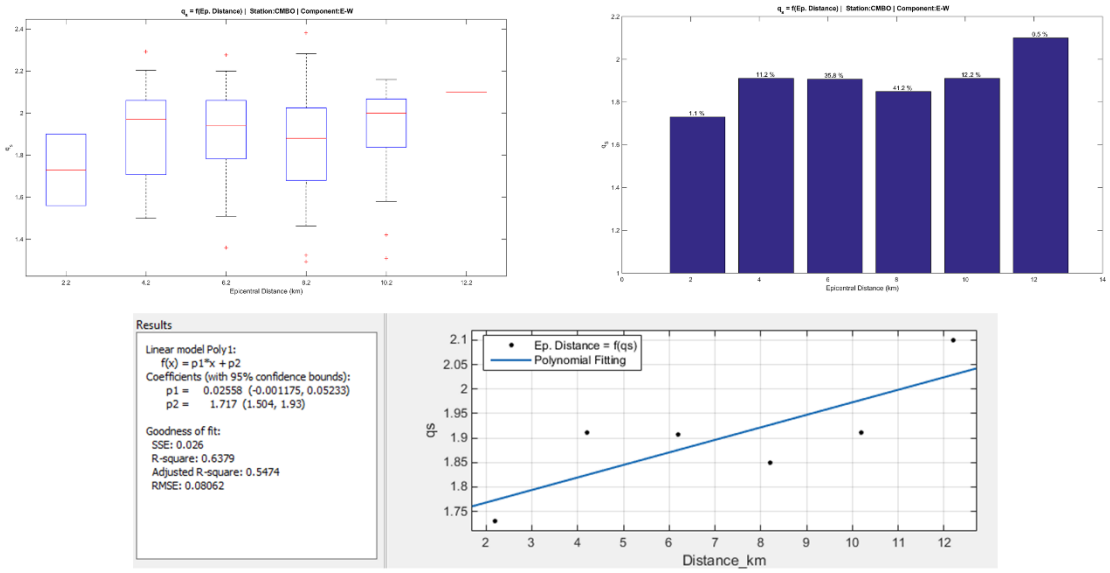

Figure 7.37 Whisker plot statistical analysis of q_s as a function of epicentral distance (measured in km) for station CMBO and E-W component.

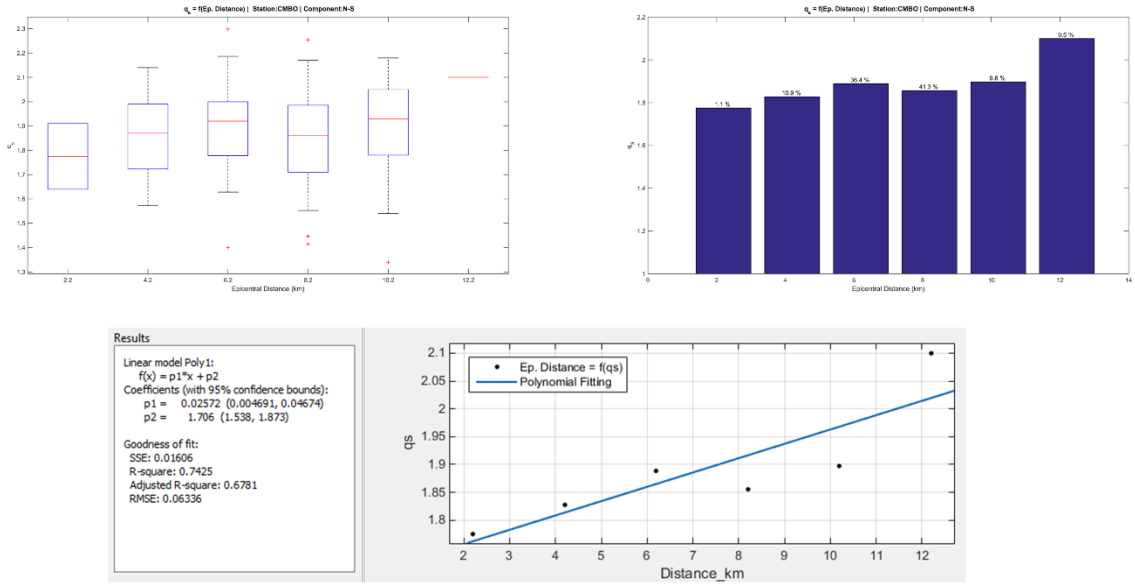

Figure 7.38 Whisker plot statistical analysis of q_s as a function of epicentral distance (measured in km) for station CMBO and N-S component.

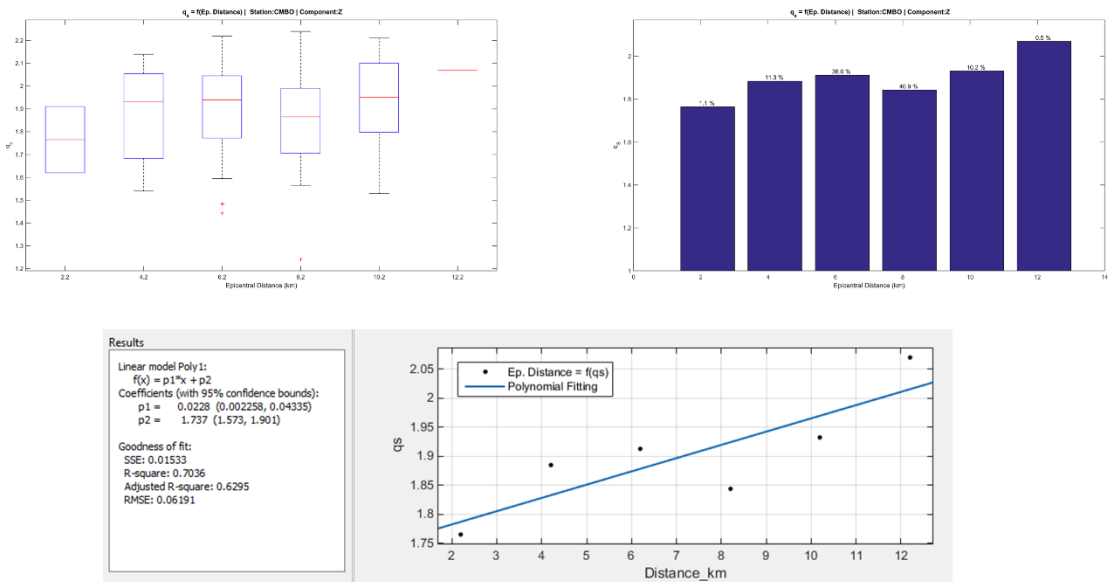

Figure 7.39 Whisker plot statistical analysis of q_s as a function of epicentral distance (measured in km) for station CMBO and Z component.

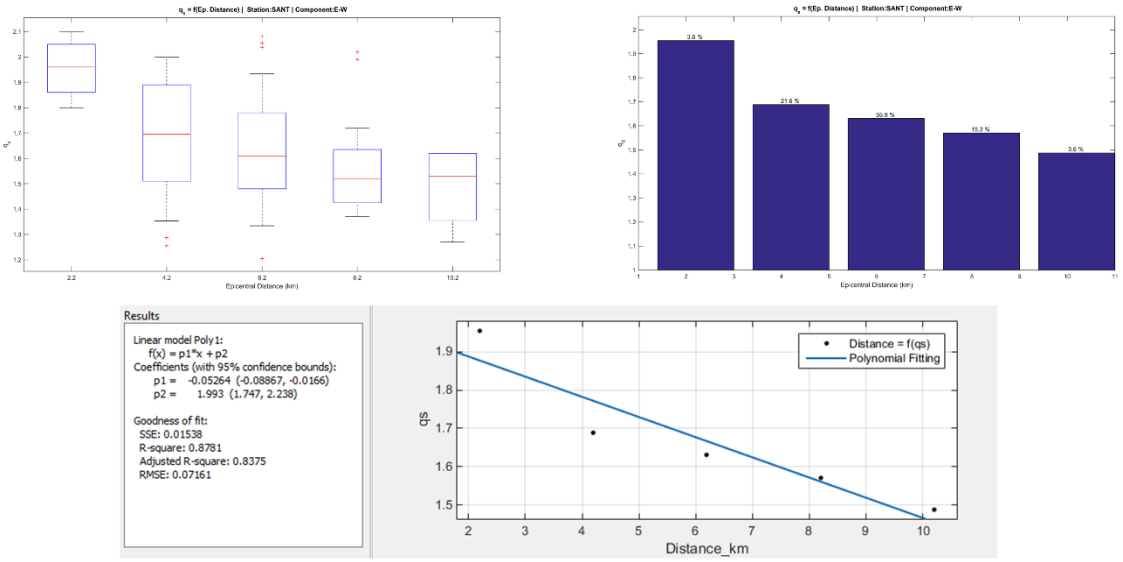

Figure 7.40 Whisker plot statistical analysis of q_s as a function of epicentral distance (measured in km) for station SANT and E-W component.

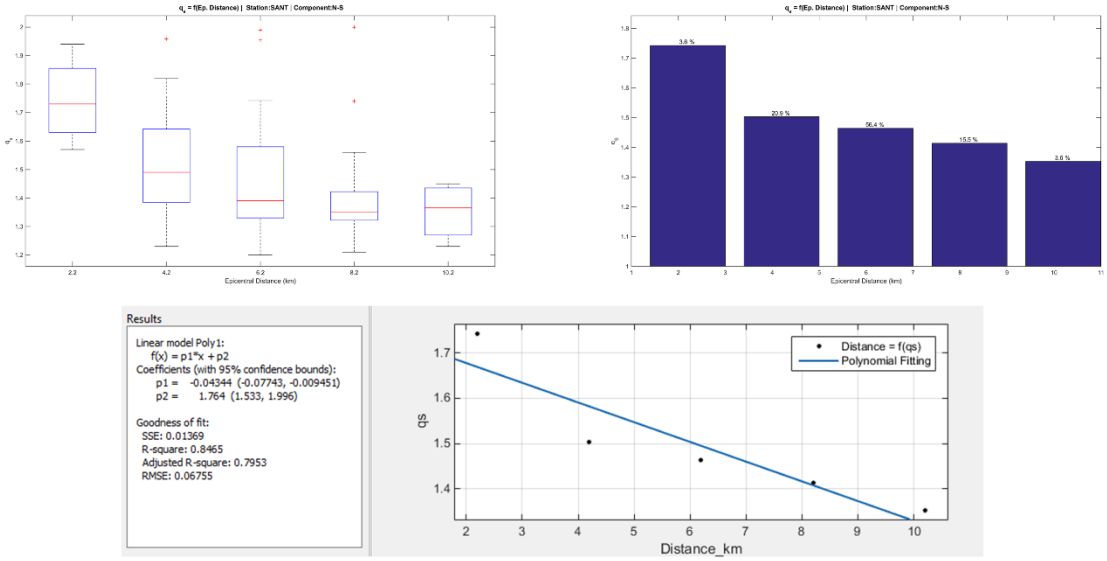

Figure 7.41 Whisker plot statistical analysis of q_s as a function of epicentral distance (measured in km) for station SANT and N-S component.

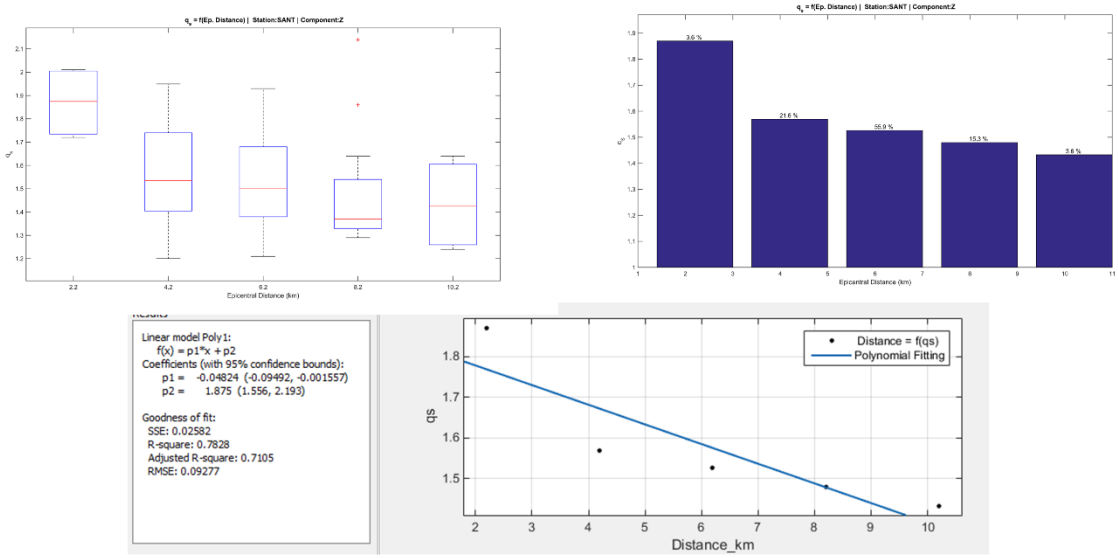

Figure 7.42 Whisker plot statistical analysis of q_s as a function of epicentral distance (measured in km) for station SANT and Z component.

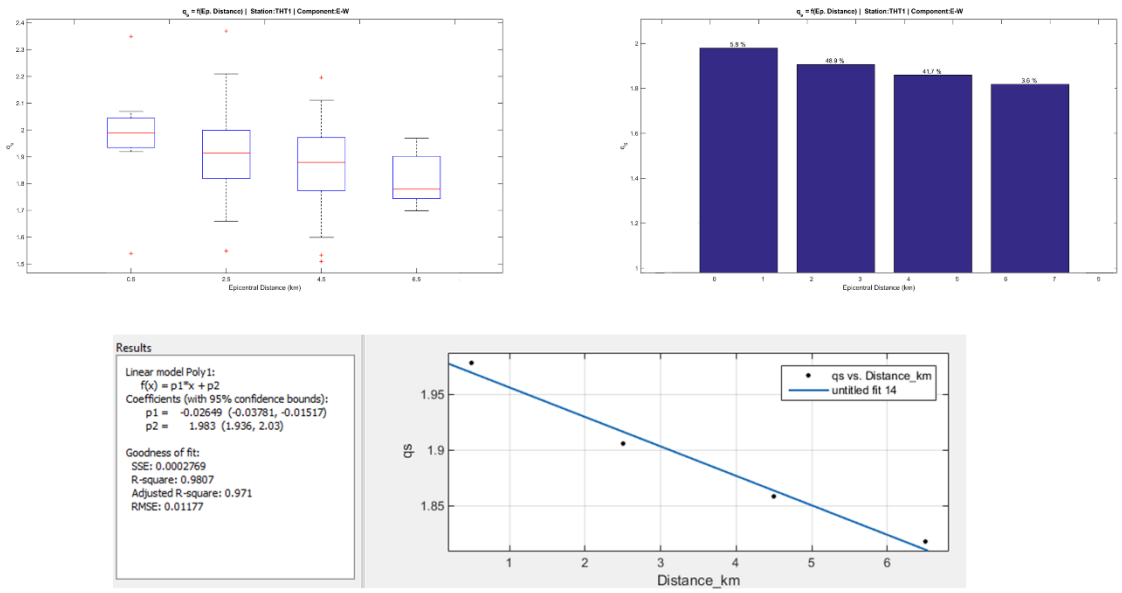

Figure 7.43 Whisker plot statistical analysis of q_s as a function of epicentral distance (measured in km) for station THT1 and E-W component.

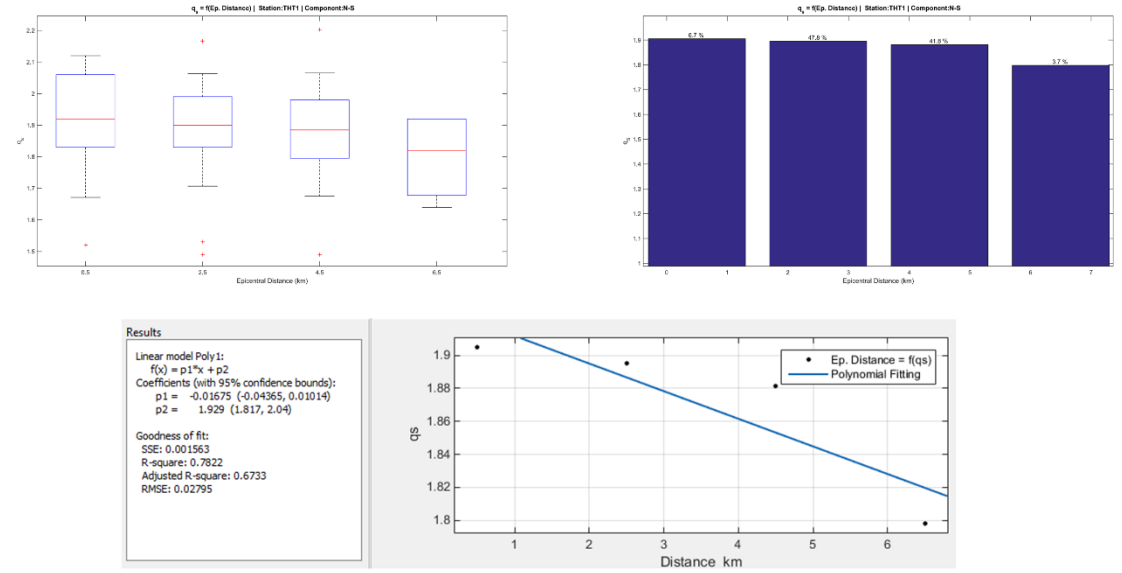

Figure 7.44 Whisker plot statistical analysis of q_s as a function of epicentral distance (measured in km) for station THT1 and N-S component.

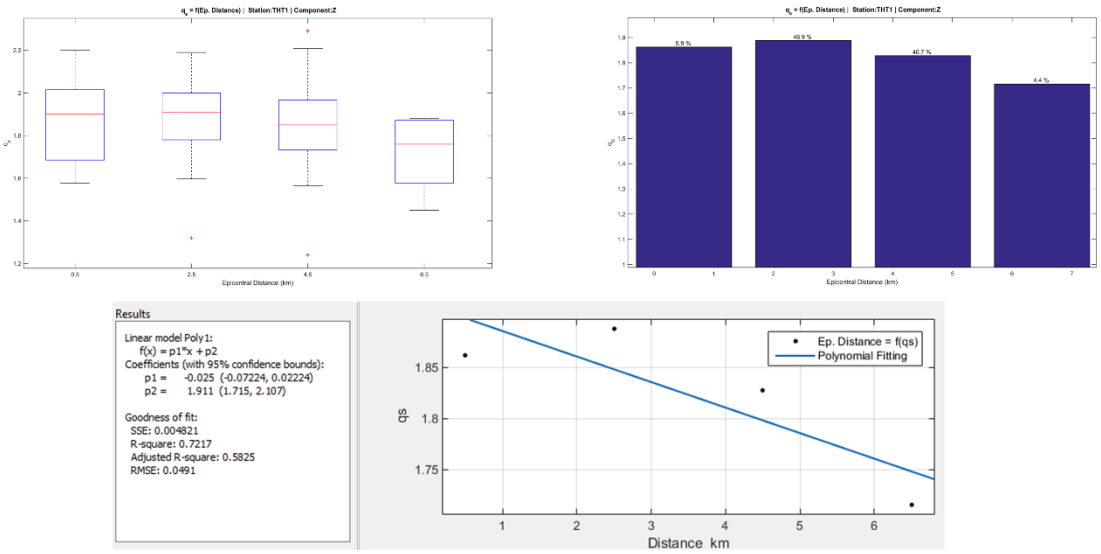

Figure 7.45 Whisker plot statistical analysis of q_s as a function of epicentral distance (measured in km) for station THT1 and Z component.

	Magnitude M_L			Epicentral Distance (km)		
STATION	P1	P2	R^2	P1	P2	R^2
SANT E-W	0.22	1.12	0.86	-0.05	1.99	0.88
SANT N-S	0.16	1.13	0.9	-0.05	1.76	0.85
SANT Z	0.21	1.1	0.83	-0.05	1.88	0.78
CMBO E-W	0.14	1.6	0.71	0.03	1.72	0.64
CMBO N-S	0.13	1.6	0.6	0.03	1.71	0.74
CMBO Z	0.14	1.59	0.64	0.03	1.73	0.71
THT1 E-W	0.1	1.73	0.73	-0.03	1.98	0.98
THT1 N-S	0.1	1.73	0.86	-0.02	1.93	0.78
THT1 Z	0.13	1.61	0.83	-0.03	1.91	0.72

Table 7.1 Summarized results of linear regression models.

7.4 q_s index variation per station pair. Outliers and extreme values.

The dynamic change of the scatterers distribution within the wider area of Santorini's caldera, can be evaluated as the temporal variation of the differences between the q_s indices, for same earthquake events, observed on different seismological stations. These

values are essential, since they depict individual regimes and unique sub-surface processes, with divergent physical properties.

Energy contribution outside the volcanic system or any ambient geo-physical change within Santorini's caldera, that can potentially lead to the change of any physical subsurface property, implies variations of the entropic scattering index. The observed temporal q_s variations, are in agreement with the GPS displacement observation of NOMI station, as presented in Figure 7.49.

The extremes values, generated from the differences of the entropic scattering index between the station pairs of:

- SANT – CMBO
- SANT – THT1
- CMBO – THT1

are presented in the following figures (Figure 7.46 to Figure 7.48). The extreme values are strictly confined within the caldera's area, covering the period from 10/2011 to 03/2012 (mm/yyyy).

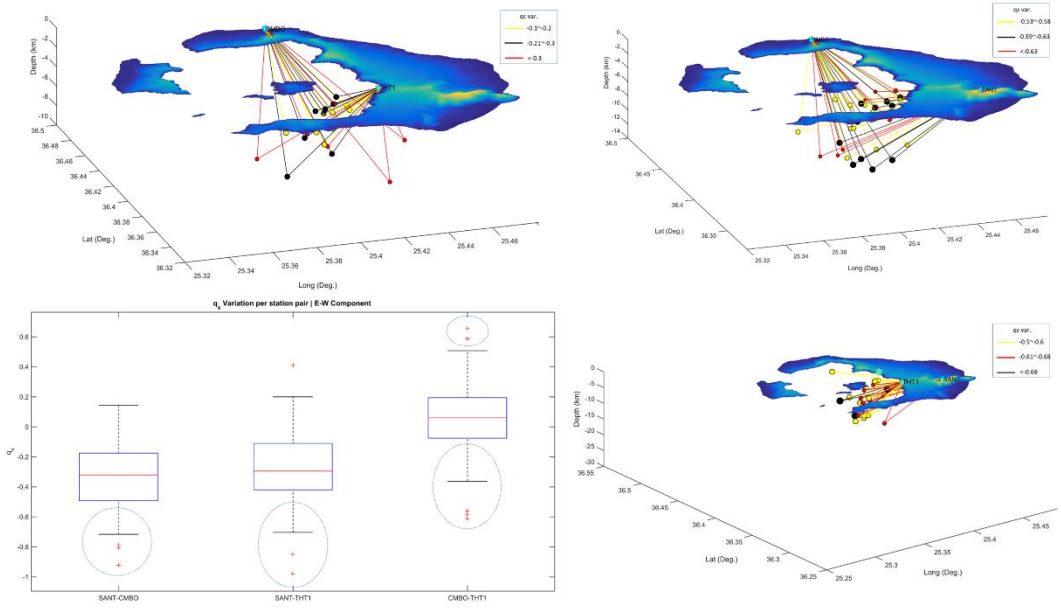

Figure 7.46 Extreme values of the q_s index, obtained from the pair-station difference for individual earthquake events procedure. Component E-W.

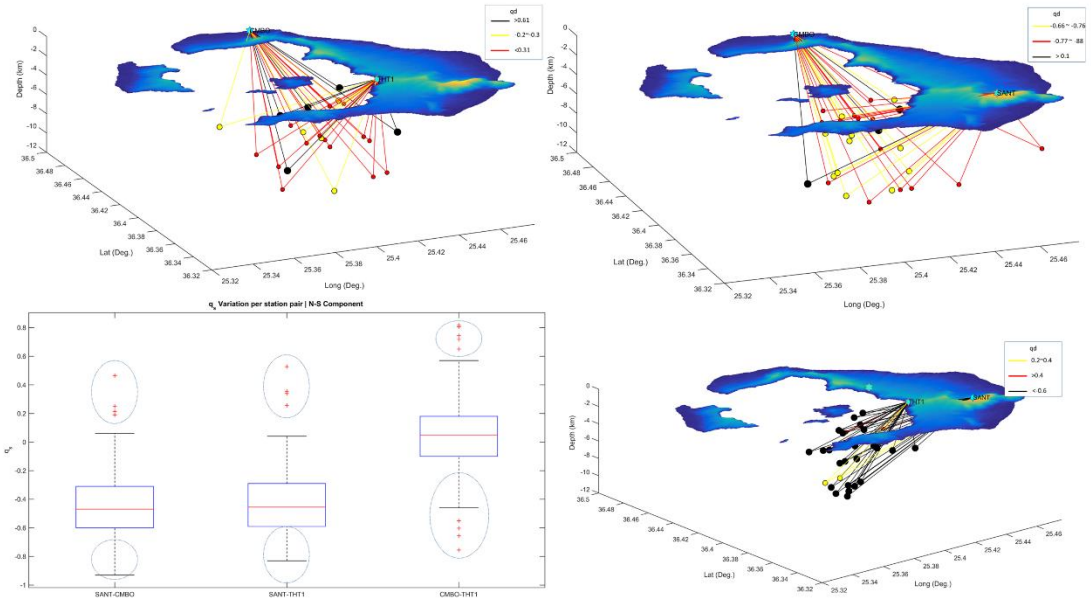

Figure 7.47 Extreme values of the q_S index, obtained from the pair-station difference for individual earthquake events procedure. Component N-S.

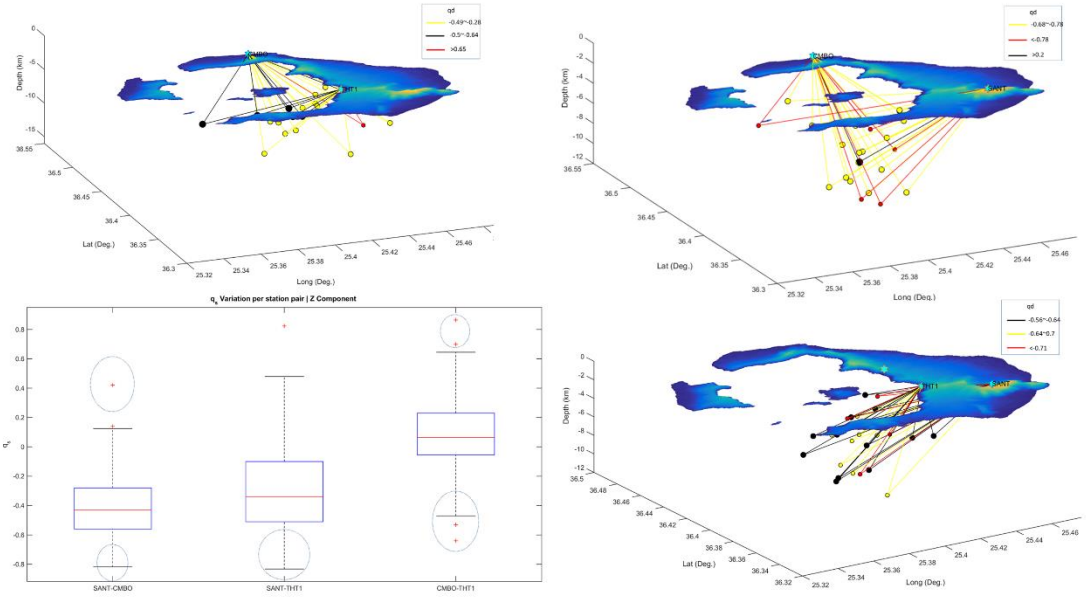

Figure 7.48 Extreme values of the q_S index, obtained from the pair-station difference for individual earthquake events procedure. Component Z.

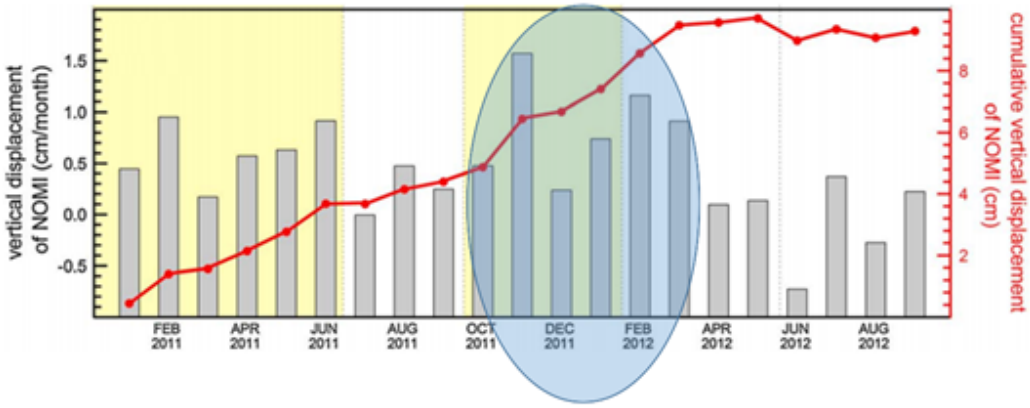

Figure 7.49 Monthly and cumulative rates of the vertical displacement of GPS station NOMI [35].

7.5 Discussion and Conclusions

For all earthquake events, coda wave increments, as presented in 5.2.3 section, deviate from the Gaussian distribution, carrying long-term memory effects. The non-extensive statistical physics approach is now considered as a sufficient and necessary condition, for the study of volcanic systems via instrumental observations.

The temporal variation of q_s index, indicates dependence between the volcanic activity and the observed seismicity, as both phenomena contributed to the increase of the amount of q_s during the unrest period.

As seen from Figure 7.1 to Figure 7.9, the scattering entropic index for all seismological stations and for the three components, showed an increasing trend and high values during the volcanic crisis, following a declining trend towards the background level. The reduction behavior coincides with the decrease of seismicity.

For the seismological station 'SANT', before and after the volcanic unrest period, the maximum q_s values were estimated at 1.75 in comparison with the volcanic crisis period, where the entropic index reached the amount of 2.14. This change indicates an increase of 22.3%. The same behavior was observed at both CMBO and THT1 stations. In the case of CMBO, after the well-defined unrest period, the entropic index has set its upper limit to the value of 2, while during the crisis it reached the value of 2.4, showing an increase of 20%. Last, the raise of the entropic scattering index for THT1 station, reached 21.1% (from 1.9 to 2.3).

The spatiotemporal variation of the q_s index, as observed after the analysis procedure, presents strong correlation with the observed seismicity alongside the Kameni

tectonovolcanic lineament. On the contrary, as seen in Figure 7.22Figure 7.23Figure 7.24, seismic events along the Columbo tectonovolcanic lineament did not indicate any affect signs upon codas increments properties, keeping the q_s index to the background level. This behavior is in agreement with the hypothesis that all major volcanic events-eruptions of Santorini's Volcano are associated with seismicity, accompanied with fluids and magma migrations within the Kameni tectonovolcanic lineament. As might be expected, the threshold, at which the entropic scattering index of the system must be found, in order to indicate an underlying volcanic high intense volcanic activity, is still unknown, since the Santorini's volcanic complex hasn't shown an adequate number of low frequency seismic events, spasmodic bursts and continuous tremors, all indications of a potential volcanic eruption.

As showed in Figure 7.1 to Figure 7.9, the q_s indices present higher values at CMBO and THT1 stations. The lower values of q_s at SANT station, indicates lower scatterers distribution at the southeast part of Santorini. This contrast, corresponds to the dominant geological feature of Santorini's island, expressed by the geophysical difference between the intra-caldera volcanic rocks with the surface expression, dense bedrock of the Profitis Ilias mountain.

These observations strengthen the hypothesis that scatterers are magnifying the entropic parameter q_s at the Caldera's vicinity, as seismic wavefronts encounter more obstacles in their ray-paths, due to a constant dynamical change regime.

After extensive statistical process and analysis of the entropic scattering index, we came to the conclusion that there is a slight relation of the entropic index q_s with the local magnitude (M_L). For all stations and for all three components, as the magnitude increases the q_s increases too.

Furthermore, the correlation of q_s as a function of epicentral distance, measured in kilometers, showed a decreased behavior for SANT and THT1 stations, while for CMBO station, this relation is expressed by a positive slope.

An important finding, regarding the dynamical evolution of the Santorini's Volcano, is the correlation between the vertical ground displacement, as observed by the GPS station of NOMI (see Figure 7.49), and the extreme values and outliers of the entropic scattering index differences, as calculated per pair of stations.

This indication is considered an additional verification of Tsalli's non-extensive statistical physics implementation, upon complex natural-physical systems, being under dynamic evolution.

Fluctuations of the entropic scattering index among the three components (HHE, HHN and HHZ) are constant and, in some cases, this difference exceeds the permissible deviation in order for a solution to be acceptable. This phenomenon is crucial and has to be considered in further research studies.

8 Bibliography

[1] Aspiotis Theodoros et al., "Dynamical evolution of the seismic coda wave increments during the 2011-2012 Santorini's caldera unrest. A Non-Extensive Statistical Physics approach. In: EGU General Assembly Conference Abstracts. 2020. p. 8190.".

[2] B. BIJU-DUVAL111, J. DERCOURT121 and X. LE PICHON, "From the Tethys ocean to the Mediterranean seas: a plate tectonic model of the evolution of the western Alpine system," *Histoire structurale des bassins méditerranéens,* p. 143, 1977.

[3] NOMIKOU, P., et al., "Submarine volcanoes of the Kolumbo volcanic zone NE of Santorini Caldera, Greece," *Global and Planetary Change,* pp. 90: 135-151., 2012.

[4] G. PE-PIPER and D. J. W. PIPER, "The South Aegean active volcanic arc: relationships between magmatism and tectonics.," *Developments in Volcanology ,* pp. p. 113-133, Elsevier, 2005.

[5] PAPAZACHOS, B. C., et al, "Fault plane solutions in the Aegean Sea and the surrounding area and their tectonic implication," *Boll. Geof. teor. appl, 1998, 39.3: 199-218..*

[6] X. LE PICHON and C. KREEMER, "The Miocene-to-present kinematic evolution of the Eastern Mediterranean and Middle East and its implications for dynamics. Annual Review of Earth and Planetary Sciences, 2010, 38: 323-351.".

[7] X. LE PICHON and J. ANGELIER, "The Hellenic arc and trench system: a key to the neotectonic evolution of the eastern Mediterranean area. Tectonophysics, 1979, 60.1-2: 1-42".

[8] HOLLENSTEIN, Ch, et al, "Crustal motion and deformation in Greece from a decade of GPS measurements, 1993–2003. Tectonophysics, 2008, 449.1-4: 17-40.".

[9] X. LE PICHON and J. ANGELIER, "The Hellenic arc and trench system: a key to the neotectonic evolution of the eastern Mediterranean area. Tectonophysics, 1979, 60.1-2: 1-42.".

[10] MCCLUSKY, S1, et al., "Global Positioning System constraints on plate kinematics and dynamics in the eastern Mediterranean and Caucasus. Journal of Geophysical Research: Solid Earth, 2000, 105.B3: 5695-5719.".

[11] L. H. ROYDEN and D. J. PAPANIKOLAOU, "Slab segmentation and late Cenozoic disruption of the Hellenic arc. Geochemistry, Geophysics, Geosystems, 2011, 12.3.".

[12] ARMIJO, Rolando, et al., "Westward propagation of the North Anatolian fault into the northern Aegean: Timing and kinematics. Geology, 1999, 27.3: 267-270.".

[13] L. JOLIVET and J.-P. BRUN, "Cenozoic geodynamic evolution of the Aegean. International

Journal of Earth Sciences, 2010, 99.1: 109-138.".

[14] S. RONDENAY, "Multi-disciplinary experiments for dynamic understanding of subduction under the aegean sea. International Federation of Digital Seismograph Networks, 2006.".

[15] PAPADIMITRIOU, P., et al., "The Santorini Volcanic Complex: a detailed multi-parameter seismological approach with emphasis on the 2011–2012 unrest period. Journal of Geodynamics, 2015, 85: 32-57.".

[16] TZANIS, A., et al., "Tectonic deformation in the Santorini volcanic complex (Greece) as inferred by joint analysis of gravity, magnetotelluric and DGPS observations. Geophysical Journal International, 2020, 220.1: 461-489.".

[17] D. MCKENZIE, "Active tectonics of the Mediterranean region. Geophysical Journal International, 1972, 30.2: 109-185.".

[18] FYTIKAS, M., et al. , "Tertiary to Quaternary evolution of volcanism in the Aegean region. Geological Society, London, Special Publications, 1984, 17.1: 687-699.".

[19] C. MONACO and L. TORTORICI, "Faulting and effects of earthquakes on Minoan archaeological sites in Crete (Greece). Tectonophysics, 2004, 382.1-2: 103-116.".

[20] A. NUR and E. H. CLINE, "Poseidon's horses: plate tectonics and earthquake storms in the Late Bronze Age Aegean and Eastern Mediterranean. Journal of Archaeological Science, 2000, 27.1: 43-63.".

[21] FRIEDRICH, Walter L., et al., "Santorini eruption radiocarbon dated to 1627-1600 BC. Science, 2006, 312.5773: 548-548.".

[22] A. BOND and R. S. J. SPARKS, "The minoan eruption of Santorini, Greece. Journal of the Geological Society, 1976, 132.1: 1-16.".

[23] T. H. DRUITT and V. FRANCAVIGLIA, "Caldera formation on Santorini and the physiography of the islands in the late Bronze Age. Bulletin of Volcanology, 1992, 54.6: 484-493.".

[24] F. W. MCCOY and G. HEIKEN, "Tsunami generated by the Late Bronze age eruption of Thera (Santorini), Greece. Pure and Applied Geophysics, 2000, 157.6-8: 1227-1256.".

[25] Y. Gorokhovich, "SANTORINI, Eruption. Santorini, Eruption. 2012.".

[26] F. FOUQUE, Santorini and Its Eruptions (translated and annotated by AR McBirney, 1998). 1879..

[27] M. FYTIKAS, Post-Minoan volcanic activity of the Santorini volcano. Volcanic hazard and risk. Forecasting possibilities. Thera and the Aegean world III, 1990, 2: 183-198..

[28] V. SALTOGIANNI and S. C. STIROS, Modeling the Mogi magma source centre of the Santorini (Thera) volcano, Aegean Sea, Greece, 1994–1999, based on a numerical-

topological approach. Studia Geophysica et Geodaetica, 2012, 56.4: 1037-1062..

[29] NEWMAN, Andrew V., et al., Recent geodetic unrest at Santorini caldera, Greece. Geophysical Research Letters, 39(6)..

[30] PARKS, Michelle M., et al., Evolution of Santorini Volcano dominated by episodic and rapid fluxes of melt from depth. Nature Geoscience, 2012, 5.10: 749-754..

[31] KAVIRIS, G., et al., "A detailed seismic anisotropy study during the 2011-2012 unrest period in the Santorini Volcanic Complex. Physics of the Earth and Plan".

[32] T. H. DRUITT and V. FRANCAVIGLIA, Caldera formation on Santorini and the physiography of the islands in the late Bronze Age. Bulletin of Volcanology, 1992, 54.6: 484-493..

[33] DRUITT, T. H., et al., Explosive volcanism on Santorini, Greece. Geological Magazine, 1989, 126.2: 95-126..

[34] D. M. PYLE and J. R. ELLIOTT, Quantitative morphology, recent evolution, and future activity of the Kameni Islands volcano, Santorini, Greece. Geosphere, 2006, 2.5: 253-268..

[35] SALTOGIANNI, Vasso, et al. , Time-space modeling of the dynamics of Santorini volcano (Greece) during the 2011–2012 unrest. Journal of Geophysical Research: Solid Earth, 2014, 119.11: 8517-8537..

[36] K. AKI, Analysis of the seismic coda of local earthquakes as scattered waves. Journal of geophysical research, 1969, 74.2: 615-631..

[37] E. CARCOLÉ and H. SATO, Spatial distribution of scattering loss and intrinsic absorption of short-period S waves in the lithosphere of Japan on the basis of the Multiple Lapse Time Window Analysis of Hi-net data. Geophysical Journal International, 2010, 180.1: 268-290..

[38] P. E. MALIN, A first-order scattering solution for modelling elastic wave codas—I. The acoustic case. Geophysical Journal International, 1980, 63.2: 361-380..

[39] K. AKI and B. CHOUET, Origin of coda waves: source, attenuation, and scattering effects. Journal of geophysical research, 1975, 80.23: 3322-3342..

[40] A. R. LEVANDER and N. R. HILL, P-SV resonances in irregular low-velocity surface layers. Bulletin of the Seismological Society of America, 1985, 75.3: 847-864..

[41] EWING, William Maurice, et al., "Elastic waves in layered media. PhT, 1957, 10.12: 27.".

[42] K. TAKANO, "Analysis of seismic coda waves of ultra microearthquakes in the Matsushiro area. Journal of Physics of the Earth, 1971, 19.3: 209-215.".

[43] E. BISZTRICSANY, "A new method for the determination of the magnitude of earthquakes. Geofiz. Kozlemen, 1958, 7.2.".

[44] K. TSUMURA, "Determination of earthquake magnitude from total duration of oscillation. Bull. Earthquake Res. Inst. Univ. Tokyo, 1967, 45: 7-18.".

[45] C. R. REAL and T.-L. TENG, "Local Richter magnitude and total signal duration in southern California. Bulletin of the Seismological Society of America, 1973, 63.5: 1809-1827.".

[46] W. H. BAKUN, "Seismic moments, local magnitudes, and coda-duration magnitudes for earthquakes in central California. Bulletin of the Seismological Society of America, 1984, 74.2: 439-458.".

[47] C. A. MICHAELSON, "Coda duration magnitudes in central California: An empirical approach. Bulletin of the Seismological Society of America, 1990, 80.5: 1190-1204.".

[48] MOUAYN, Issam, et al., "Duration magnitude scale and site residuals for Northern Morocco. pure and applied geophysics, 2004, 161.5-6: 1061-1080.".

[49] S. MATSUMOTO, "Characteristics of coda waves and inhomogeneity of the earth. Journal of Physics of the Earth, 1995, 43.3: 279-299.".

[50] H. SATO, M. C. FEHLER and T. MAEDA, "Seismic wave propagation and scattering in the heterogeneous earth. Springer Science & Business Media, 2012.".

[51] L. S. GAO, "Coda wave analysis for distinguishing attenuation due to isotropic scattering from attenuation due to absorption. pure and applied geophysics, 1984, 122.1: 1-9.".

[52] A. M. DAINTY and M. N. TOKSÖZ, "Seismic codas on the Earth and the Moon: A comparison. Physics of the Earth and Planetary Interiors, 1981, 26.4: 250-260.".

[53] NAKAMURA, Y., et al., "Lunar seismic energy transmission. TrAGU, 1970, 51: 776.".

[54] DAINTY, Anton M., et al., "Seismic scattering and shallow structure of the Moon in Oceanus Procellarum. The Moon, 1974, 9.1-2: 11-29.".

[55] LOGNONNÉ, Philippe, et al., "Constraints on the shallow elastic and anelastic structure of Mars from InSight seismic data. Nature Geoscience, 2020, 13.3: 213-220.".

[56] J. WESLEY, "Diffusion of seismic energy in the near range. Journal of geophysical research, 1965, 70.20: 5099-5106".

[57] DAINTY, A. M., et al., "Elastic wave propagation in a highly scattering medium-a diffusion approach. Journal of Geophysics| IF 32.18, 1977, 43.1: 375-388.".

[58] A. M. DAINTY and M. N. TOKSÖZ, "Seismic codas on the Earth and the Moon: A comparison. Physics of the Earth and Planetary Interiors, 1981, 26.4: 250-260.".

[59] M. A. HEDLIN and P. M. SHEARER, " An analysis of large-scale variations in small-scale mantle heterogeneity using Global Seismographic Network recordings of precursors to

PKP. Journal of Geophysical Research: Solid Earth, 2000, 105.B6: 13655-13673.".

[60] HERRMANN, Robert B., "Q estimates using the coda of local earthquake. Bulletin of the Seismological Society of America, 1980, 70.2: 447-468.".

[61] A. M. SUTEAU and J. H. WHITCOMB, "A local earthquake coda magnitude and its relation to duration, moment Mo, and local Richter magnitude ML. Bulletin of the Seismological Society of America, 1979, 69.2: 353-368.".

[62] Gao, L. S., et al., "Effects of multiple scattering on coda waves in three-dimensional medium. pure and applied geophysics, 1983, 121.1: 3-15.".

[63] KOPNICHEV, Y. F., "Models for the formation of the coda of the longitudinal wave (English Trans.). In: Dokl. Akad. Nauk SSSR. 1977. p. 13-15.".

[64] R.-S. WU, "Multiple scattering and energy transfer of seismic waves—separation of scattering effect from intrinsic attenuation—I. Theoretical modelling. Geophysical Journal International, 1985, 82.1: 57-80.".

[65] S. 1. Chandrasekhar, "Radiative Transfer, Dover, New York (revised version of 1950)".

[66] Y. ZENG, "Theory of scattered P-and S-wave energy in a random isotropic scattering medium. Bulletin of the Seismological Society of America, 1993, 83.4: 1264-1276.".

[67] H. SATO, "Multiple isotropic scattering model including PS conversions for the seismogram envelope formation. Geophysical Journal International, 1994, 117.2: 487-494.".

[68] U. WEGLER, M. KORN and J. PRZYBILLA, "Modeling full seismogram envelopes using radiative transfer theory with Born scattering coefficients. pure and applied geophysics, 2006, 163.2-3: 503-531.".

[69] J. PRZYBILLA, M. KORN and U. WEGLER, "Radiative transfer of elastic waves versus finite difference simulations in two-dimensional random media. Journal of Geophysical Research: Solid Earth, 2006, 111.B4.".

[70] A. A. GUSEV and I. R. ABUBAKIROV, "Monte-Carlo simulation of record envelope of a near earthquake. Physics of the earth and planetary interiors, 1987, 49.1-2: 30-36.".

[71] M. HOSHIBA, " Simulation of multiple-scattered coda wave excitation based on the energy conservation law. Physics of the Earth and Planetary Interiors, 1991, 67.1-2: 123-136.".

[72] L. RYZHIK, G. PAPANICOLAOU and J. B. KELLER, "Transport equations for elastic and other waves in random media. Wave motion, 1996, 24.4: 327-370.".

[73] R. L. WEAVER, "Equipartition and retrieval of Green's function. Earthquake Science, 2010, 23.5: 397-402.".

[74] LINE, C. E. R., et al., "Statistical inversion of controlled-source seismic data using parabolic wave scattering theory. Geophysical journal international, 1998, 132.1: 61-78.".

[75] K. NISHIGAMI, "A new inversion method of coda waveforms to determine spatial distribution of coda scatterers in the crust and uppermost mantle. Geophysical research letters, 1991, 18.12: 2225-2228.".

[76] HARTSE, Hans E., et al. , "Single-station spectral discrimination using coda waves. Bulletin of the Seismological Society of America, 1995, 85.5: 1464-1474.".

[77] M. HOSHIBA, "Estimation of nonisotropic scattering in western Japan using coda wave envelopes: Application of a multiple nonisotropic scattering model. Journal of Geophysical Research: Solid Earth, 1995, 100.B1: 645-657.".

[78] OBERMANN, Anne, et al., "4-D Imaging of Subsurface Changes with Coda Waves: Numerical Studies of 3-D Combined Sensitivity Kernels and Applications 2008 Wenchuan Earthquake. Pure and Applied Geophysics, 2019, 176.3: 1243-1254.".

[79] R.-S. WU and K. AKI, "Introduction: Seismic wave scattering in three-dimensionally heterogeneous earth. In: Scattering and Attenuations of Seismic Waves, Part I. Birkhäuser, Basel, 1988. p. 1-6.".

[80] T. G. RAUTIAN and V. I. KHALTURIN, "The use of the coda for determination of the earthquake source spectrum. Bulletin of the Seismological Society of America, 1978, 68.4: 923-948.".

[81] B. CHOUET, "Source, scattering and attenuation effects on high frequency seismic waves. 1976. PhD Thesis. Massachusetts Institute of Technology.".

[82] A. FRANKEL and L. WENNERBERG, " Energy-flux model of seismic coda: separation of scattering and intrinsic attenuation. Bulletin of the Seismological Society of America, 1987, 77.4: 1223-1251.".

[83] MOROZOV, Igor B., et al., "Frequency dependence of coda Q, part I: numerical modeling and examples from peaceful nuclear explosions. Bulletin of the Seismological Society of America, 2008, 98.6: 2615-2628.".

[84] J. BOATWRIGHT, "A spectral theory for circular seismic sources; simple estimates of source dimension, dynamic stress drop, and radiated seismic energy. Bulletin of the Seismological Society of America, 1980, 70.1: 1-27.".

[85] RAUTIAN, T. G., et al. , "Preliminary analysis of the spectral content of P and S waves from local earthquakes in the Garm, Tadjikistan region. Bulletin of the Seismological Society of America, 1978, 68.4: 949-971.".

[86] J. BRAHMA, "Estimation of coda wave attenuation quality factor from digital seismogram using statistical approach. Science and Technology, 2012, 2.1: 1-7.".

[87] OBERMANN, Anne, et al. , "Depth sensitivity of seismic coda waves to velocity perturbations in an elastic heterogeneous medium. Geophysical Journal International, 2013, 194.1: 372-382.".

[88] I. B. MOROZOV, "Temporal variations of coda Q: An attenuation-coefficient view. Physics of the Earth and Planetary Interiors, 2011, 187.1-2: 47-55.".

[89] T. RIKITAKE, "Earthquake precursors. Bulletin of the Seismological Society of America, 1975, 65.5: 1133-1162.".

[90] S. CRAMPIN, "Geological and industrial implications of extensive-dilatancy anisotropy. Nature, 1987, 328.6130: 491-496.".

[91] S. PULINETS and D. OUZOUNOV, "Lithosphere–Atmosphere–Ionosphere Coupling (LAIC) model–An unified concept for earthquake precursors validation. Journal of Asian Earth Sciences, 2011, 41.4-5: 371-382.".

[92] BULLEN, Keith Edward, et al. , "An introduction to the theory of seismology. Cambridge university press, 1985.".

[93] A. JIN and K. AKI, "JIN, Anshu; AKI, Keiiti.".

[94] MAK, Sum, et al., "Coda Q estimates in the Hong Kong region. Journal of Asian Earth Sciences, 2004, 24.1: 127-136.".

[95] DOBRYNINA, Anna A., et al. , "Spatial changes of seismic attenuation and multiscale geological heterogeneity in the Baikal Rift and surroundings from analysis of coda waves. Tectonophysics, 2016, 675: 50-68.".

[96] C. TSALLIS, "Possible generalization of Boltzmann-Gibbs statistics. Journal of statistical physics, 1988, 52.1-2: 479-487.".

[97] I. KOUTALONIS and F. VALLIANATOS, "Evidence of non-extensivity in Earth's ambient noise. Pure and Applied Geophysics, 2017, 174.12: 4369-4378.".

[98] K. IOANNIS and V. FILIPPOS, "Observational evidence of non-extensive behaviour of seismic coda waves. Physica A: Statistical Mechanics and its Applications, 2020, 124523.".

[99] A. JIN and K. AKI, "Temporal change in coda Q before the Tangshan earthquake of 1976 and the Haicheng earthquake of 1975. Journal of Geophysical Research: Solid Earth, 1986, 91.B1: 665-673.".

[100] W. H. BAKUN and A. G. LINDH, "Local magnitudes, seismic moments, and coda durations for earthquakes near Oroville, California. Bulletin of the Seismological Society of America, 1977, 67.3: 615-629.".

[101] LEE, William Hung Kan; BENNETT, R. E.; MEAGHER, K., "A method of estimating magnitude of local earthquakes from signal duration. US Department of the Interior, Geological

Survey, 1972.".

[102] LANE, David, et al., "Introduction to statistics. David Lane, 2003.".

[103] I. T. LABORATORY, "Exploratory Data Analysis".

[104] Vsauce, "https://www.youtube.com/watch?v=fCn8zs912OE&ab_channel=Vsauce," [Online].

[105] K. GIESEN and J. SÜDEKUM, Zipf's law for cities in the regions and the country. Journal of Economic Geography, 2011, 11.4: 667-686..

[106] M. E. NEWMAN, Power laws, Pareto distributions and Zipf's law. Contemporary physics, 2005, 46.5: 323-351..

[107] X. GABAIX, "Zipf's law for cities: an explanation. The Quarterly journal of economics, 1999, 114.3: 739-767.".

[108] J. D. BURGOS and P. MORENO-TOVAR, "Zipf-scaling behavior in the immune system. Biosystems, 1996, 39.3: 227-232.".

[109] M. A. MONTEMURRO, "Beyond the Zipf–Mandelbrot law in quantitative linguistics. Physica A: Statistical Mechanics and its Applications, 2001, 300.3-4: 567-578.".

[110] C. TULLO and J. HURFORD, "Modelling Zipfian distributions in language. In: Proceedings of language evolution and computation workshop/course at ESSLLI. 2003. p. 62-75.".

[111] R. FERRER-I-CANCHO and B. ELVEVÅG, "Random texts do not exhibit the real Zipf's law-like rank distribution. PLoS One, 2010, 5.3: e9411.".

[112] R. D. SMITH, "Investigation of the Zipf-plot of the extinct Meroitic language. arXiv preprint arXiv:0808.2904, 2008.".

[113] HUMPHRIES, Nicolas E., et al. , "Environmental context explains Lévy and Brownian movement patterns of marine predators. Nature, 2010, 465.7301: 1066-1069.".

[114] E. BORNBERG-BAUER, "How are model protein structures distributed in sequence space?. Biophysical Journal, 1997, 73.5: 2393-2403.".

[115] L. A. ADAMIC, "Zipf, power-laws, and pareto-a ranking tutorial. Xerox Palo Alto Research Center, Palo Alto, CA, http://ginger. hpl. hp. com/shl/papers/ranking/ranking. html, 2000.".

[116] D. J. SCHWAB, I. NEMENMAN and P. MEHTA, "Zipf’s law and criticality in multivariate data without fine-tuning. Physical review letters, 2014, 113.6: 068102.".

[117] G. NEUKUM and B. A. IVANOV, "Crater size distributions and impact probabilities on Earth from lunar, terrestrial-planet, and asteroid cratering data. Hazards due to Comets and

Asteroids, 1994, 1: 359-416.".

[118] B. BLASIUS and R. TÖNJES, "Zipf's law in the popularity distribution of chess openings. Physical review letters, 2009, 103.21: 218701.".

[119] J. T. WIXTED, "The psychology and neuroscience of forgetting. Annu. Rev. Psychol., 2004, 55: 235-269.".

[120] PIETRONERO, Luciano, et al. , "Explaining the uneven distribution of numbers in nature: the laws of Benford and Zipf. Physica A: Statistical Mechanics and its Applications, 2001, 293.1-2: 297-304.".

[121] F. VALLIANATOS, G. PAPADAKIS and G. MICHAS, "Generalized statistical mechanics approaches to earthquakes and tectonics. Proceedings of the Royal Society A: Mathematical, Physical and Engineering Sciences, 2016, 472.2196: 20160497.".

[122] M. L. GOLDSTEIN, S. A. MORRIS and G. G. YEN, "Problems with fitting to the power-law distribution. The European Physical Journal B-Condensed Matter and Complex Systems, 2004, 41.2: 255-258.".

[123] N. L. JOHNSON, A. W. KEMP and S. KOTZ, "Univariate discrete distributions. John Wiley & Sons, 2005.".

[124] B. GUTENBERG, "he energy of earthquakes. Quarterly Journal of the Geological Society, 1956, 112.1-4: 1-14.".

[125] K. AKI, "Maximum likelihood estimate of b in the formula log N= a-bM and its confidence limits. Bull. Earthq. Res. Inst., Tokyo Univ., 1965, 43: 237-239.".

[126] O. SOTOLONGO-COSTA and POSADAS, "A. Fragment-asperity interaction model for earthquakes. Physical review letters, 2004, 92.4: 048501.".

[127] H. KANAMORI and D. L. ANDERSON, "Theoretical basis of some empirical relations in seismology. Bulletin of the seismological society of America, 1975, 65.5: 1073-1095.".

[128] H. KANAMORI, "Quantification of earthquakes. Nature, 1978, 271.5644: 411-414.".

[129] K. AKI, " A probabilistic synthesis of precursory phenomena. Earthquake prediction: an international review, 1981, 4: 566-574.".

[130] SPYROPOULOS, Chrysanthe, et al., "Experimental evidence for different strain regimes of crack populations in a clay model. Geophysical Research Letters, 1999, 26.8: 1081-1084.".

[131] T. T. CLADOUHOS and R. MARRETT, "Are fault growth and linkage models consistent with power-law distributions of fault lengths?. Journal of Structural Geology, 1996, 18.2-3: 281-293.".

[132] A. GUPTA and C. H. SCHOLZ, "Brittle strain regime transition in the Afar depression: Implications for fault growth and seafloor spreading. Geology, 2000, 28.12: 1087-1090.".

[133] T. YAMASHITA, "Attenuation and dispersion ofSH waves due to scattering by randomly distributed cracks. pure and applied geophysics, 1990, 132.3: 545-568.".

[134] MAIN, Ian G., et al., "Influence of fractal flaw distributions on rock deformation in the brittle field. Geological Society, London, Special Publications, 1990, 54.1: 81-96.".

[135] D. BEARINGER and C. HILLIER, "Fracture Characterization: From Core to Discrete Fracture Network Model. Geophysics, 2016, 39.3: 347-383.".

[136] H. SATO and R. FUKUSHIMA, "Radiative transfer theory for the fractal structure and power-law decay characteristics of short-period seismograms. Geophysical Journal International, 2013, 195.3: 1831-1842.".

[137] DURRANT, Alan (ed.), Quantum physics of matter. CRC Press, 2000.

[138] D. M. Dowd, "https://www.youtube.com/watch?v=kfffy12uQ7g&ab_channel=PBSSpaceTime," PBS Space Time. [Online].

[139] J. CERNOHORSKY and S. A. BLUDMAN, Maximum entropy distribution and closure for Bose-Einstein and Fermi-Dirac radiation transport. 1994..

[140] D. L. TURCOTTE, Fractals and chaos in geology and geophysics. Cambridge university press, 1997.

[141] D. BHATTACHARYYA and J. M. DAWLATY, Teaching Entropy from Phase Space Perspective: Connecting the Statistical and Thermodynamic Views Using a Simple One-Dimensional Model. Journal of Chemical Education, 2019, 96.10: 2208-2216..

[142] C. TSALLIS, M. GELL-MANN and Y. SATO, Asymptotically scale-invariant occupancy of phase space makes the entropy Sq extensive. Proceedings of the National Academy of Sciences, 2005, 102.43: 15377-15382..

[143] H. GOLDSTEIN, C. POOLE and J. SAFKO, "Classical mechanics. 2002.".

[144] E. C. BREWER, A guide to the scientific knowledge of things familiar. CS Francis & Co., 1852..

[145] Ν. Δ. ΜΑΝΙΏΤΗΣ, "Νανοθερμοδυναμική του Hill και μη εκτατική Στατιστική Μηχανική του Tsallis: Θεωρία και Πείραμα. Aristotle University of Thessaloniki, 2014.".

[146] K. IOANNIS, "A NON-EXTENSIVE STATISTICS APPROACH OF SEISMIC CODA WAVES.".

[147] Ε. ΜΗΤΣΟΚΆΠΑΣ, "Στατιστική μηχανική και εντροπία πολύπλοκων συστημάτων. 2016.

PhD Thesis.".

[148] B. B. MANDELBROT, "The Fractal Geometry of. Nature, 1982, 394-397.".

[149] S. ABE and N. SUZUKI, "Law for the distance between successive earthquakes. Journal of Geophysical Research: Solid Earth, 2003, 108.B2.".

[150] C. H. SCHOLZ, "The Mechanics of Earthquakes and Faulting. Cambridge University Press, Cambridge, 471 p. 2002.".

[151] B. GUTENBERG and C. F. RICHTER, " Frequency of earthquakes in California. Bulletin of the Seismological Society of America, 1944, 34.4: 185-188.".

[152] RUNDLE, John B., et al. , "Statistical physics approach to understanding the multiscale dynamics of earthquake fault systems. Reviews of Geophysics, 2003, 41.4.".

[153] F. VALLIANATOS, I. KOUTALONIS and G. CHATZOPOULOS, "Evidence of Tsallis entropy signature on medicane induced ambient seismic signals. Physica A: Statistical Mechanics and its Applications, 2019, 520: 35-43.".

[154] I. MAIN, " Statistical physics, seismogenesis, and seismic hazard. Reviews of Geophysics, 1996, 34.4: 433-462.".

[155] T. CHELIDZE, F. VALLIANATOS and L. (. TELESCA, "Complexity of Seismic Time Series: Measurement and Application. Elsevier, 2018.".

[156] U. TIRNAKLI and E. P. BORGES, "The standard map: From Boltzmann-Gibbs statistics to Tsallis statistics. Scientific reports, 2016, 6: 23644.".

[157] J. NAIR, A. WIERMAN and B. ZWART, "The fundamentals of heavy-tails: properties, emergence, and identification. In: Proceedings of the ACM SIGMETRICS/international conference on Measurement and modeling of computer systems. 2013. p. 387-388.".

[158] E. T. JAYNES, "Information theory and statistical mechanics. Physical review, 1957, 106.4: 620.".

[159] C. TSALLIS, " Introduction to nonextensive statistical mechanics: approaching a complex world. Springer Science & Business Media, 2009.".

[160] J. BERCHER, "On escort distributions, q-gaussians and Fisher information. In: AIP Conference Proceedings. American Institute of Physics, 2011. p. 208-215.".

[161] G. KANIADAKIS, "Theoretical foundations and mathematical formalism of the power-law tailed statistical distributions. Entropy, 2013, 15.10: 3983-4010.".

[162] S. ABE, "Geometry of escort distributions. Physical Review E, 2003, 68.3: 031101.".

[163] Wolfram, "mathworld.wolfram.com/HilbertTransform," [Online].

[164] M. 2. ABDEL-AKHER, "Index IEEE Transactions on Power Delivery Vol. 25. IEEE Transactions on Power Delivery, 2010, 25.4: 3157.".

[165] UPADHYAYA, Arpita, et al., "Anomalous diffusion and non-Gaussian velocity distribution of Hydra cells in cellular aggregates. Physica A: Statistical Mechanics and its Applications, 2001, 293.3-4: 549-558.".

[166] A. NAKAMICHI and M. MORIKAWA, "Is galaxy distribution non-extensive and non-Gaussian?. Physica A: Statistical Mechanics and its Applications, 2004, 341: 215-233.".

[167] PICOLI JR, S., et al., "q-distributions in complex systems: A brief review. Brazilian Journal of Physics, 2009, 39.2A: 468-474.".

[168] N. GEIN, "https://bbnet.gein.noa.gr/HL/databases/database," [Online].

[169] BEYREUTHER, Moritz, et al., "ObsPy: A Python toolbox for seismology. Seismological Research Letters, 2010, 81.3: 530-533.".

[170] G. KING, D. STURDY and J. WHITNEY, "The landscape geometry and active tectonics of northwest Greece.," *Geological Society of America Bulletin,* vol. 105.2, pp. 137-161, 1993.

[171] P. SAMMONDS and M. OHNAKA, " Evolution of microseismicity during frictional sliding. Geophysical Research Letters, 1998, 25.5: 699-702.".

[172] I. G. MAIN and P. W. BURTON, "Information theory and the earthquake frequency-magnitude distribution. Bulletin of the Seismological Society of America, 1984, 74.4: 1409-1426.".